ORNL
MASTER COPY

10-9

OAK RIDGE NATIONAL LABORATORY
operated by
UNION CARBIDE CORPORATION
for the
U. S. ATOMIC ENERGY COMMISSION

ORNL-TM-1148

STUDIES IN HEAT TRANSFER AND FLUID MECHANICS

PROGRESS REPORT FOR PERIOD OCT. 1, 1963 - JUNE 30, 1964

H. W. Hoffman
J. J. Keyes, Jr.

NOTICE This document contains information of a preliminary nature and was prepared primarily for internal use at the Oak Ridge National Laboratory. It is subject to revision or correction and therefore does not represent a final report.

LEGAL NOTICE

This report was prepared as an account of Government sponsored work. Neither the United States, nor the Commission, nor any person acting on behalf of the Commission:

A. Makes any warranty or representation, expressed or implied, with respect to the accuracy, completeness, or usefulness of the information contained in this report, or that the use of any information, apparatus, method, or process disclosed in this report may not infringe privately owned rights; or

B. Assumes any liabilities with respect to the use of, or for damages resulting from the use of any information, apparatus, method, or process disclosed in this report.

As used in the above, "person acting on behalf of the Commission" includes any employee or contractor of the Commission, or employee of such contractor, to the extent that such employee or contractor of the Commission, or employee of such contractor prepares, disseminates, or provides access to, any information pursuant to his employment or contract with the Commission, or his employment with such contractor.

ORNL-TM-1148

Contract No. W-7405-eng-26

STUDIES IN HEAT TRANSFER AND FLUID MECHANICS
PROGRESS REPORT FOR PERIOD OCT. 1, 1963 – JUNE 30, 1964

H. W. Hoffman
J. J. Keyes, Jr.

AUGUST 1965

OAK RIDGE NATIONAL LABORATORY
Oak Ridge, Tennessee
operated by
UNION CARBIDE CORPORATION
for the
U. S. ATOMIC ENERGY COMMISSION

CONTENTS

Page

SUMMARY v

1. INTRODUCTION 1

2. BOILING HEAT TRANSFER AND TWO-PHASE FLOW 2

2.1. Boiling-Potassium Heat Transfer 2

2.1.1. Forced-Convection System 2

2.1.2. Superheat Phenomena 15

2.2. Boiling in Multirod Geometries 29

2.3. General Boiling Studies 31

2.3.1. Critical Heat Flux for Natural Convection of Water in Blocked Vertical Channels 31

2.4. Swirl-Flow Heat Transfer 34

2.4.1. Swirl-Flow Forced-Convection Bulk-Boiling Burnout. 34

2.4.2. Subcooled Swirl-Flow Boiling and Burnout with Heated Twisted Tapes and Zero Wall Flux 41

2.5. Analysis of Parallel Flow in Rod Clusters 50

3. FLOW DYNAMICS AND TURBULENCE 64

3.1. Vortex Fluid Mechanics — Hydromagnetic Stabilization . . . 64

3.1.1. Theoretical Studies 64

3.1.2. Experimental Studies 83

3.2. Potential Vortex Flow Near a Stationary Disk 99

3.3. Boundary-Layer Transient Phenomena 102

3.4. Turbulent Transport Studies 109

4. THERMOPHYSICAL PROPERTIES 114

4.1. Alkali Liquid Metals 114

4.1.1. Surface Tension of Potassium 114

4.1.2. Density of Potassium 117

4.1.3. Contact-Angle Determinations 117

4.1.4. Surface Tension of Lithium 119

4.1.5. Density of Lithium 122

5. BIBLIOGRAPHY 124

SUMMARY

Boiling Heat Transfer and Two-Phase Flow

Boiling Potassium Heat Transfer. The study of boiling with potassium in forced flow upward through a circular channel was continued following installation of a new boiler. This new section has six heated regions (~1 ft long each with 0.839-in. outside diameter and 0.270-in. inside diameter) separated by adiabatic zones 1.5 in. long in which the wall thickness was reduced to 0.075 in.; the flux capability of this unit was of the order of 100,000 Btu/hr·ft^2. Attempts at fabricating a second high flux unit (~500,000 Btu/hr·ft^2) were unsuccessful, and this effort has been temporarily discontinued.

Additional data were obtained for the critical flux and for two-phase pressure drop with boiling. Two sets of runs terminated with "burnout" and gave values for the critical flux of ~56,000 Btu/hr·ft^2 at a mass flow of 0.7×10^5 lb/hr·ft^2 and ~82,000 Btu/hr·ft^2 at $G = 1.0 \times 10^5$ lb/hr·ft^2; the exit qualities were 100% and 98%, respectively. These results continue to agree well with predictions based on the Lowdermilk, Lanzo, and Siegel water data.

The axial fluid temperature profile (based on pressure measurements made at five stations along the tube assuming liquid-vapor thermal equilibrium) showed a curvature consistent with the wall-temperature profile but fell significantly above the wall temperature values. While this discrepancy may reflect a real phenomenon, it is possible that the source may, in part, derive from a systemic error in pressure measurement or from an uncertainty in the knowledge of vapor pressure for potassium.

Results for fluxes below the critical continue to suggest a lesser dependence on ΔT than observed with water or with the earlier potassium data. However, since these values are associated with small temperature differences (3 to 10°F) and some uncertainty exists in the procedure whereby these differences were obtained, this conclusion remains somewhat doubtful.

Pressure-drop data for two-phase flow of potassium with boiling were observed to correlate well with the specific data of Shrock and Grossman

for water using the Lockhart-Martinelli method of presentation. The simpler homogeneous model was found to predict pressure losses which were only one-third of those measured.

A small natural-circulation loop was constructed to provide a facility for quantitative measurement of the superheat required for bubble nucleation with the alkali liquid metals. Three different surfaces (smooth as-received, porous coating, and discrete holes) were included in the apparatus to provide for testing the influence of surface condition on the superheat. Data on the magnitude of the surface-temperature oscillations were obtained at heat fluxes between 16,000 and 37,000 Btu/hr·ft^2 with the following results:

1. Smooth Surface – Typical wall-temperature oscillations with an average amplitude of 140°F at a frequency of 0.25 cps were recorded at saturation temperatures between 1450 and 1470°F; the corresponding superheats were of the order of 210 to 240°F.

2. Porous Surface – Wall-temperature fluctuations were erratic displaying occasional large temperature spikes (95 to 125°F) randomly dispersed between periods of "quiet" operation with thermal oscillations of low magnitude (2 to 3°F) and high frequency (~1.3 cps) and other periods with fluctuations of intermediate magnitude (~20°F) and frequency (0.13 cps) for saturation temperatures between 1420 and 1450°F. Superheats varied from values of 140 to 180°F associated with the thermal spikes down to 60°F with the intermediate fluctuations and 24 to 30°F with the low magnitude oscillations.

3. Discrete Holes – At a saturation temperature of 820°F, wall-temperature oscillations of ~65°F total amplitude (superheats of 140°F) and a primary frequency of 0.02 cps were observed; superimposed on the fundamental mode was a higher frequency fluctuation of 0.60 to 0.75 cps. As the saturation temperature was increased, the fundamental oscillation decreased in amplitude and increased in frequency, while the secondary fluctuation remained essentially unchanged in both frequency and amplitude. At temperatures above 1200 to 1250°F, only the high-frequency oscillation was detected. Above 1350°F, these oscillations also disappeared; and straight-line traces in both boiler and condenser were recorded. The superheats for the latter situation were of the order of 7 to 12°F.

Measured superheats for the smooth surface ranged from ~700°F at T_{sat} = 950°F to a low of ~270°F at 1480°F. Corresponding results with the porous surface were more complex. For the bulk of the data over the same temperature span as for the smooth surface, the superheat decreased from somewhat more than 100°F to about 12°F. In the limited temperature span between 1300 and 1450°F, the superheat showed significant "scatter" which could be related to the various fluctuation modes described above. Very low superheats (from 80°F at 930°F to 9°F at 1540°F) were observed during periods in which the wall temperature did not oscillate; it was speculated that this condition corresponded to an annular flow with vaporization rather than boiling. For the surface with discrete holes, the superheats ranged from 83°F at 900°F to a low of 7 to 12°F at 1350°F.

Boiling in Multirod Geometries. Preliminary data have been obtained on the critical flux as a function of the exit quality for boiling water in parallel flow through a seven-rod cluster in which the rods were at a 1/16-in. separation. For a saturated inlet condition and mass flows of 2.7 to 3.2×10^4 lb/hr·ft^2, the critical flux varied from ~1.28×10^5 Btu/hr·ft^2 at an exit quality of 35.5% to about 1.13×10^5 Btu/hr·ft^2 at X_e = 41.0%. With all of the rods at the same heat flux, the critical flux was achieved first on the central rod.

General Boiling Studies. The magnitude of the critical heat flux has been analytically estimated and experimentally measured for the condition of flow blockage at the inlet of a natural-circulation cooled channel immersed in a liquid pool. Two correlations of the minimum critical flux were developed. The first was based on an empirical fit of limited available data; and the second, on an adaptation to include the effect of heat addition of Wallis' correlation for adiabatic flooding rates in unheated vertical tubes. Experimental data obtained with tubes of ~0.10- to 0.25-in. inside diameter and 6- to 48-in. heated length fell a factor 2.2 above the minimum flux predicted by the latter correlation. For tubes of less than 0.10-in. inside diameter, the critical flux was below this correlation apparently due to the influence of surface tension.

Swirl-Flow Heat Transfer. An apparatus has been constructed for the study of boiling with net vapor generation within a tube containing a full-length twisted tape. The test channel will be mounted vertically; and data will be obtained over a range of inlet flow rates, inlet subcoolings, and tape-twist ratios. Axial-flow data will be obtained in the same apparatus for comparison with the swirl-flow results. Burnout protection will be provided by a set of subminiature solid-state light-sensitive switches which become conducting when the effective local irradiance becomes sufficiently high and activate a relay and circuit breaker. Preliminary tests with these switches indicated a sharp increase in sensitivity at source temperature of 1100 to 1200°F and no measurable effect of ambient temperature over the range of anticipated operating conditions.

Subcooled swirl-flow boiling was studied for the situation of heat generation within the tape and an adiabatic tube wall over a range of tape-twist ratios, inlet water temperatures, and heat fluxes. It was observed that the critical heat flux for a twisted tape was not markedly greater than for a straight tape; a maximum enhancement of ~20% at a tape-twist ratio of 7 to 10 was noted at the lowest inlet temperature.

Analysis of Flow Through Rod Clusters. The general problem of describing the velocity distribution and the pressure-drop two-phase annular flow in the complex rod-cluster geometry has been considered. As a preliminary, the "simpler" case of single-phase annular flow was developed using separation of variables to reduce the original partial differential equation to a pair of ordinary differential equations. An extended point-match technique was then employed to meet the boundary conditions along the surface of the peripheral rod in the unit flow channel. Other possible mathematical techniques were also evaluated; the difficulties associated with these alternate methods are discussed.

Flow Dynamics and Turbulence

Vortex Fluid Mechanics. The analysis of the effect of a uniform axial magnetic field on stability of vortex motion was continued. An exact criterion, valid for magnetic stabilization both of nondissipative pure vortex flow and of inviscid pure vortex flow with finite conductivity, was

derived. For these cases, it was found that the magnetic field for marginal stabilization increases linearly with the outer peripheral velocity of the vortex and parabolically with the density of the fluid but decreases with an increase in radius ratio (inner/outer) of the two concentric cylinders confining the flow. Equations have also been formulated which, together with the associated boundary conditions, have enabled examination of the more general case of hydromagnetic stability of vortex-like flow (including pure vortex flow) with or without radial flow. The following special cases have been considered in detail.

1. Nondissipative Vortex-Like Flow — The exact criterion for hydromagnetic stabilization is found to depend on the shape of the velocity profile and results are presented in terms of the Alfvén modulus, the radius ratio, and a shape factor for the profile.

2. Dissipative Pure-Vortex Flow — The critical Reynolds modulus has been determined as a function of Hartmann modulus (the dimensionless magnetic field strength) and radius ratio. Small values of magnetic field are found to result in destabilization, whereas large values are stabilizing.

3. Dissipative Vortex-Like Flow — Results are presented for the case of zero radial flow as graphs of the critical Taylor modulus versus the square of the Hartmann modulus for several values of the radius ratio and for the special case in which only the inner cylinder rotates. For this case, the magnetic field is always stabilizing and the critical Taylor modulus becomes proportional to the square of the Hartmann modulus at large values of the latter. In addition, results are presented for the case of outward radial flow as graphs of the critical tangential Reynolds modulus versus radial Reynolds modulus for several values of Hartmann modulus. It is concluded that the effect of increasing radial flow is usually stabilizing and that, while both radial flow and magnetic field are stabilizing, large values of radial flow decrease the effect of the field and vice versa. Furthermore, at large values of radial Reynolds modulus, the critical tangential Reynolds modulus becomes asymptotically proportional to radial Reynolds modulus to the three-halves power, independent of the radius ratio.

The experimental investigation was extended to include a study of the effect of injection geometry (slits versus round nozzles) on stability of

jet-driven vortex-like flow of an aqueous electrolytic conductor under the influence of a uniform axial magnetic field. Two 1.1-in.-diam by 6 1/2-in. long vortex tubes were employed for these studies, and observation of dye filaments injected into the boundary layer along the cylindrical wall was the technique employed for determining effects of the magnetic field on flow stability. It was observed that, for all geometries, the effect of the field is the suppression of flow instabilities of an apparent oscillatory nature which originate along the concave wall at low values of tangential Reynolds modulus when there is no field. Results of flow visualization studies based on analysis of still and motion pictures are described.

Quantitatively, the critical (or transition) value of tangential Reynolds modulus was found to increase approximately linearly with the square of the Hartmann modulus (for sufficiently large values of the latter) in the case of flows generated by two or four slits and also in the case of round nozzles. The data for eight slits suggest a more rapid increase in Reynolds modulus at high values of the Hartmann modulus. The effect of injection geometry is further evidenced by the observation that the critical Reynolds modulus increases with increasing numbers of injection slits, suggesting the effect of growth of the boundary layer between slits. It was also observed that the influence of the field on the recovery of jet velocity as tangential velocity near the periphery is dependent on the ratio of tangential to radial velocity, high values of the latter resulting in relatively large increases in recovery when the flow is magnetically stabilized.

The experimental results are discussed from the point of view of the theory for dissipative, vortex-like flow, with and without radial flow, and some preliminary comparisons are made.

Potential Vortex Flow Near a Stationary Disk. An analytical and experimental investigation has been initiated into the interaction of a vortex flow and a stationary disk, as related to the end-wall by-pass flow problem in vortex tubes. A two-dimensional, free-stream flow closely approximating a pure vortex will be generated experimentally by passing water radially inward through a rotating porous outer drum, with exhaust through a much smaller porous inner tube concentric with the drum. The

boundary layer on a stationary end wall confining the flow will be studied over a wide range of free-stream tangential Reynolds modulus by means of a number of flow visualization techniques presently being developed. A theoretical study of the boundary-layer flow is being made in which the usual boundary-layer simplifications to the momentum equations will not be made, and an analog computer may be used to obtain the tangential and radial velocities simultaneously.

Boundary-Layer Transient Phenomena. Fabrication of the heated, stainless steel test section incorporating gunbarrel-type thermocouples for instantaneous surface temperature measurement was completed to the point of vacuum deposition of the thin film to form the hot junction. Difficulties in the latter operation have been experienced, however. Techniques for fabrication of reliable, long-lived hot-film surface probes are also under investigation. One such probe was employed to measure the instantaneous local heat-transfer coefficient inside a 2-in.-diam pipe in the range of Reynolds modulus from 2500 to 157,000. The data show a definite laminar behavior for Reynolds moduli below 2600, and a change to turbulent flow for Reynolds moduli greater than ~15,000, with a transition region characterized by intermittency of turbulence in between. Percentage fluctuations in local heat-transfer coefficient (averaged over a small frequency range) were correlated with frequency; and it was found that the largest fluctuations (~8% of the mean coefficient when averaged) occur at the low end of the frequency specturm (~2 cps). Analysis of the data was also made in terms of the power spectral density using an analog computer, from which it was observed that only at high values of the Reynolds modulus is there a significant contribution to the turbulent thermal energy by high-frequency fluctuations. Data have been recorded from which, it is hoped, an analysis can be made of the degree of correlation between the fluctuations in axial velocity near the wall and the fluctuations in the heat-transfer coefficient.

Turbulent Transport Studies. An air flow facility was constructed and operated to investigate the previously observed discrepancy between literature values and the results of this study on the turbulence level in water flows within a circular channel. New hot-wire probes with thinner

and longer supports and very fine tungsten wires (1.2 to 1.6 $\times 10^4$ in. diameter) were developed for these air studies. Analysis of the data has not yet been completed.

Thermophysical Properties

Alkali Liquid Metals. Results on the surface tension of potassium against helium obtained by the maximum bubble-pressure technique have been extended to temperatures near the boiling point. In the temperature span between 70 and 710°C, the surface tension (in dynes/cm) can be represented by the least-squares derived equation, $\sigma = 115.36 - 0.0646\ t$, with a mean-square deviation of ±0.72 dynes/cm. The data fall significantly higher (about 20% on the average) than values found in earlier studies as reported in the literature. Similar data obtained with lithium, $\sigma = 437.80 - 0.144\ t \pm 2.4$ in the temperature range 200 to 1000°C, agree more closely with literature values (~5%).

Data obtained on the density of potassium by varying the depth of capillary immersion in the surface tension measurements were found to be only 0.4% above published values. For lithium, the agreement was also quite good showing a maximum deviation of 2%.

Experiments to measure the contact angle for potassium droplets against various metals were continued. A condensed-vapor cloud in the vicinity of the droplet has made clear photography difficult for temperatures above 400°C; however, some tentative results have been obtained for an untreated, 32 μrms finish, type 304 stainless steel surface. Immediate spreading was observed when the droplet was placed on a surface preheated to 600°C. A second droplet contacting this same surface ~3 hr later after the temperature had been reduced to 300°C showed a contact angle of 10 deg. After cleaning the surface, a third droplet gave a contact angle of 130 deg at 100°C. With increasing temparature, the angle was reduced to 90 deg for a surface temperature of 150°C after 35 min and to 15 deg at 250°C after 60 min.

STUDIES IN HEAT TRANSFER AND FLUID MECHANICS
PROGRESS REPORT FOR PERIOD OCT. 1, 1963 – JUNE 30, 1964

H. W. Hoffman J. J. Keyes, Jr.

I. INTRODUCTION

The studies described in the sections following reflect the progress made during this reporting period in the specific program on heat transfer and fluid mechanics supported at the Oak Ridge National Laboratory by the Engineering Development Branch of the U. S. Atomic Energy Commission. It is the purpose of these investigations to generate some of the fundamental data on heat transport and fluid flow needed in advancing both new and existing reactor concepts. The primary emphasis continues to be on certain aspects of turbulence in both linear and vortexing flows and on two-phase flow and boiling heat transfer with water and potassium.

This report is the second in the current series (see Bibliography); the next report will cover the period through June 30, 1965, and, hopefully, will be available by September, 1965.

2. BOILING HEAT TRANSFER AND TWO-PHASE FLOW

2.1. Boiling-Potassium Heat Transfer

2.1.1. Forced-Convection System

A. I. Krakoviak H. W. Hoffman

Introduction

The study of boiling with potassium in forced flow upward through a circular tube was resumed following installation of a medium-flux boiler (100,000 Btu/hr·ft^2 maximum capability); additional critical heat flux and two-phase pressure-drop data have been obtained. Fabrication of a new high-flux boiler ($q/A \sim 500{,}000$ Btu/hr·ft^2) continues to be beset by difficulties. The design of this new test unit differed from the previous boiler[1] in three aspects: (1) provision was made for the direct measurement of the tube-wall temperature at three equally spaced, short, adiabatic regions along the tube wall, (2) a pressure tap was added at the midpoint of the boiler, and (3) Pt-Pt 10% Rh thermocouples were substituted for the original Chromel-Alumel couples. The first such boiler constructed was extensively damaged prior to installation; the unit was dropped in shipping causing the mashing of several thermocouples and the tearing off of the central pressure tap leaving a hole in the tube wall. Only the copper blocks were salvaged. Boroscopic examination of the second boiler following the brazing operation revealed significant quantities of braze alloy on the inner tube surface. Although the tube is leak tight and the braze alloy is compatible with potassium, there remains serious doubt as to whether the inside surface can be smoothed sufficiently by mechanical means to effect a usable heat-transfer surface. Efforts to correct this situation will be continued.

---

[1]A. I. Krakoviak and H. W. Hoffman, Boiling-Potassium Heat Transfer: Forced-Convection System, pp. 5–21, "Studies in Heat Transfer and Fluid Mechanics, Progress Report for Period Jan. 1 – Sept. 30, 1963," USAEC Report ORNL-TM-915, Oak Ridge National Laboratory, October 1964.

Apparatus Modifications

In view of the above described difficulties in constructing a new high-flux boiler, a test unit of lower flux capability has been installed for interim operation. This boiler (termed medium flux) was machined from a 7-ft length of 1/2-in. double extra heavy IPS type 347 stainless steel pipe (0.270 in. ID, 0.839 in. OD). As shown schematically in Fig. 2.1, the boiler was divided into six 12-in.-long sections which were heated radiantly by individual clamshell heaters of 1 1/4-in. inside diameter. These heated portions were separated by 1.5-in. gaps in which the wall was thinned from the original 0.285 in. to 0.075 in. Pressure taps, located in the final four gaps and at the boiler exit, were provided with cooling jackets; the pressures were measured with four Taylor devices and with a 6-in. bronze Bourdon-tube gage (maintained at the calibration temperature of 160°F). A pair of 0.008-in.-diam Pt-Pt 10% Rh thermocouples were also welded to the tube wall in each of the interheater gaps; the leads of these thermocouples were brought out along the pressure-transmitting lines. Fiberfrax insulation in these regions created an essentially adiabatic zone.

Tube-wall temperatures at the midpoint of each heated section were obtained with Pt-Pt 10% Rh thermocouples placed in 0.035-in.-diam holes drilled radially into the tube wall; the location of the bottoms of these wells with respect to the inside tube surface are indicated in Fig. 2.2. The 8-mil thermocouple wires were threaded through two-hole ceramic insulators (0.031 in. OD) and individually resistance welded to the stainless steel at the bottom of the well. The leads were insulated with quartz-cloth sleeving and brought out radially through the clamshell heater halves. The inside surface temperature was obtained by extrapolation from the temperatures measured at the bottom of the thermocouple wells.

Some error in the temperature measurement results from heat flow along the thermocouple leads to the junction and from distortion of the heat flow pattern in the tube wall by the drilled thermowells. If by proper insulation the thermocouple leads at the radius of the outside surface are maintained at the temperature of the outside stainless steel

ORNL-DWG 64-7305

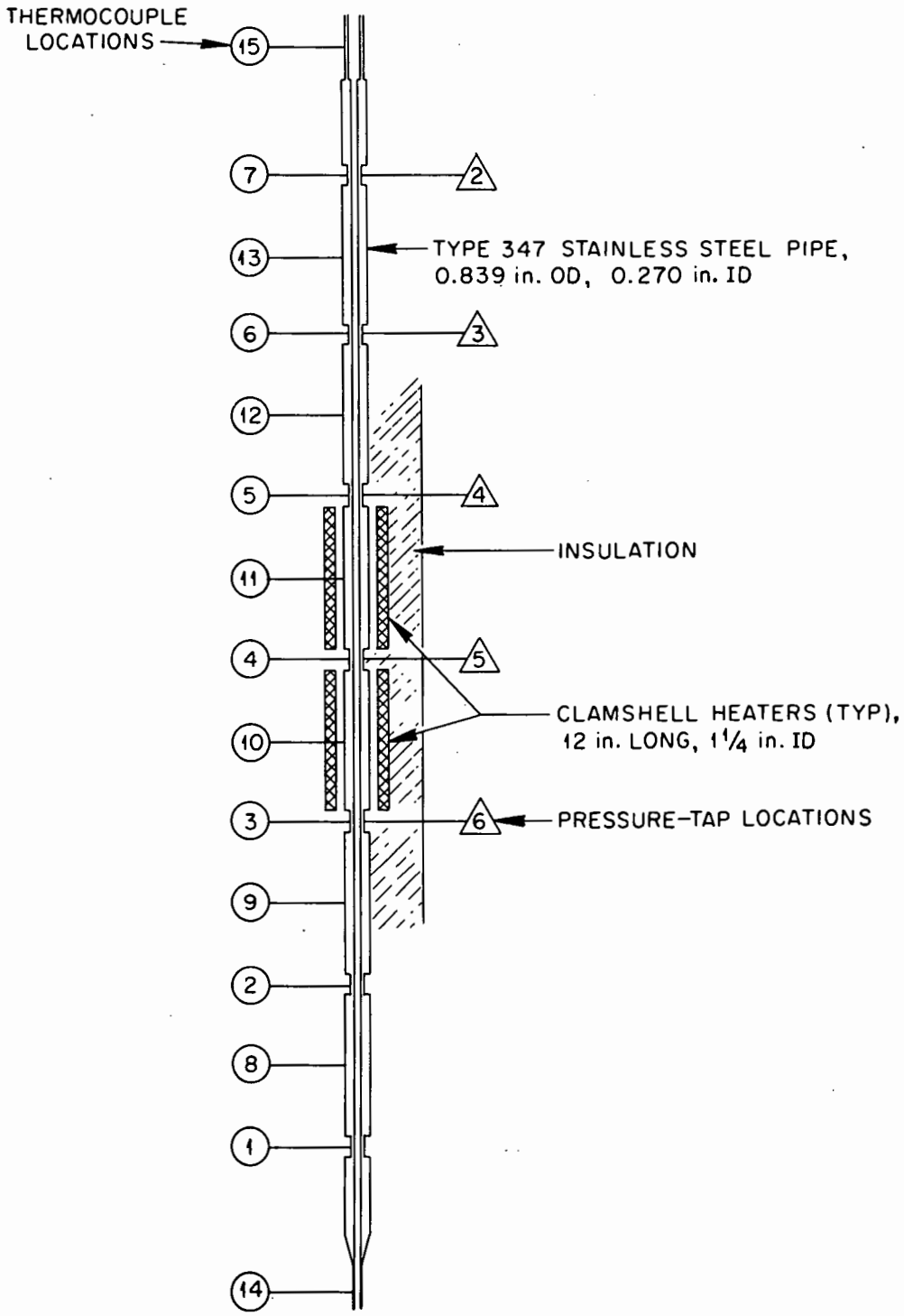

Fig. 2.1. Schematic of Medium-Flux Boiler Section.

ORNL-DWG 64-7306

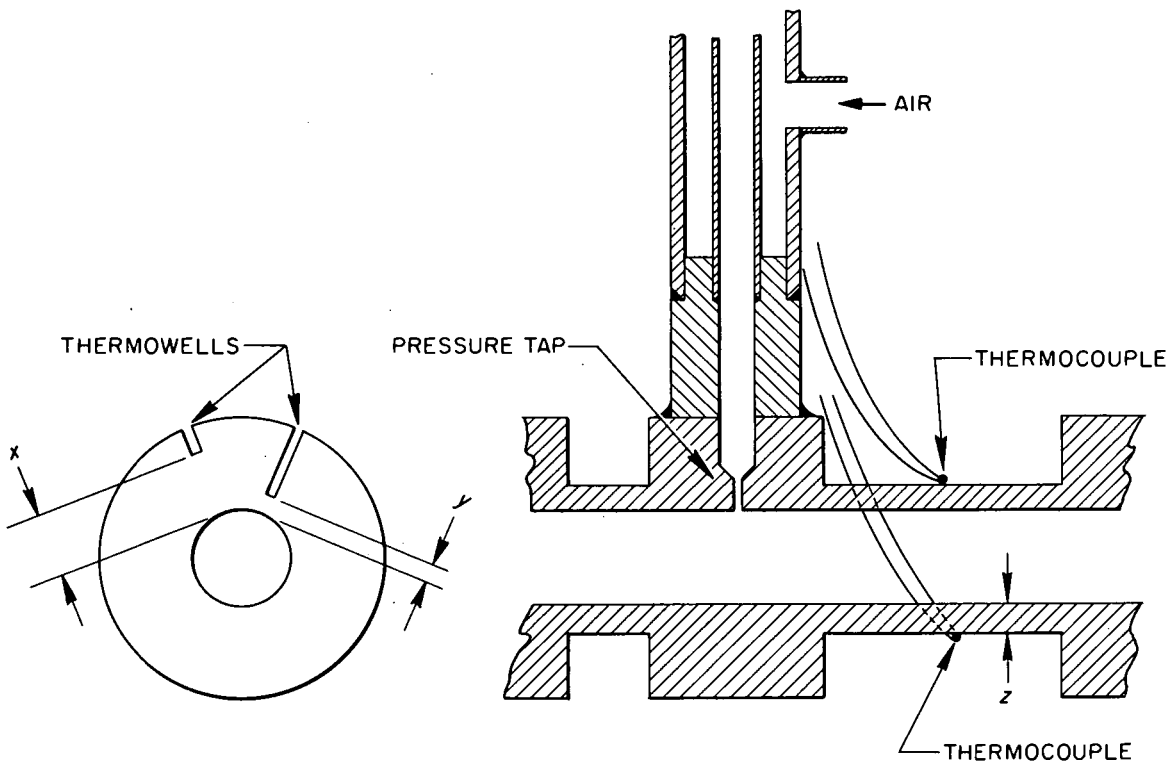

THERMOCOUPLE POSITION	WALL THICKNESS (in.)
1-7	$z = 0.075$
8	$x = 0.1210$, $y = 0.041$
9	$x = 0.2005$, $y = 0.051$
10	$x = 0.2146$, $y = 0.018$
11	$x = 0.2070$, $y = 0.054$
12	$x = 0.2106$, $y = 0.033$
13	$x = 0.2040$, $y = 0.021$

Fig. 2.2. Thermocouple and Pressure Tap Details of Medium-Flux Boiler.

surface, these errors can be kept to less than 5% of the total temperature drop through the tube wall. (For a maximum heat flux of 100,000 Btu/hr·ft^2 at the inside tube surface, the total temperature drop through the tube wall is about 100°F.) Care must be taken, however, to insure that good welds exist between the thermocouple wires and the stainless steel at the bottom of the thermowell and that the thermocouple leads are not directly exposed to the heater. A slight eccentricity in the boiler (inside diameter with respect to outside diameter) introduces an additional error of about 3°F at the maximum heat flux.

Heat-Transfer Results

The data obtained thus far with the medium-flux boiler (designated Series C) are given in Table 2.1. Typical axial temperature profiles are shown in Figs. 2.3 (run C-7 at q/A = 56,600 Btu/hr·ft^2) and 2.4 (run C-12 at q/A = 80,600 Btu/hr·ft^2). Wall temperatures measured in the adiabatic interheater gaps are indicated by the solid circles; these temperatures should correspond to the inside wall temperatures at these locations. Inside wall temperatures obtained by extrapolation from the measurements in thermowells at the midpoint of each heated section (indicated by crosses) are in reasonable agreement with the interheater-zone values.

Provision was made in the medium-flux boiler for pressure measurements at a number of positions along the boiler (see Fig. 2.1) for the twofold purpose of obtaining better data on the two-phase pressure loss and of establishing more clearly the fluid temperature profile in the boiler. The absolute pressures measured at the five locations are given in Table 2.1. The temperatures corresponding to these pressure values, assuming liquid-vapor equilibrium, are also shown in Figs. 2.3 and 2.4 (open circles); the simplified equation of Lemmon et al.,[2]

$$\log P = 4.185 - \frac{4332}{T} , \qquad (2.1)$$

[2]A. W. Lemmon, Jr., H. W. Deem, E. H. Hall, and J. F. Walling, The Thermodynamic and Transport Properties of Potassium, "Proceedings of 1963 High-Temperature Liquid-Metal Heat Transfer Technology Conference," USAEC Report ORNL-3605, Oak Ridge National Laboratory (in publication).

Table 2.1. Operating Variables and Results of Two-Phase Potassium Flow Studies

Run No. Series C	10^{-5} × Inlet Mass Flow, lb/hr·ft^2	Inlet Fluid Temperature, °F	Exit Fluid Temperature, °F	Exit Quality, Wt % Vapor	Heat Flux Q/A (ΔH Fluid), Btu/hr·ft^2	Heat Balance, $Q_{electric}/Q_{fluid}$	Boiler Pressure, psia PE-6	PE-5	PE-4	PE-3	PE-2
1	2.236	1428.7	1358.3	11.50	17,235	0.84	17.02	16.25	15.38	14.41	12.79
2	1.886	1492.9	1417.3	23.40	32,828	0.97	23.20	22.45	21.15	19.42	17.11
3	1.583	1465.8	1398.2	25.52	30,427	1.04	20.72	19.95	18.83	17.58	15.50
4	1.134	1441.1	1382.4	34.82	30,559	1.03	18.40	17.93	16.80	15.85	14.25
5	1.957	1559.6	1471.6	38.62	57,993	1.03	31.55	30.30	28.03	25.50	22.23
6	1.609	1543.0	1460.8	45.80	57,252	1.05	29.55	28.15	26.20	24.05	21.09
7	1.150	1514.6	1442.4	62.24	56,555	1.07	25.70	24.95	23.15	21.49	19.11
8	0.9157	1491.7	1424.7	77.20	56,395	1.06	23.05	22.25	20.90	19.55	17.53
9	0.7688	–	–	91.03	–	*	22.35	21.45	20.15	18.95	17.05
10‡	0.6967	–	–	100.00	–	**	–	–	–	–	–
11	1.896	1617.1	1529.7	55.34	81,444	1.06	40.51	38.24	35.31	32.11	28.37
12	1.640	1596.7	1515.2	62.80	80,568	1.05	37.41	35.56	32.68	29.91	26.54
13	1.178	1573.4	1501.65	87.50	81,688	1.08	33.81	32.16	30.11	27.56	24.78
14	1.056	1563.6	1529.4	95.80	80,223	1.09	32.86	31.26	29.16	27.21	24.46
15‡	0.9918	–	–	98.00	–	***					

*$Q_{electric}$ = 59,667 Btu/hr·ft^2.

**$Q_{electric}$ = 59,632 Btu/hr·ft^2.

***$Q_{electric}$ = 87,990 Btu/hr·ft^2.

‡Burnout.

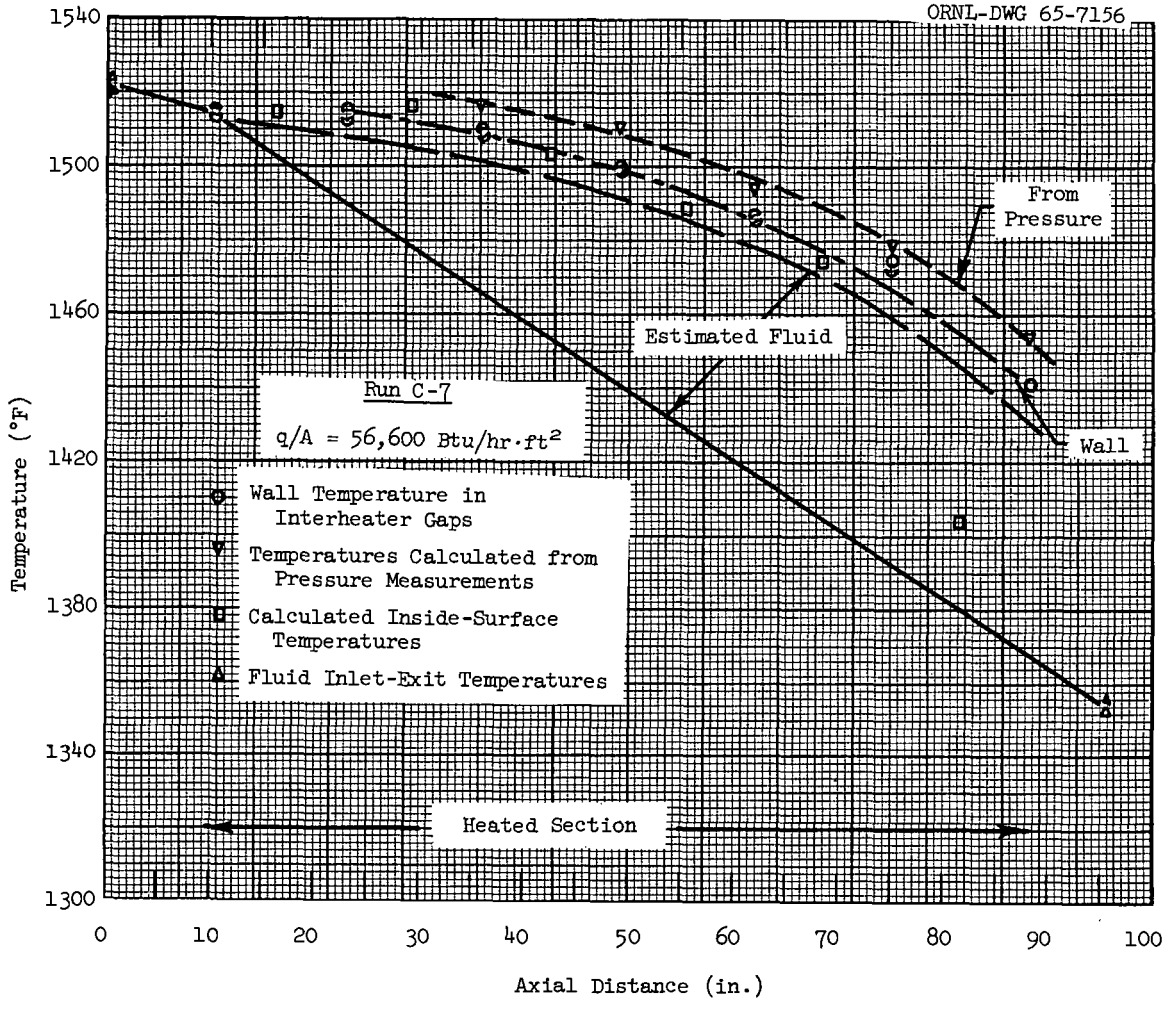

Fig. 2.3. Axial Temperature Profile; Run C-7.

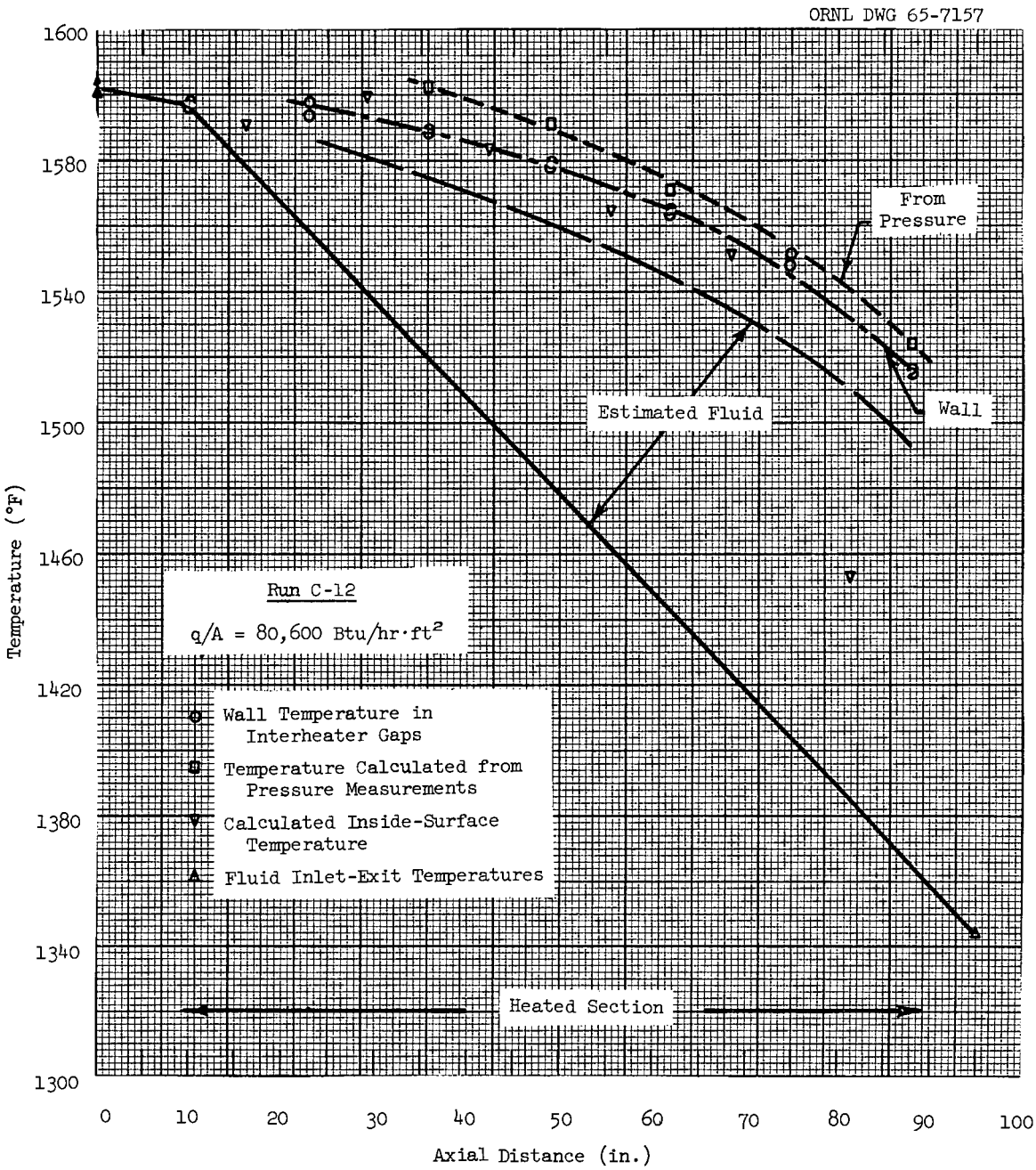

Fig. 2.4. Axial Temperature Profile; Run C-12.

was used in this calculation. In Eq. (2.1), P is given in atmospheres for T in °K. In the temperature range 900 to 1100°K, this equation yields pressures which are about 0.5% low in respect to the more complete equation developed by Lemmon and his co-workers;[2] the data plotted in Figs. 2.3 and 2.4 include this correction. The most obvious characteristic of these data is that they fall significantly above the inside-tube-wall temperature values though supposedly measuring the fluid saturation temperature. The source of this discrepancy has not yet been clarified; it may reflect a systematic error in the measurement of the absolute pressure. Note, however, that the results clearly show curvature in the axial fluid temperature profile.

Thermocouples in the thinned-wall section immediately preceding the first heated zone lie at the end of an ~1-ft-long essentially adiabatic region and, thus, probably provide a good measure of the inlet fluid temperature. The inlet fluid temperatures indicated at the zero axial position also fall within this adiabatic zone. Shown in both Fig. 2.3 and Fig. 2.4 is a linear interpolation of the fluid temperature as drawn previously with respect to the data obtained in the high- and low-flux boilers.[1] A more reasonable estimate is indicated by the curved lines (long dashes) passing through the initial wall-temperature value; these curves have been drawn parallel to the fluid-temperature curves calculated from the pressure data. The fluid temperatures deduced from the pressure measurements would correspond to the upper estimated fluid-temperature curve for run C-7, if the pressures recorded were consistently high by about 2 psi; similarly, for run C-12, an error of ~+3.5 psi is sufficient to account for the discrepancy. In contrast, an error of 25 to 35°F in the measurements with the Pt-Pt 10% Rh thermocouples does not seem likely, even though an absolute calibration was not made; the thermocouples were calibrated only with respect to each other.

The results for heat fluxes below the critical are given in Fig. 2.5; ΔT_{sat} is the mean-temperature difference between the wall-temperature curve and the upper estimated fluid-temperature curve. The range of the data obtained with the high-flux boiler is also indicated in this figure, and it is noted that the current results suggest a lesser dependence on

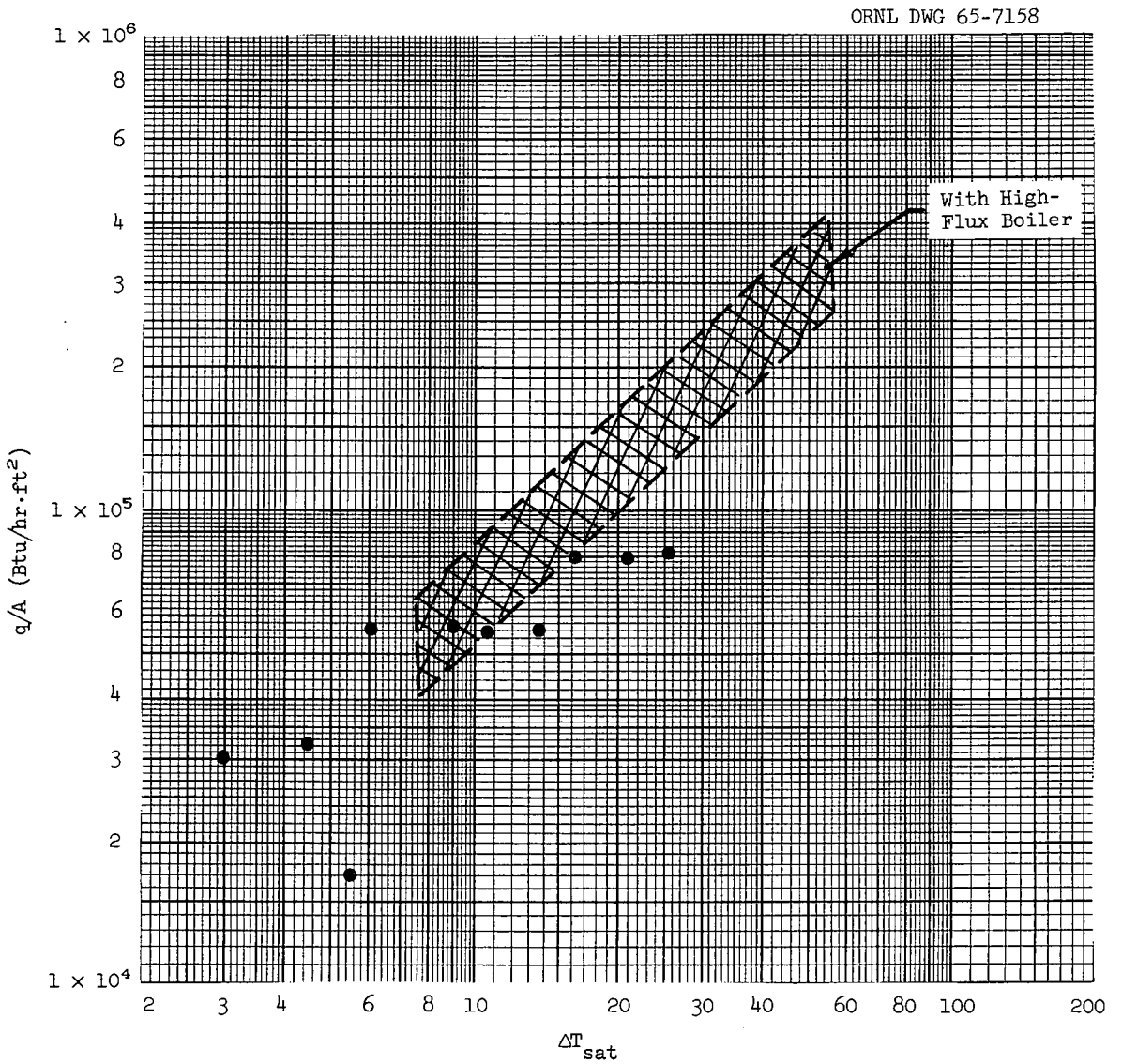

Fig. 2.5. Boiling-Potassium Heat Transfer.

ΔT than was observed with the earlier data. However, since many of the values are associated with very small temperature differences (3 to 10°F) and since an uncertainty exists in the procedure for obtaining these differences, this conclusion may well be premature. Again, though there are some anomolous values, decreasing ΔT at any given flux level seems to correspond to increasing exit quality.

Two sets of runs terminated with "burnout": C-5 through C-10 and C-11 through C-15; the critical values are given in Fig. 2.6 in comparison with the results obtained with the previous boilers. Note that the agreement with the Lowdermilk, Lanzo, and Siegel correlation[3] for water remains good. For run C-10, the critical flux was ~56,250 Btu/hr·ft^2 (calculated from $Q_{electric}$ using the heat balance ratio) at a mass flow of ~0.7×10^5 lb/hr·ft^2 with an exit quality of essentially 100%; for run C-15, $\phi_{crit} \cong$ 82,230 Btu/hr·ft^2 at $G \cong 1.0 \times 10^5$ lb/hr·ft^2 and X = 98%. During run C-15 (quality ~96%), temperature oscillations of 30°F total amplitude were detected at the boiler exit.

Pressure-Drop Data

As discussed above, the axial pressure distribution was measured over the downstream two-thirds of the boiler. While there appears to be an error in the absolute values of the pressure, the differences recorded between pressure-tap locations should be valid. The results are presented in Fig. 2.7 following the method of Lockhart and Martinelli[4] which defines a friction multiplier as the ratio of the total two-phase pressure drop, $(dP/d\ell)_{TPT}$, to the pressure drop for the liquid phase only, $(dP/d\ell)_\ell$, at the same inlet liquid mass flow. This friction multiplier can be correlated with the dimensionless parameter,[4,5] X_{tt}, where

[3]W. H. Lowdermilk, D. D. Lanzo, and B. L. Siegel, "Investigation of Boiling Burnout and Flow Stability for Water Flowing in Tubes," Report NACA-TN-4382, National Advisory Committee for Aeronautics, September 1958.

[4]R. W. Lockhart and R. C. Martinelli, "Prediction of Pressure Drop for Isothermal Two-Phase, Two-Component Flow in Pipes," Chem. Eng. Progr., 45: 39 (1949).

[5]R. C. Martinelli and D. B. Nelson, "Prediction of Pressure Drop During Forced-Circulation Boiling of Water," Trans. ASME, 70: 695–702 (1948).

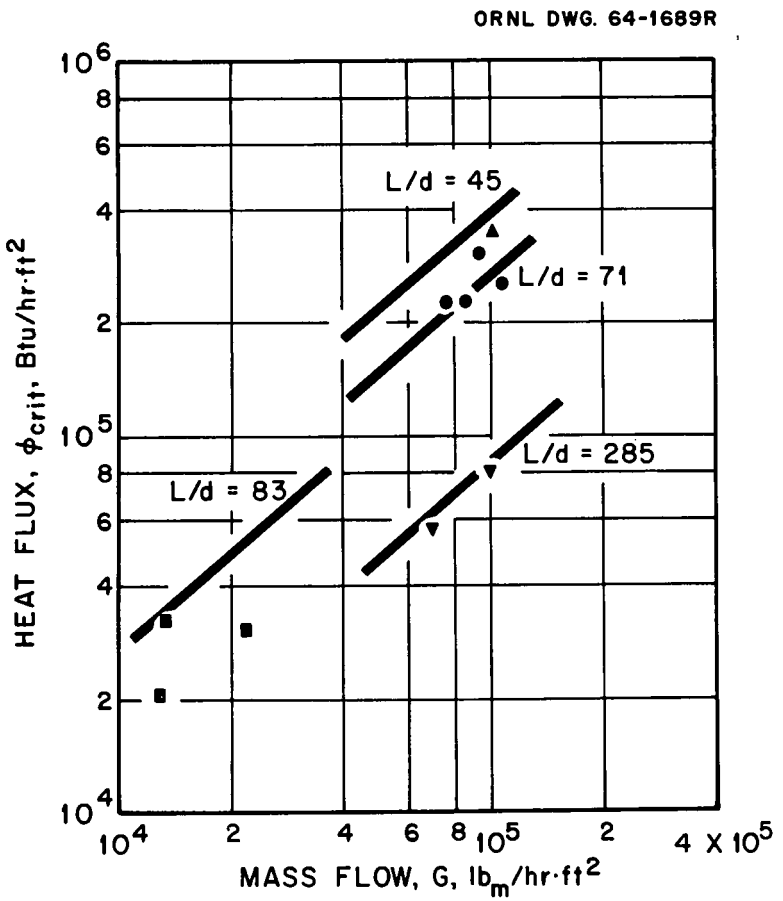

Fig. 2.6. Critical Heat Flux with Boiling Potassium.

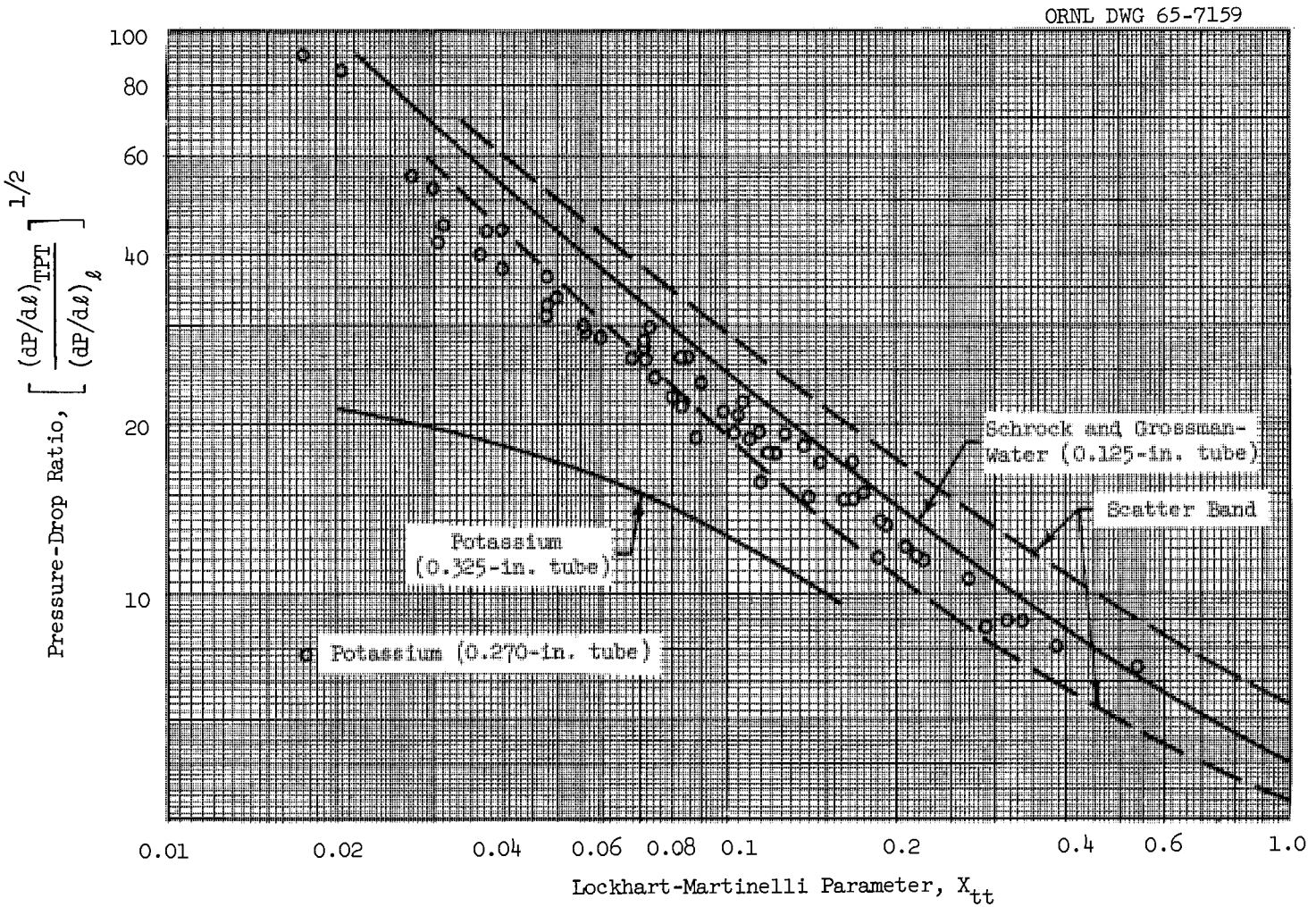

Fig. 2.7. Pressure Drop with Forced-Convection Vaporization of Potassium Flowing Upward in a Vertical Tube at Constant Heat Flux.

$$X_{tt} = \left(\frac{1}{x} - 1\right)^{0.9} \left(\frac{\mu_\ell}{\mu_v}\right)^{0.1} \left(\frac{\rho_v}{\rho_\ell}\right)^{0.5} . \qquad (2.2)$$

In Eq. (2.2), x is the exit quality; μ, the viscosity; ρ, the density, and the subscripts, v and ℓ, refer to vapor and liquid, respectively. The fluid properties were evaluated at the fluid bulk (saturation) temperature. The qualities at the exit of each 1-ft-long section between pressure taps ranged between 12% and 96% and were obtained by linear interpolation along the test section between the inlet (zero) quality and the measured exit quality. Over the pressure range of the current data (12.8 and 40.5 psia), the density ratio in Eq. (2.2) varied nearly threefold.

The data are compared in Fig. 2.7 with the results of Schrock and Grossman[6] for the boiling of water in upward flow through a small diameter (0.125-in.) tube and with the earlier potassium data[1] in a 0.325-in. tube in which end effects were included. It is noted that the present results fall 10 to 20% below the mean for the Schrock and Grossman data though generally within their indicated scatter band.

As a matter of interest, the pressure-drop data of Table 2.1 have been evaluated in terms of the simpler homogeneous model. Preliminary results for the pressure drop across sections 6-5 and 3-2 for run C-12 are shown in Fig. 2.8.

2.1.2 Superheat Phenomena

A. I. Krakoviak

Data obtained previously in a number of boiling potassium forced-convection and natural-convection systems at ORNL have suggested the existence of abnormally high superheats. A simple analysis for predicting the magnitude of the superheat required to initiate boiling with the alkali liquid metals[7] verified the above conclusion and indicated the

[6]V. E. Schrock and L. M. Grossman, "Forced-Convection Boiling in Tubes," Nucl. Sci. Eng., 12: 474–481 (1962).

[7]A. I. Krakoviak, Boiling-Potassium Heat Transfer: Superheat Phenomena, pp. 21–26, "Studies in Heat Transfer and Fluid Mechanics, Progress Report for Period Jan. 1 – Sept. 30, 1963," USAEC Report ORNL-TM-915, Oak Ridge National Laboratory, October 1964.

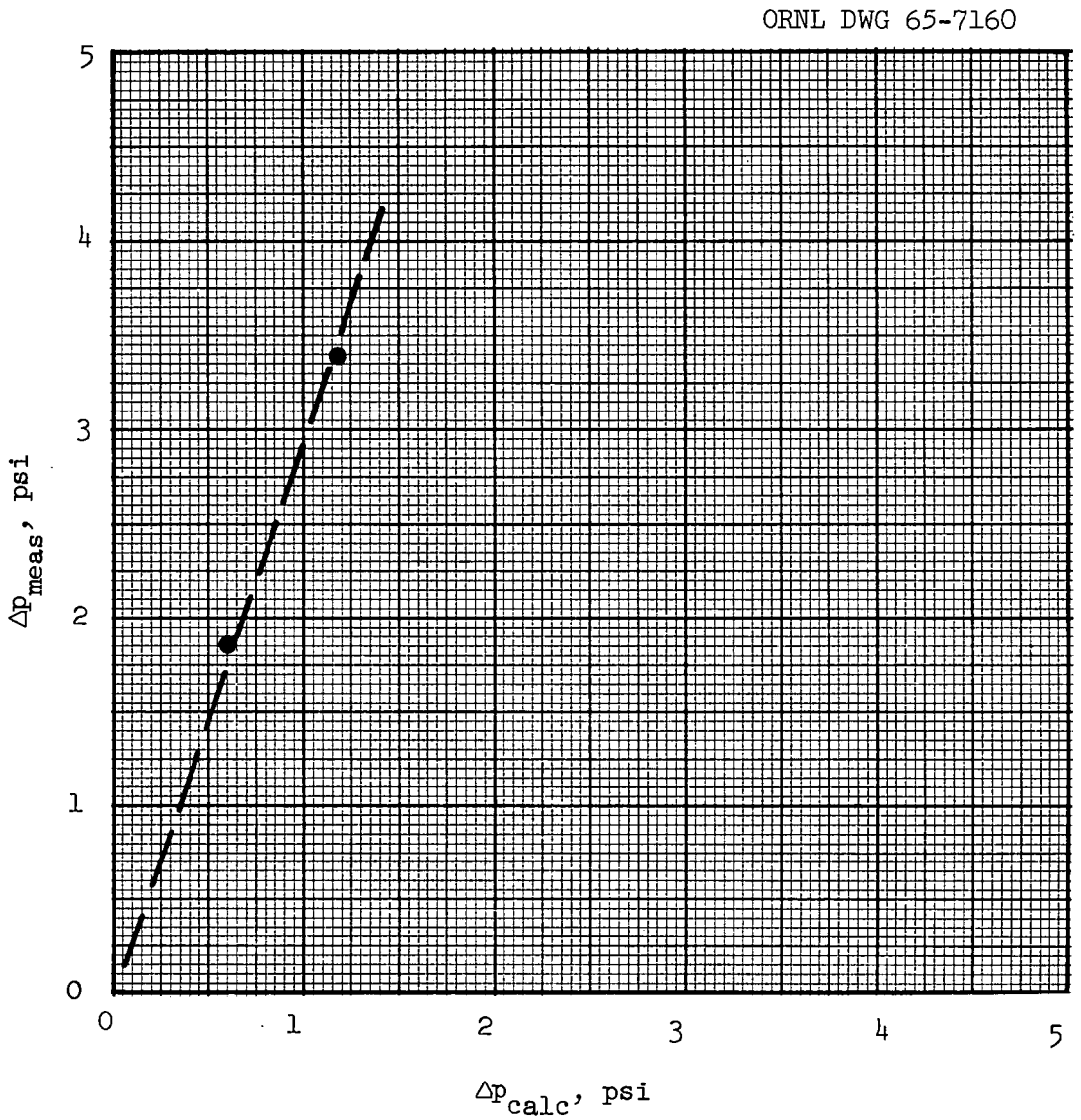

Fig. 2.8. Comparison of Measured Pressure Drops with Values Calculated by Homogeneous Model.

need for further quantitative measurements. Accordingly, an experimental program was undertaken to determine the liquid superheat with potassium and to establish the effect of surface condition on the magnitude of the superheat.

Apparatus

A small (20-in. × 20-in.) natural-circulation loop was designed for the purposes of this study. The system (shown schematically in Fig. 2.9) was constructed of 1/2-in. sched-40, type 347 stainless steel pipe arranged so as to accommodate the three test regions A, B, and C in Fig. 2.9. The structure of these test sections is given in Table 2.2. In operation, the

Table 2.2. Boiling Surface Characteristics

Region	Surface Treatment
A	Porous surface coating
B	Two opposed rows of four small diameter holes spaced at 2-in. separation
C	As received

fluid was boiled in section A, while region B remained unheated; the vapor generated was condensed by cooling the tube wall at the top of leg B. Alternately, surface B was examined by heating this region, while section A remained unheated. Finally, by rotating the loop clockwise by 90 deg, region C could be studied.

The surface B was formed by drilling holes through the pipe wall which were then closed on the outside with weld metal to form cavities of the desired depth. X-ray examination of the completed section showed one hole to be as in Fig. 2.10-b, three as in Fig. 2.10-c, and the remaining four as in Fig. 2.10-d. These holes were arranged in two diametrically opposed rows of four holes extending axially along the tube with the holes in each row at 2-in. separation and with one row displaced in the axial direction by 1 in. with respect to the other.

Tube wall temperatures were obtained with Chromel-Alumel thermocouples (0.010-in. wire) resistance welded to the outside tube wall at the positions

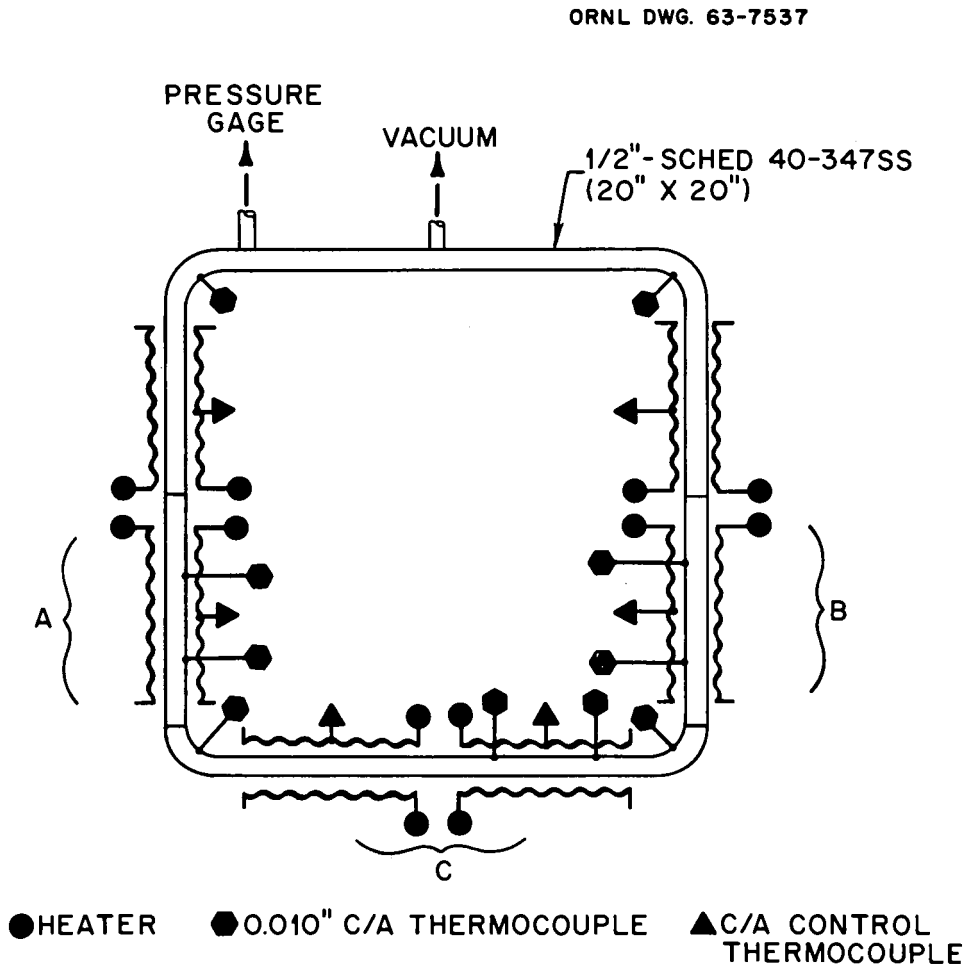

Fig. 2.9. Natural-Convection Superheat Loop.

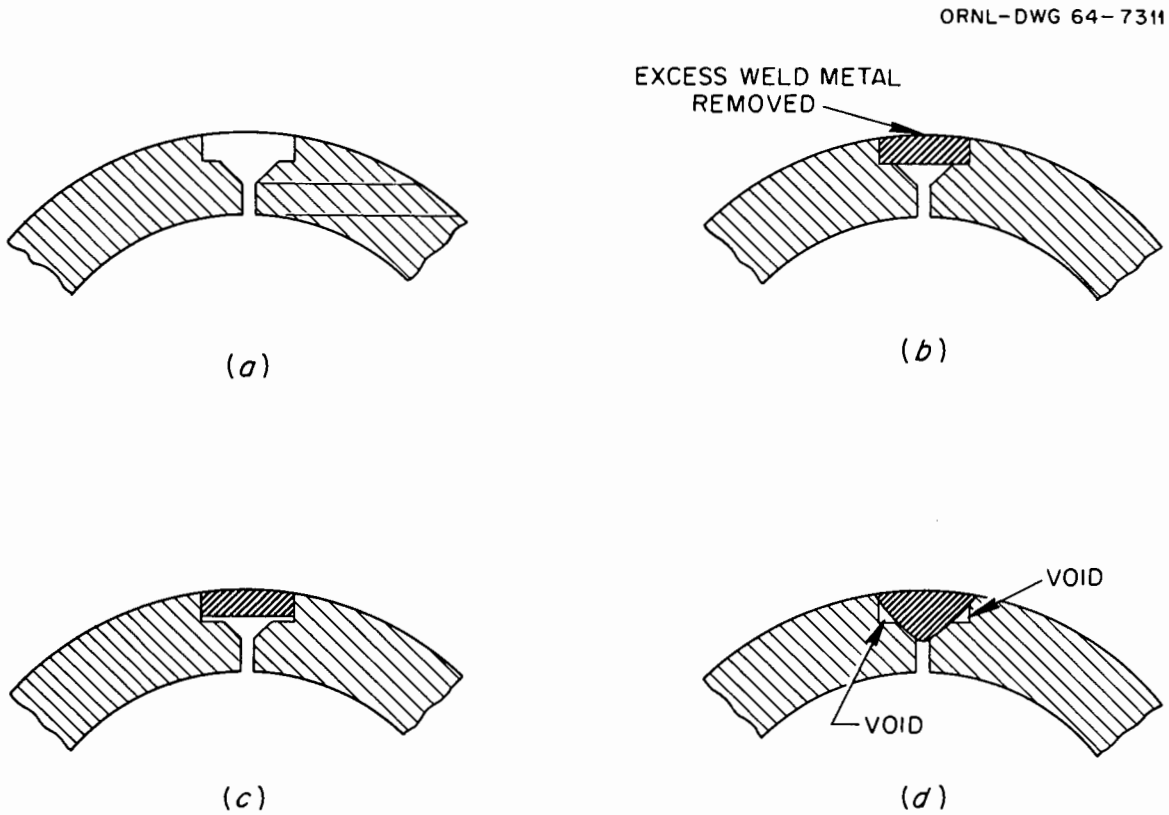

Fig. 2.10. Shape of Cavities after Back-Welding of Holes Drilled Through Pipe Wall.

indicated in Fig. 2.9. The loop pressure was measured with a calibrated bronze Bourdon tube gage (0 to 30 psia range) which was maintained at the calibration temperature of 160°F. In general, the saturation temperature, as determined from the loop pressure, averaged 3°F above the value indicated by the condenser thermocouples; the maximum deviation observed was 10°F. Each test region was heated by a pair of electric resistance (clamshell) heaters. The power input to the heaters, after correction for external heat loss, was used to establish the heat flux and the temperature drop through the boiler wall. The saturation temperature level was controlled by adjusting the loop pressure.

Temperature Patterns

Initial data were obtained with a loop containing only an as-received and a porous surface; the test region containing discrete holes was inoperative in that the holes were completely refilled with weld metal during the back-welding operation so as to return it to an essentially as-received condition.

Typical of the temperature oscillations recorded in the boiler and condenser regions are those given for the surfaces C (labeled smooth) and A (labeled treated) in Figs. 2.11 and 2.12, respectively. The heat flux in these experiments ranged from 16,000 to 37,000 Btu/hr·ft^2. The temperatures shown are the recorded outside tube wall temperatures; the calculated temperature drop through the wall was generally less than 13°F.

Figure 2.11 displays the temperature pattern observed with the smooth surface. The superheat at nucleation was obtained as the temperature difference between the maxima in the boiler (heater) curve and the minima in the condenser curve. (The saturation temperature was taken to be the value indicated by the condenser curve.) Uncorrected superheats of 210 to 240°F were determined for the specific data pictured. The tube wall temperature fluctuated with an average amplitude of ~140°F at a frequency of 0.25 cps. This pattern of wall temperature oscillations is very similar to that which had been previously found during some periods of operation with the low-flux boiler.[1]

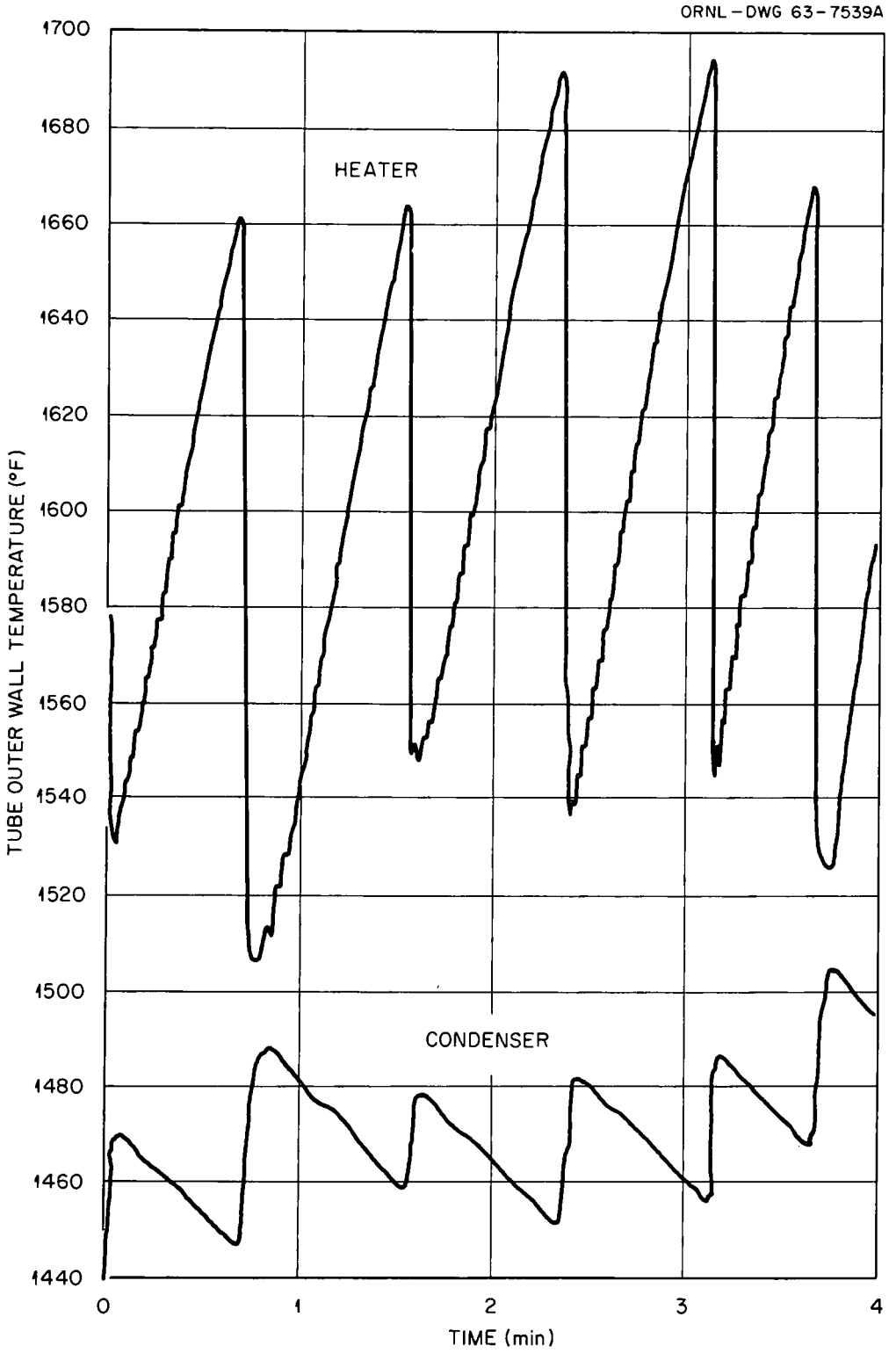

Fig. 2.11. Outside Tube Wall Temperatures in Natural-Convection Boiler. Smooth surface at a saturation temperature of 1450 to 1470°F.

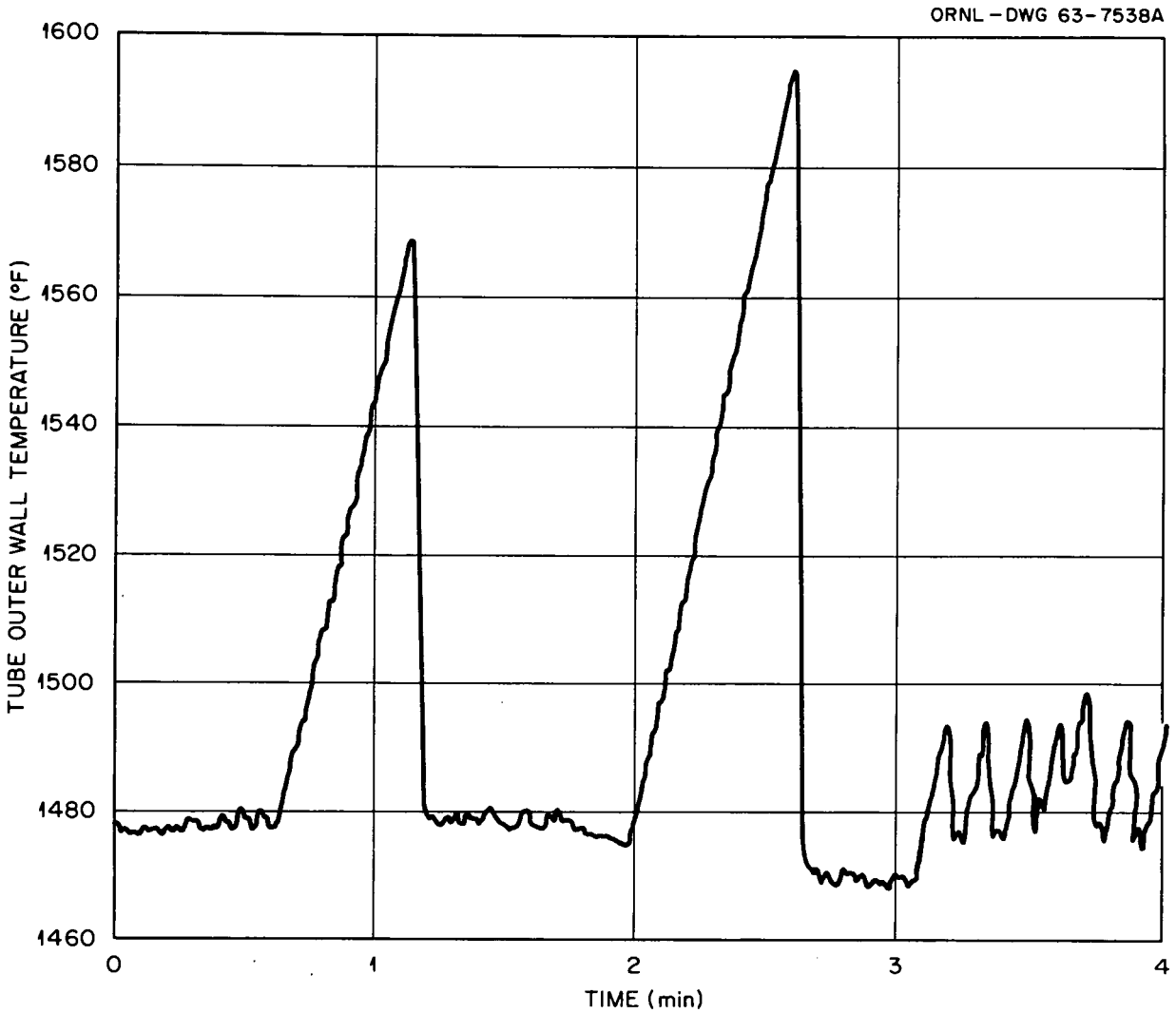

Fig. 2.12. Outside Tube Wall Temperatures in Natural-Convection Boiler. Treated surface at a saturation temperature of 1420 to 1450°F.

Contrasting with this behavior was the temperature pattern observed with the treated surface; a continuous four-minute portion (not a composite) of a temperature trace is given in Fig. 2.12. Three distinct conditions were noted:

1. Temperature spikes of large magnitude (95 to 125°F) and irregular occurrence having a pattern and associated sound similar to those observed with the smooth surface and a superheat level between 140 and 180°F.

2. Periods of "quiet" operation of various duration separating these peaks for which the thermal oscillations were of low magnitude (2 to 3°F) and relative high frequency (~1.3 cps) and the superheat was of the order of 25 to 30°F.

3. Some fluctuations of intermediate magnitude (~20°F) and frequency (0.13 cps) with a superheat of 60°F.

A fourth mode, not shown in Fig. 2.12, was also seen in which the tube wall temperature remained constant without fluctuations for times as long as one minute. The saturation temperature associated with the data of Fig. 2.12 was 1420 to 1450°F.

Following accumulation of the above data, the faulty drilled surface was removed from the loop and replaced by a section having the characteristics described for surface B in Table 2.2 and Fig. 2.10. The original smooth and treated surfaces were retained. The temperature patterns observed with this surface are shown in Figs. 2.13 and 2.14.

The first of these (Fig. 2.13) was obtained at a saturation pressure of 0.18 psia corresponding to a saturation temperature of 820°F; the minima in the condenser temperature curve (uncorrected for wall temperature drop) indicate a saturation temperature of ~805°F. The total amplitude of the wall temperature oscillation was of the order of 65°F with a primary frequency of about 0.02 cps. Superimposed on the fundamental mode was a high-frequency fluctuation of 0.60 to 0.75 cps. The superheat associated with these data was 140°F.

As the saturation pressure was increased, the fundamental oscillation decreased in amplitude and increased in frequency, while the secondary fluctuation remained essentially unchanged in both frequency and amplitude.

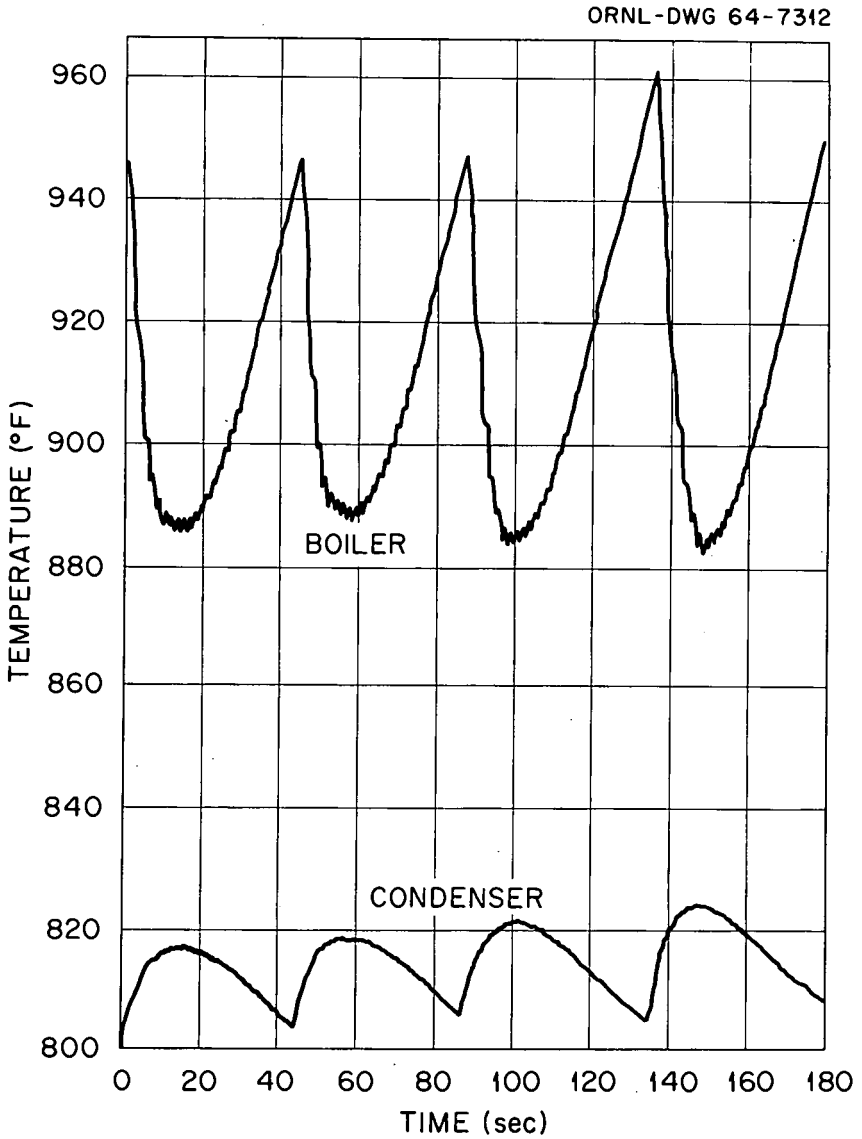

Fig. 2.13. Outside Tube Wall Temperature in Natural-Convection Boiler at a Saturation Temperature of 820°F.

ORNL Dwg. 65-7161

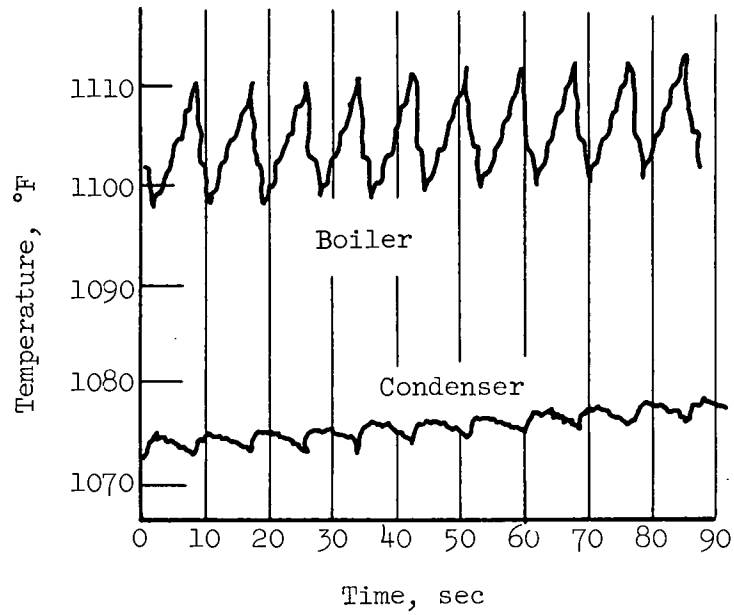

(a) T_{sat} = 1070°F

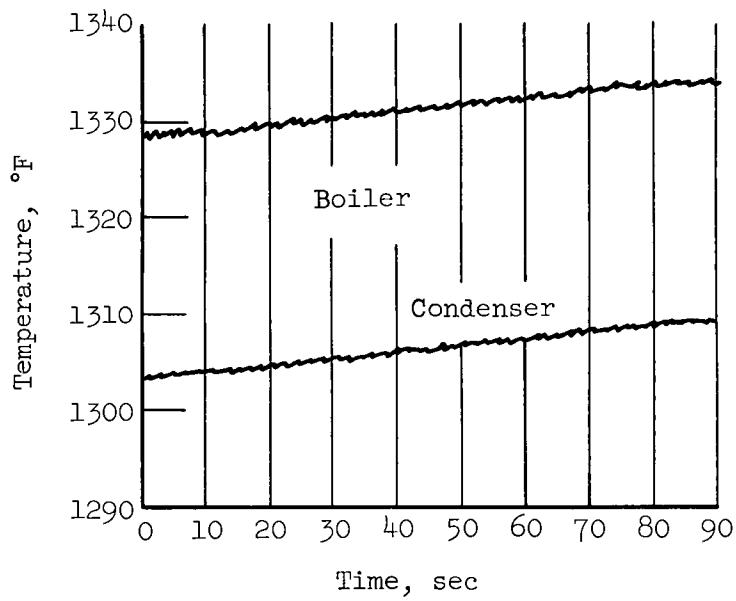

(b) T_{sat} = 1260°F

Fig. 2.14. Outside Tube Wall Temperature Traces in Natural-Convection Boiler at Several Saturation Temperature Levels.

At still higher temperatures (1200 to 1250°F), only the high-frequency oscillation was detectable. Finally, at saturation temperatures in excess of 1350°F, the high-frequency oscillations also disappeared; and straight-line traces in both boiler and condenser were recorded. Typical temperature profiles illustrating this are shown in Fig. 2.14. In the upper portion (Fig. 2.14-a), the saturation temperature was ~1070°F with an oscillation amplitude of ~12°F at a frequency of 0.12 cps; in the lower portion (Fig. 2.14-b), the saturation temperature was ~1260°F, the oscillation amplitude ~1°F, and the oscillation frequency ~0.8 cps. It has been estimated that the amplitude of the high-frequency temperature fluctuation is reduced by a factor of three between the inside and outside surfaces, whereas the low-frequency fluctuation is transmitted essentially without attenuation.

Superheat Correlation

The results obtained with all three surfaces are summarized and compared in Fig. 2.15; the liquid superheat (corrected to account for the temperature drop through the tube wall) is plotted against the saturation temperature at each operating condition. Comparison is also made with the superheat calculated[7] according to the equation,

$$T_{w,i} - T_{sat} \cong \frac{2\ R\ T_{sat}^2\ \sigma}{h_{fg}\ P_\ell\ r}\ , \qquad (2.3)$$

where $T_{w,i}$ is the absolute surface temperature; T_{sat}, the absolute temperature of the fluid at the pressure, P_ℓ; σ, the surface tension of the liquid at the vapor-liquid interface; h_{fg}, the latent heat of vaporization of the liquid; r, the bubble radius; and R, the gas constant. The cavity (bubble) radius was introduced as an independent parameter to generate the multiple curves shown.

The uppermost set of data in Fig. 2.15 (normal triangles) were obtained with the smooth surface and show remarkably little scatter along with good reproducibility. The measured superheat ranged from ~700°F at T_{sat} = 950°F to a low of ~270°F at 1480°F.

Corresponding results with the porous surface are more complex, while showing a significant decrease in the superheat required for bubble

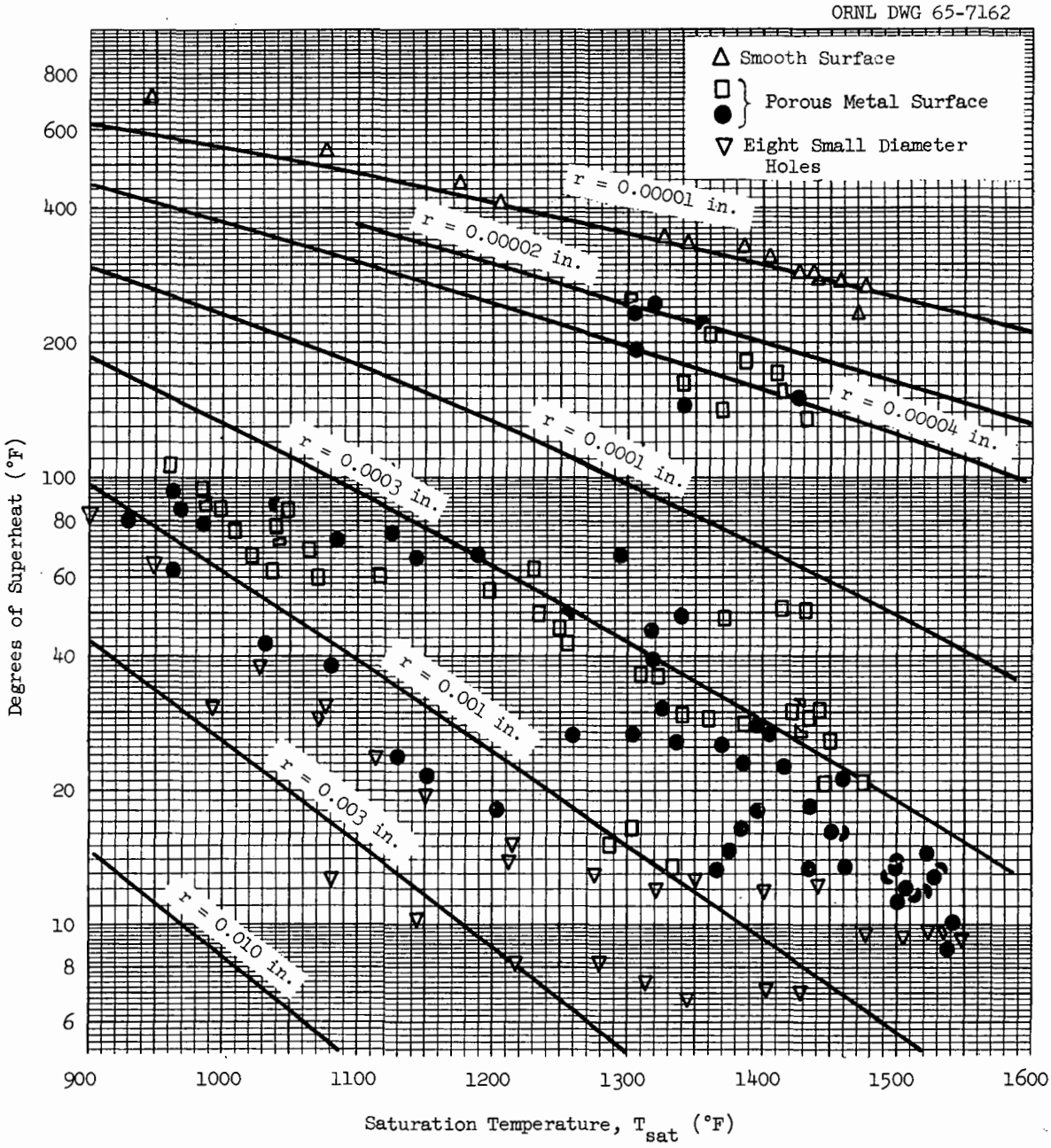

Fig. 2.15. Liquid Superheat with Potassium.

initiation. Two sets of data were obtained with this surface: (1) indicated by the squares, during the period of initial operation of the loop, and (2) represented by the filled circles, at a time subsequent to the opening of the loop and the installation of the new section with discrete, drilled holes. The superheat for the bulk of the data, over essentially the same temperature span as with the smooth surface, varied from somewhat more than 100°F to about 12°F. Over most of the temperature range examined, the data scatter, while greater than observed with the smooth surface, was still not unreasonable. Most variation occurred in the limited region between 1300 and 1450°F; and, while it is possible to relate these deviations to the boiling modes discussed above in reference to the temperature trace of Fig. 2.12, no consistent explanation for this anomalous behavior near the atmospheric boiling point is immediately available. Thus, the uppermost values in this band derive from the thermal spikes, the intermediate data points correspond to the lower amplitude peaks, and the main body of data, to the periods of low-amplitude fluctuation. The lowest superheat levels relate to those times during which the wall temperature remained constant. It is speculated that during these periods an annular flow, with vaporization rather than boiling, existed. This condition was observed over the full range of saturation temperatures and yielded "superheats" from 80°F at 930°F to 9°F at 1540°F. At the highest flux levels (above 33,700 Btu/hr·ft), the large amplitude thermal spikes were not present, suggesting that the porous surface may become increasingly effective with increasing heat flux.

The results for the test section having eight drilled holes are indicated by the inverted triangles in Fig. 2.15. The measured superheats fall consistently below those obtained with the porous surface, ranging from 83°F at a saturation temperature of 900°F to as low as 7°F at 1350°F. Two features may be distinguished in these data: (1) an apparent separation into two sets with the lower values again possibly relating to an annular flow, and (2) a leveling-off in the superheat at saturation temperatures above 1250°F. This latter characteristic is unanticipated; and, while this may merely indicate some limit in the sensitivity of the detection instrumentation, the fact that the two sets of data asymptote at different superheat values suggests that a more fundamental factor may be involved.

2.2. Boiling in Multirod Geometries

L. G. Alexander

Preliminary experiments with the previously described[8] seven-rod water boiler were completed; typical data for the critical heat flux as a function of the exit quality at a 1/16-in. rod separation are shown in Fig. 2.16. With all of the rods at the same heat flux, "burnout" occurred first on the central rod except possibly in the chug-flow regime. This result is contrary to expectations based on experiments at high pressure. However, many of the high-pressure experiments were conducted in test channels having spacers in or near the heated elements; in the present apparatus there are no spacers in the flow region.

The data appear to be reproducible during any one day of operation, but there was a gradual shift of the critical heat flux to higher values over a period of several days; this was attributed to the presence of a scale of unestablished origin which deposited on the heating surfaces. Demineralized water was used in these experiments; and the circulating stream was in contact only with the materials of construction of the apparatus — glass, stainless steel, Teflon, Inconel, and brass plus small amounts of silver and soft solders. The heated bundles consisted of Firerods sheathed in Inconel for the test cluster and of stainless steel clad Calrods for the preheater. In the course of these experiments, one of the preheater rods ruptured discharging magnesium oxide into the system; the surface contamination on the test rods may derive from this source.

The preheater is being rebuilt using Firerods both to increase the reliability of the apparatus and to extend the range of the variables being studied. At present, an exit quality of 50% is possible only at mass flows less than 20,000 $lb/hr \cdot ft^2$; while at $G = 50,000$ $lb/hr \cdot ft^2$, the exit quality is limited to about 30%, barely in the burnout range. Increasing the preheater capacity to 30 kw will enable mass flows to range up to 100,000 $lb/hr \cdot ft^2$ at 30% quality. It will also be possible to examine the effect of inlet quality on the critical flux.

---

[8]J. L. Wantland, Water Boiling in a Multirod Geometry, pp. 27–30, "Studies in Heat Transfer and Fluid Mechanics, Progress Report for Period Jan. 1 – Sept. 30, 1963," USAEC Report ORNL-TM-915, Oak Ridge National Laboratory, October 1964.

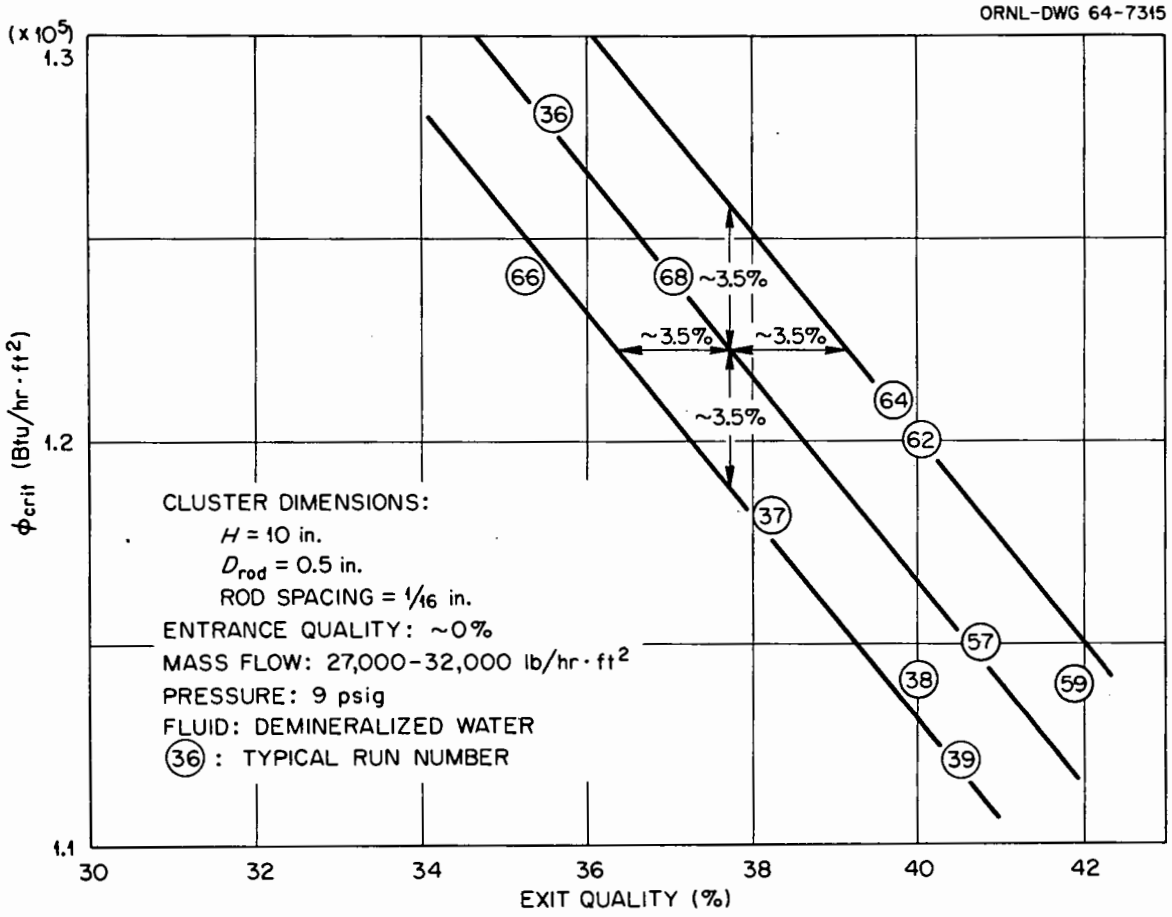

Fig. 2.16. Critical Heat Flux in a Seven-Rod Cluster.

The design of a thin-walled tube to replace the central Firerod is in progress. This tube will be heated by passing a low-voltage, high-amperage current through the wall of the tube (6 to 10 mils thick). The temperature distribution over the entire inside surface of the tube will be mapped. The frequency and magnitude of the temperature fluctuations will be determined as the heat flux is brought up to the critical level. These experiments will show where burnout is initiated in such clusters (i.e., facing an adjacent tube, or facing the gap between two adjacent tubes) and perhaps also shed some light on the nature of the instabilities that lead to burnout.

2.3. General Boiling Studies

W. R. Gambill

2.3.1. Critical Heat Flux for Natural Convection of Water in Blocked Vertical Channels

The problem of estimating the maximum allowable heat-generation rate in a vertically oriented, natural-circulation cooled reactor core with one of more flow channels inadvertently blocked at the base has sometimes arisen during hazards analyses. Very few experimental data pertinent to this poor heat-transfer situation are available, and no predictive techniques have been proposed.

To remedy this situation, two correlations of the minimum critical heat flux have been developed utilizing information available in the literature. The first is an empirical fit of the available data (nine tests conducted by WAPD[9] and MIT[10]), according to which the critical flux (Btu/hr·ft^2) is given as:

$$(\phi_c)_{min.} = 2.00 \times 10^6 \frac{D_e^2 P^{1/6}}{L_h^{0.8}} , \qquad (2.4)$$

[9]M. Troy, "Zero Net Flow Burnout Tests at 2000 Psia," USAEC Report WAPD-TH-251, Westinghouse Electric Corp., Atomic Power Division, Pittsburgh, Penna., 1596; also USAEC Report WAPD-TH-304, 1957.

[10]P. Griffith, W. A. Schumann, and A. D. Neustal, "Flooding and Burn-Out in Closed-End Vertical Tubes," Paper No. 5, Symposium on Two-Phase Fluid Flow, Institution of Mechanical Engineers, London, Feb. 7, 1962.

where D_e is the equivalent diameter of the channel (in.); L_h, the heated length of the channel (in.); and P, the pressure level (psia). The second correlation is an adaptation of Wallis' correlation[11] of adiabatic flooding rates for unheated vertical tubes to include heat addition; this results in the dimensionless expression:

$$\frac{\phi_c \, L_h}{\lambda \, D_e^{3/2} \, (\rho_v \, g \, \Delta\rho)^{1/2}} = \frac{1}{8} \, , \tag{2.5}$$

where λ is the latent heat of vaporization; ρ_v, the vapor density; $\Delta\rho$, the liquid-vapor density difference; and g, the local acceleration of gravity. Because of its greater generality, Eq. (2.5) was tentatively recommended for the prediction of critical heat fluxes for this case.

Subsequent to the statement of Eqs. (2.4) and (2.5), an experimental program of limited extent was initiated as a check on the validity of these predictions. Data were obtained with tubes of 0.087- to 0.246-in. inside diameter and 6 to 48 in. heated length operated in a liquid pool at atmospheric pressure. The new data, for tubes with an inside diameter greater than 0.1 in., and the older WAPD and MIT data are plotted in accord with Eq. (2.5) in Fig. 2.17. The minimum line above which the new tests fall yields values of ϕ_c larger by a factor of 2.2 than does Eq. (2.5). The critical fluxes for tubes with an inside diameter less than 0.1 in. fall below Eq. (2.5), apparently because of the influence of surface tension; further tests are being conducted with the smallest test sections.

The subcooling of the liquid pool above the heated channels was also varied in these tests, and the vertical dispersion of points at a given value of the abscissa in Fig. 2.17 reflects the influence of the subcooling on the critical flux.

---

[11]G. B. Wallis, "The Transition from Flooding to Cocurrent Annular Flow in a Vertical Pipe," British Atomic Energy Authority Report AEEW-R 142, 1962.

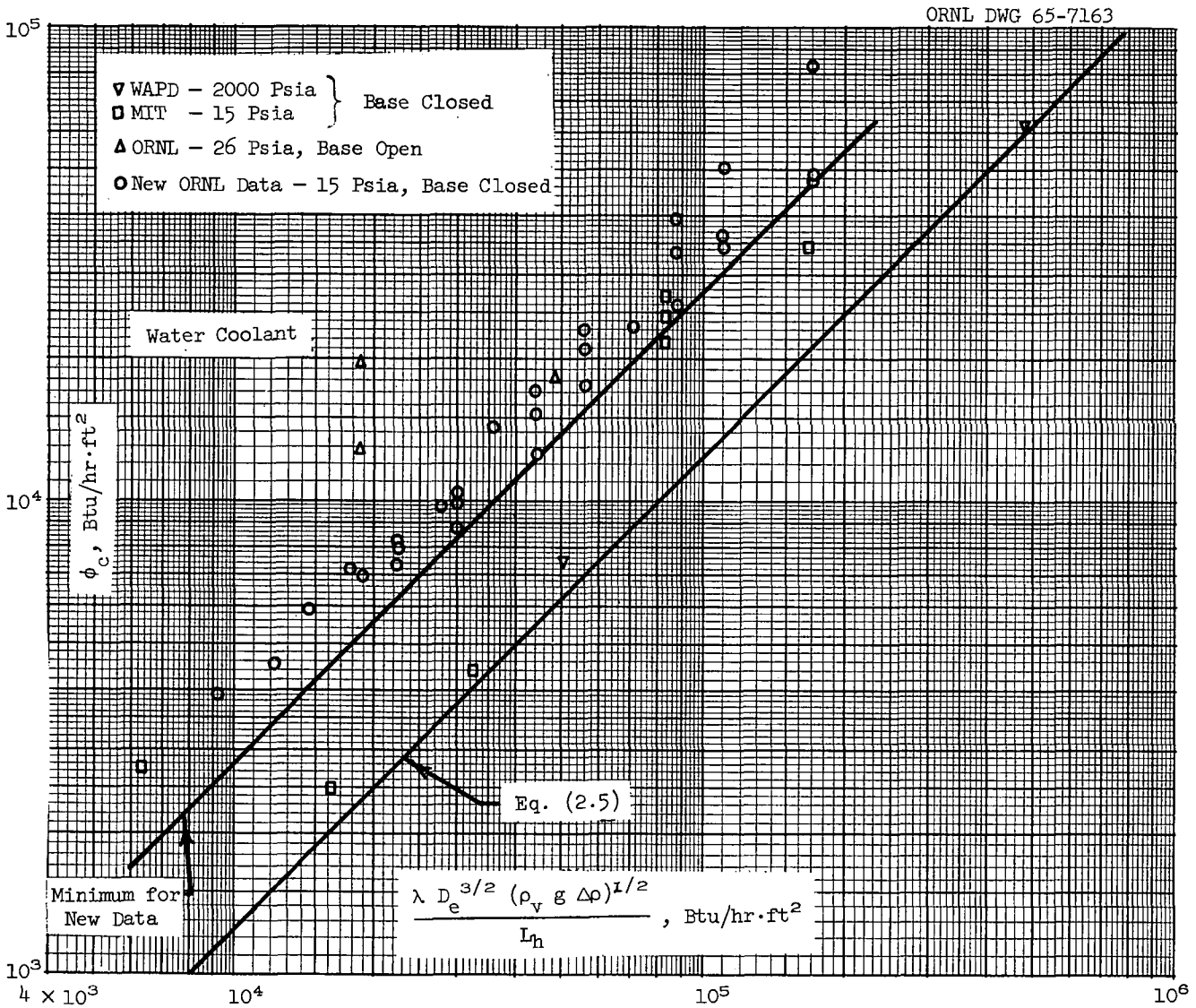

Fig. 2.17. Natural-Convection Burnout of Blocked Vertical Channels.

2.4. Swirl-Flow Heat Transfer

W. R. Gambill

2.4.1. Swirl-Flow Forced-Convection Bulk-Boiling Burnout

The heat-transfer and pressure-drop characteristics of water[12] and ethylene glycol[13] in subcooled boiling within a circular tube containing a full-length twisted tape to generate a swirl motion have been intensively studied over the past few years. This current study is intended to extend these investigations to the region of net boiling; initial emphasis is on the definition of burnout limits.

The experimental system, shown schematically in Fig. 2.18, is of open-circuit design in the sense that the test fluid (demineralized water) is pumped from a large storage vessel and, after passing through the boiler section, the separated liquid and condensed vapor streams are returned to this same vessel at a point above the free liquid surface. The liquid leaving the pump passes through a preheater into the test section; a large pressure drop, taken across a valve immediately upstream of the test boiler, serves to stabilize the flow. The water-steam mixture leaving the test section is separated in a steam separator; and the individual streams, the vapor after condensation, are returned by gravity feed through a cooler to the storage tank. The flow in all fluid streams is monitored by turbine-type meters and/or rotameters. A photograph of a front view of the system is shown as Fig. 2.19.

It is currently planned to investigate vertical upflow for exit pressures to 45 psia with inlet liquid velocities ranging from 1 to 6 ft/sec, inlet subcoolings from 0 to 30°F, and tape twist ratios from 2.5 to 8 inside diameters per 180-deg twist. Axial-flow critical-flux data will also be obtained using tubes without inserts so as to provide comparison with

---

[12]W. R. Gambill, R. D. Bundy, and R. W. Wansbrough, "Heat Transfer, Burnout, and Pressure Drop for Water in Swirl Flow Through Tubes with Internal Twisted Tapes," Chemical Engineering Progress Symposium Series, 57(32): 127–137 (1961); see also USAEC Report ORNL-2911, Oak Ridge National Laboratory, 1960.

[13]W. R. Gambill and R. D. Bundy, "High-Flux Heat-Transfer Characteristics of Pure Ethylene Glycol in Axial and Swirl Flow," A.I.Ch.E. Journal, 9(1): 55–59 (1963); see also USAEC Report ORNL-TM-915, pp. 35–40, Oak Ridge National Laboratory, October 1964.

ORNL DWG. 64-3407

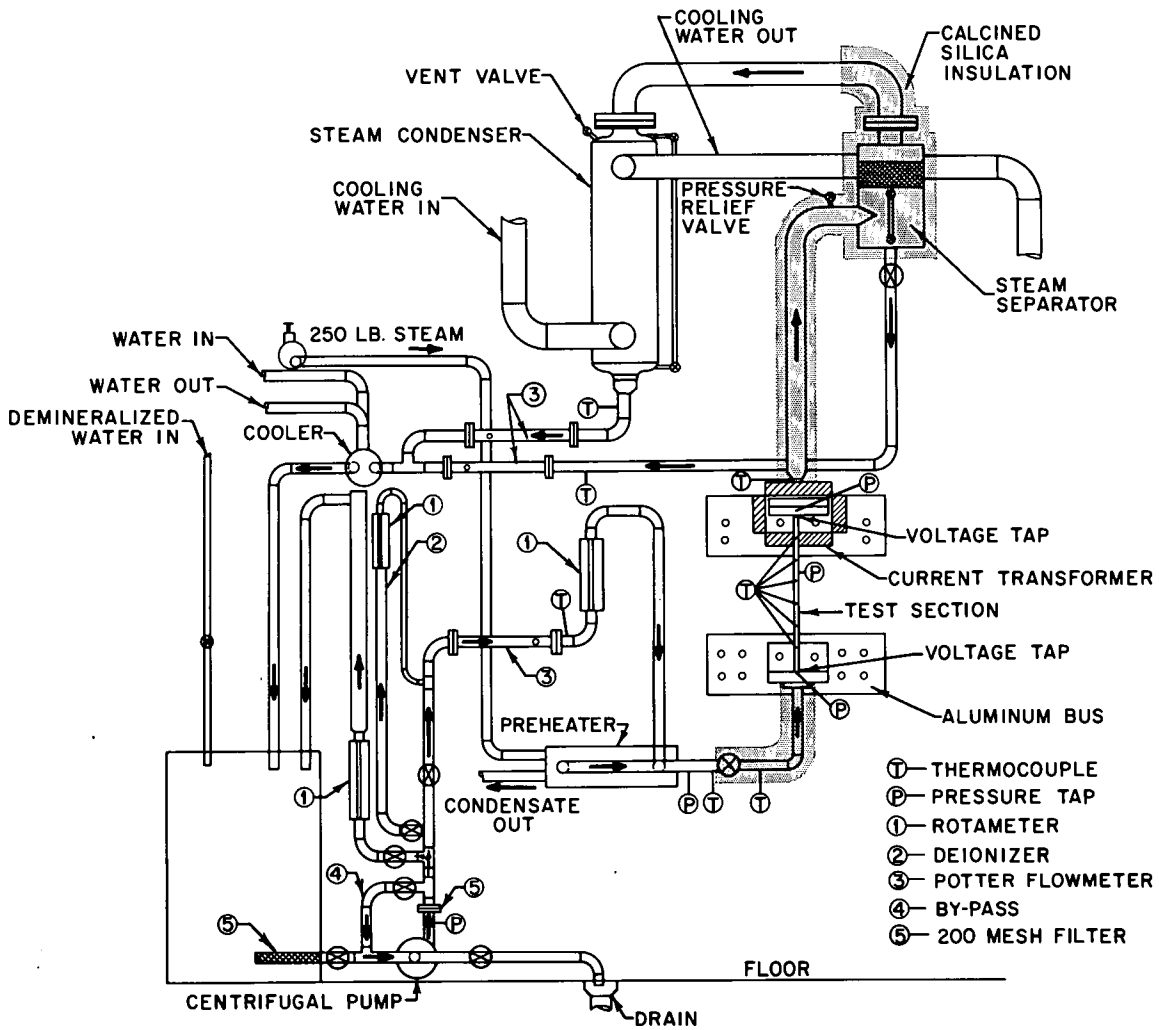

Fig. 2.18. Schematic and Flow Diagram of Experimental Loop for Study of Swirl-Flow with Net Vapor Generation.

PHOTO 70943

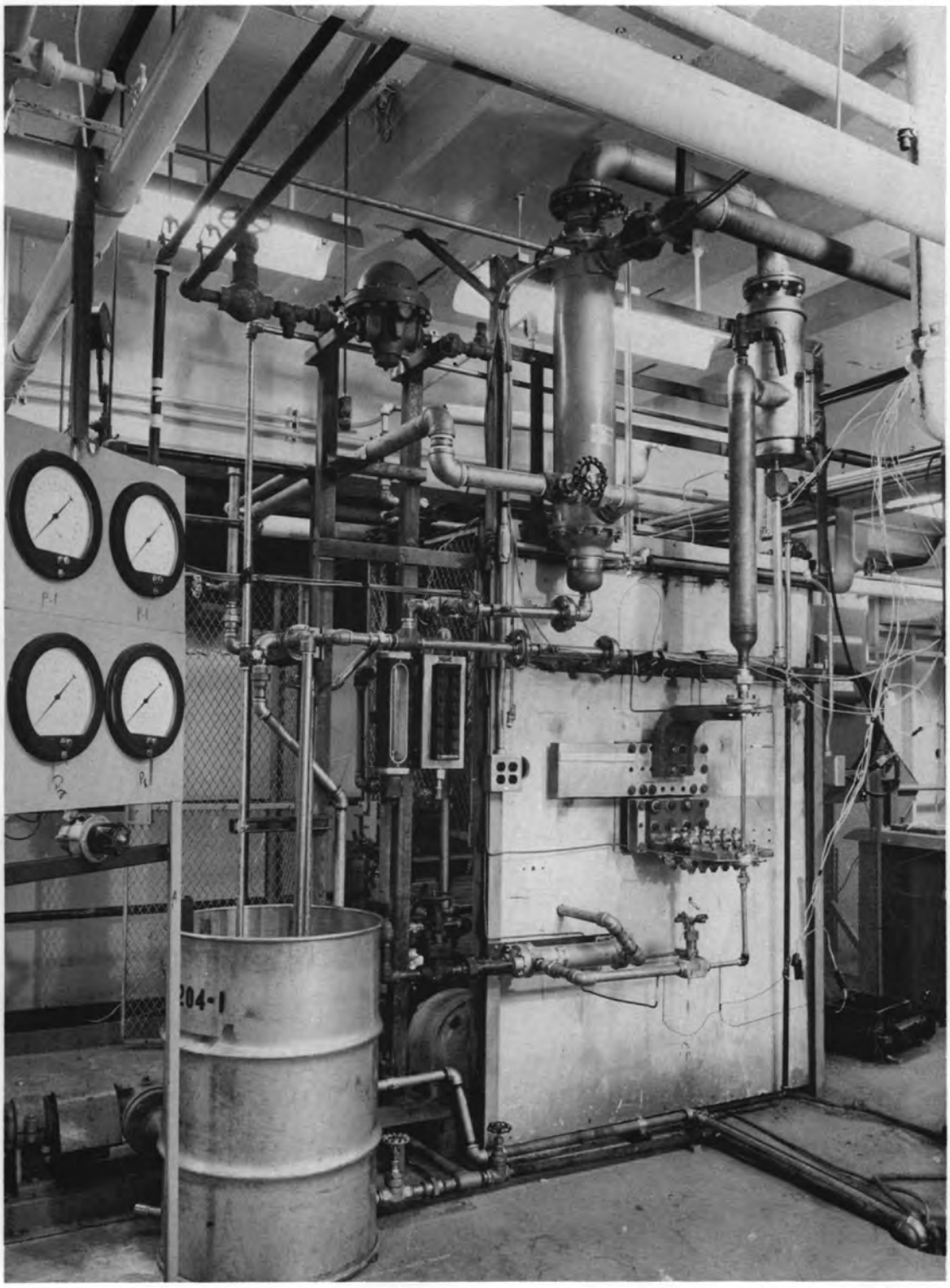

Fig. 2.19. View of Partially Assembled System for Swirl-Flow Studies with Net Vapor Generation.

the swirl flow data.

The heat-flux capability of the system with 18-in.-long A-nickel tubular test sections is $\sim 2.5 \times 10^6$ Btu/hr·ft^2. In the tubes fitted with twisted tapes, 98.8% of the total heat generation will take place in the tube wall. At $\phi = 10^6$ Btu/hr·ft^2, the temperature difference across the tube wall is ~85°F; and the adiabatic rise rate of the tube-wall temperature, ~840°F/sec. The turbine-type flowmeters have a calibrated reproducibility of ±1/2% maximum deviation. A complete series of energy balances converged within 5.6%. At pressures of 30 to 50 psia and qualities of 50 to 90 wt %, the critical flow limit is estimated to correspond to a mass velocity of ~200 lb/sec·ft^2 (inlet liquid velocity of 3.3 fps). Dry-tube, zero-flow heat-loss tests gave a maximum heat loss, at a mean external wall temperature of 300°C, of 93 watts.

An external view of the first test section during an early stage of assembly is shown in Fig. 2.20; pressure taps may be seen at the entrance, at 3/4 the heated length, and at the exit. Fig. 2.21 shows the same test section after the installation of thermocouples, a current transformer, thermal insulation, and a shroud tube concentric with the test section. On the interior surface of the nonconducting Lavite shroud tube are mounted 32 subminiature solid-state light-activated switches which will act as the sensing elements of the burnout protection system. These switches, which are of the silicon PNPN type, are normally open, but switch into conduction in ~2 μsec when the effective local irradiance rises to ~3 mw/cm^2. The switches are wired in parallel, and the closing of any one activates a relay and circuit breaker to interrupt the test-section heating current. At the same time, an external light indicates which of the switches has been activated. The total response time for the entire circuit is ~80 msec.

Two variations of the light-activated switch are pictured in Fig. 2.22; at the top is the new GE L9 unit and below is the GE subminiature L7 type (now superseded by the L9 but being used in the subject system). A brief study was made of the sensitivity of each type of switch by experimentally determining the variation of cut-on distance (x_c) with source temperature (t_s). The tests were conducted by traversing a switch mounted on a rack-and-pinion train which was free to move normal to an electrically heated

PHOTO 70945

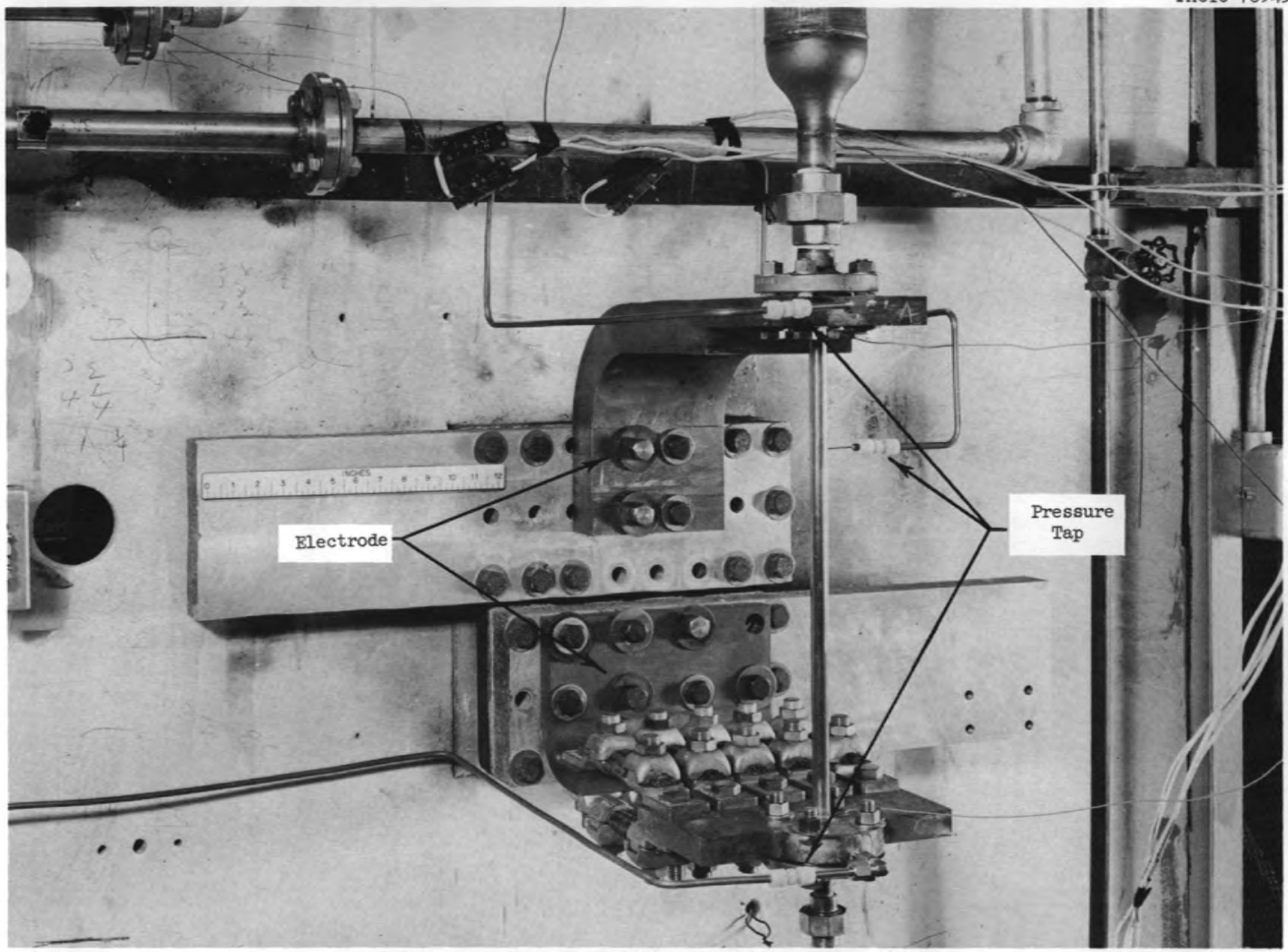

Fig. 2.20. Close-up of Swirl-Flow Test Section.

PHOTO 71031

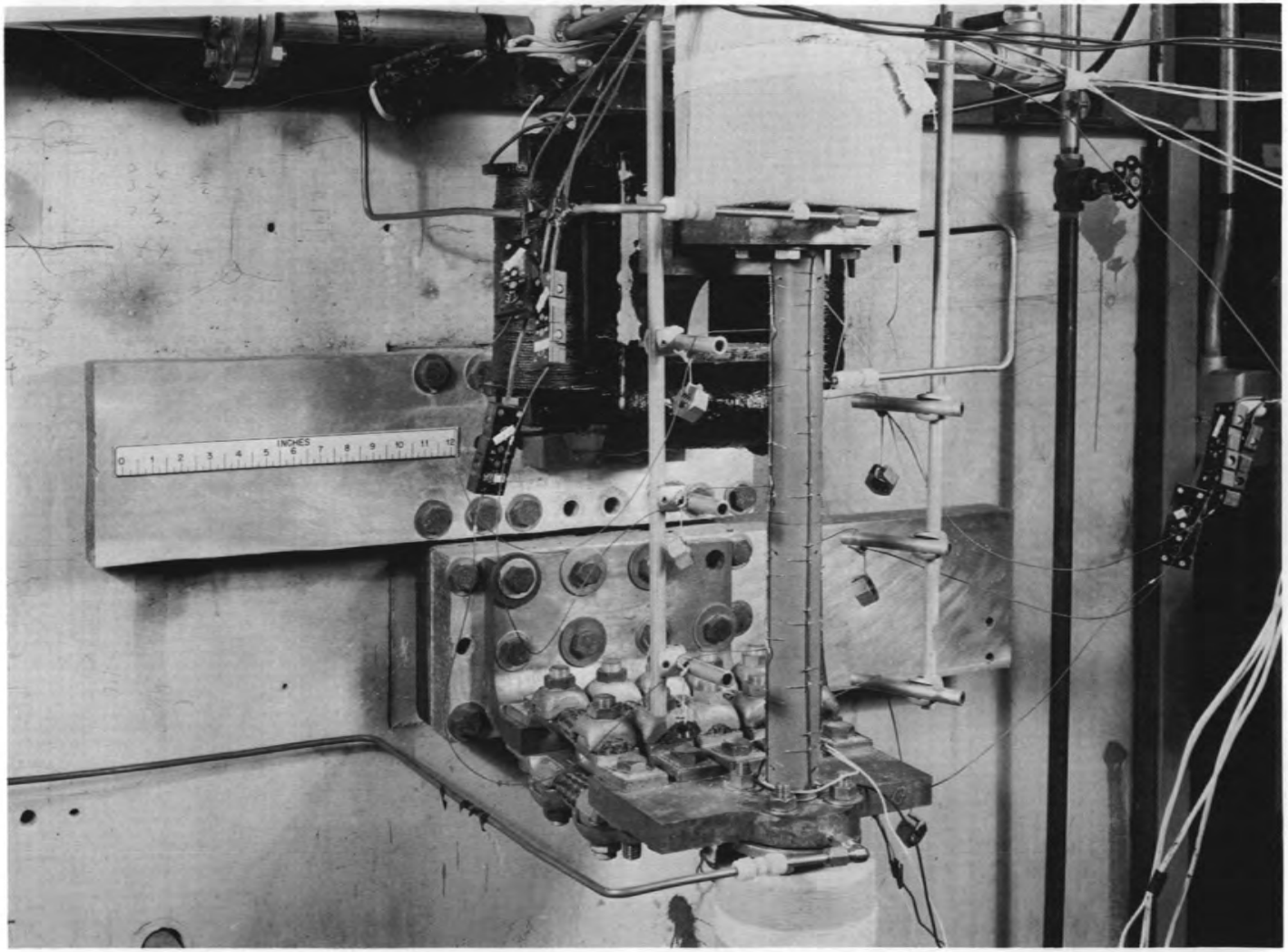

Fig. 2.21. Swirl-Flow Test Section with Shroud Installed.

PHOTO 71079

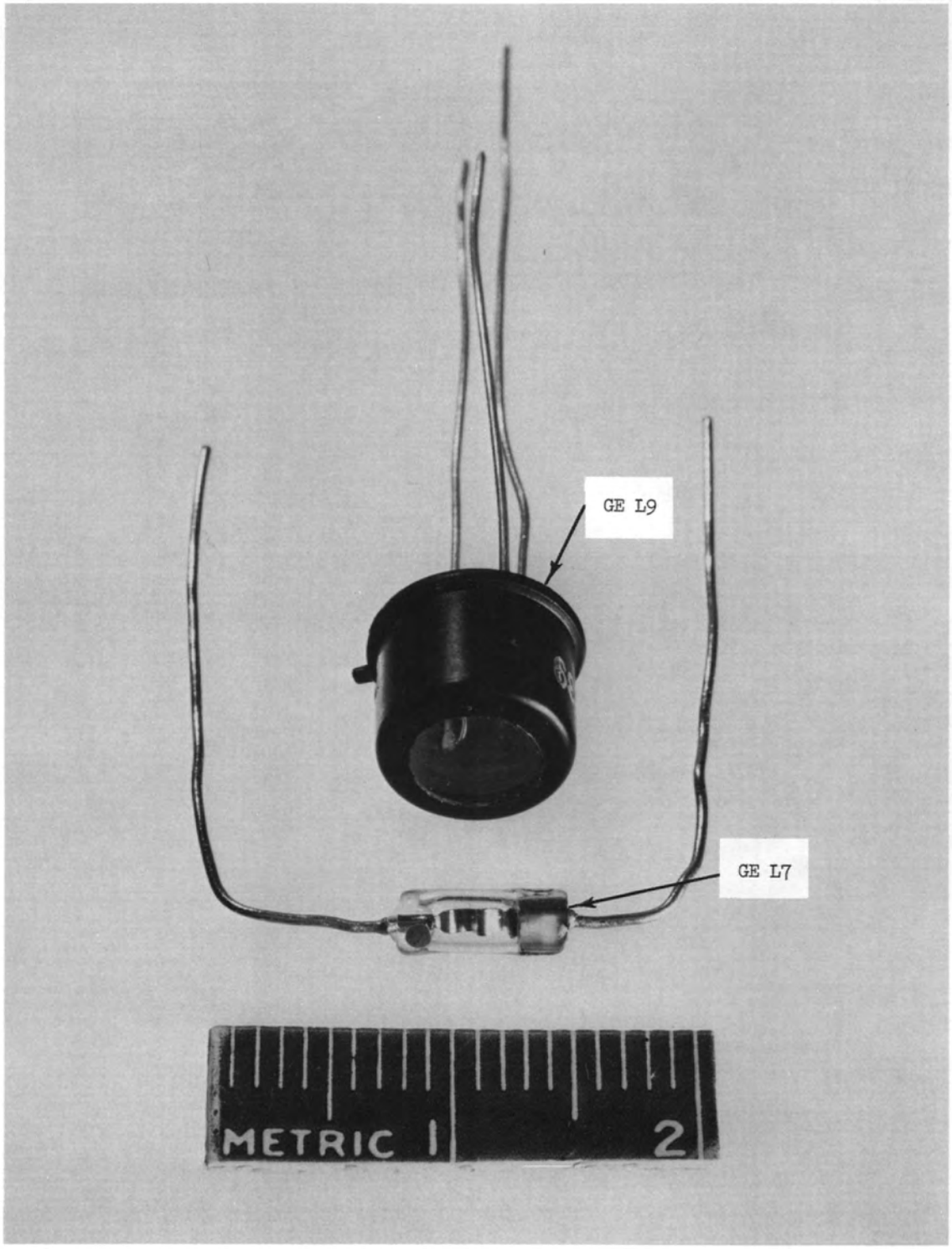

Fig. 2.22. Light-Activated Switches.

Nichrome strip mounted at the base of a Mycalex (synthetic mica) chimney. The results shown in Fig. 2.23 are typical of those obtained. The sensitivity sharply increases when source temperatures of 1100 to 1200°F are reached. Further tests were made to determine the influence of ambient temperature on switch performance; and it was found that under the anticipated operating conditions, no effect was measurable.

2.4.2. Subcooled Swirl-Flow Boiling and Burnout with Heated Twisted Tapes and Zero Wall Flux

Twenty-one series of swirl-flow tests were conducted in which all of the heat was generated in twisted-tape swirl generators. This is in contrast to past ORNL swirl-flow tests with twisted tapes,[12,13] in which ~99% of the heat was generated in the metallic tube wall. In the current study,[14] water from a constant-head tank flowed by gravity at 5 to 8 fps through a vertical 0.27-in.-ID glass tube ~13 in. long in which was located a resistance-heated, 16-mil-thick A-nickel tape. A schematic of the experimental system is shown in Fig. 2.24; and a view of a typical test section (unheated, water flowing) is shown as Fig. 2.25.

Tape twist ratios were varied from 2.7 to ∞ inside tube diameters per 180-deg twist, inlet water temperatures from 63 to 173°F, and heat fluxes from 0.21×10^6 to 1.20×10^6 Btu/hr·ft^2. The water head above the top of the tube was held at 30.7 in.

In Fig. 2.26, the mean tape-surface temperature is plotted versus the impressed heat flux with tape-twist ratio, y, as a parameter for an inlet water temperature of 64°F. Each boiling curve shown terminates at the burnout point. Similar results were obtained for the other inlet water temperatures. The burnout data alone are summarized in Table 2.3.

In Fig. 2.27, the ratio of the twisted-tape wall superheat at burnout to the average straight-tape critical wall superheat is plotted versus the tape-twist ratio for each inlet water temperature. The critical superheat

---

[14]W. R. Gambill, "Subcooled Swirl-Flow Boiling and Burnout with Electrically Heated Twisted Tapes and Zero Wall Flux," USAEC Report ORNL-TM-894, Oak Ridge National Laboratory, June 11, 1964.

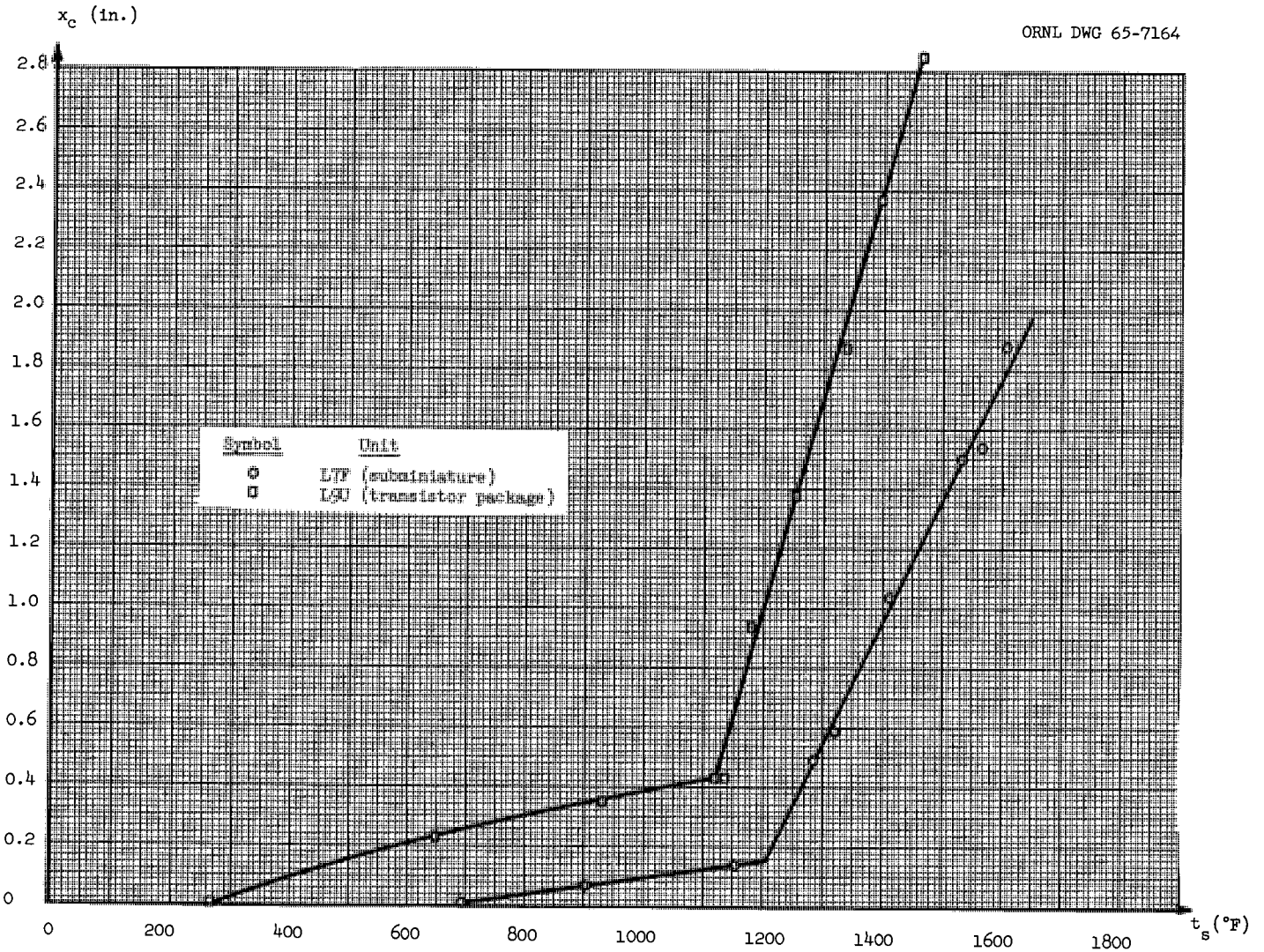

Fig. 2.23. Cut-on Distance Versus Source Temperature for GE Light-Activated Switches.

ORNL DWG. 64-1753K

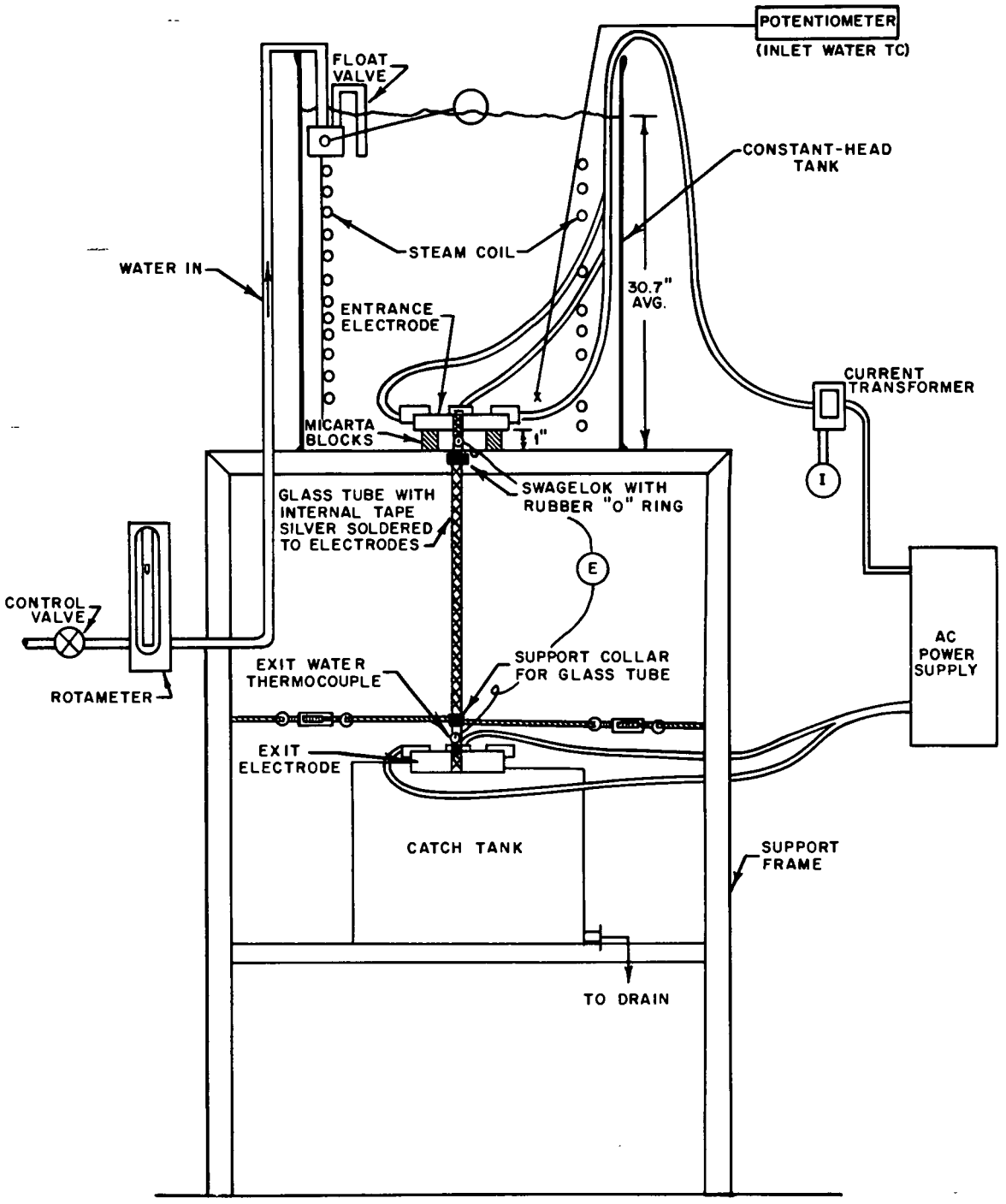

Fig. 2.24. Schematic of Apparatus for Study of Heat Transfer from a Heated Twisted Tape Within an Adiabatic, Circular Channel.

PHOTO 64495

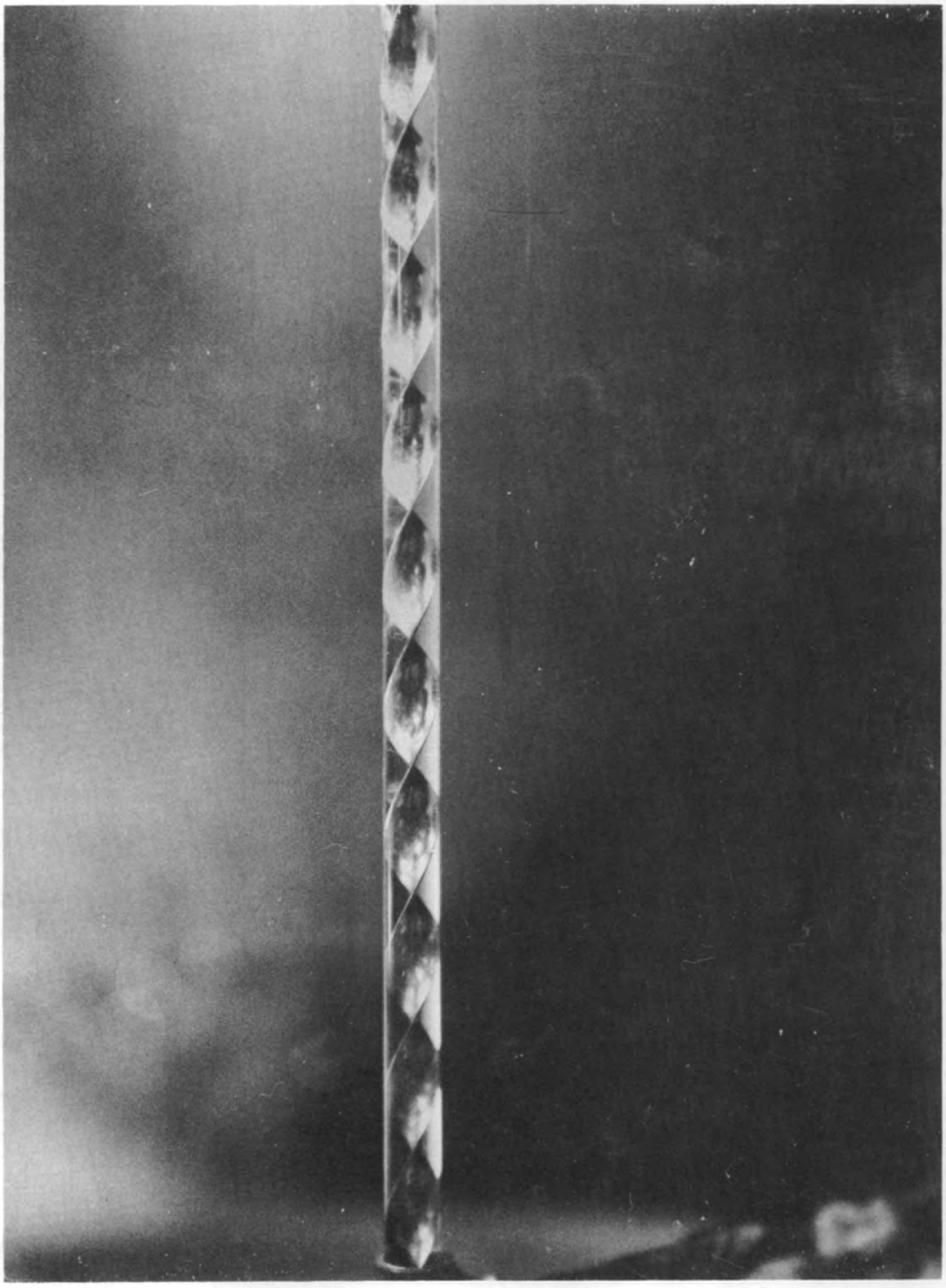

Fig. 2.25. View of Typical Test Section, Water Flowing, Zero Heat Flux.

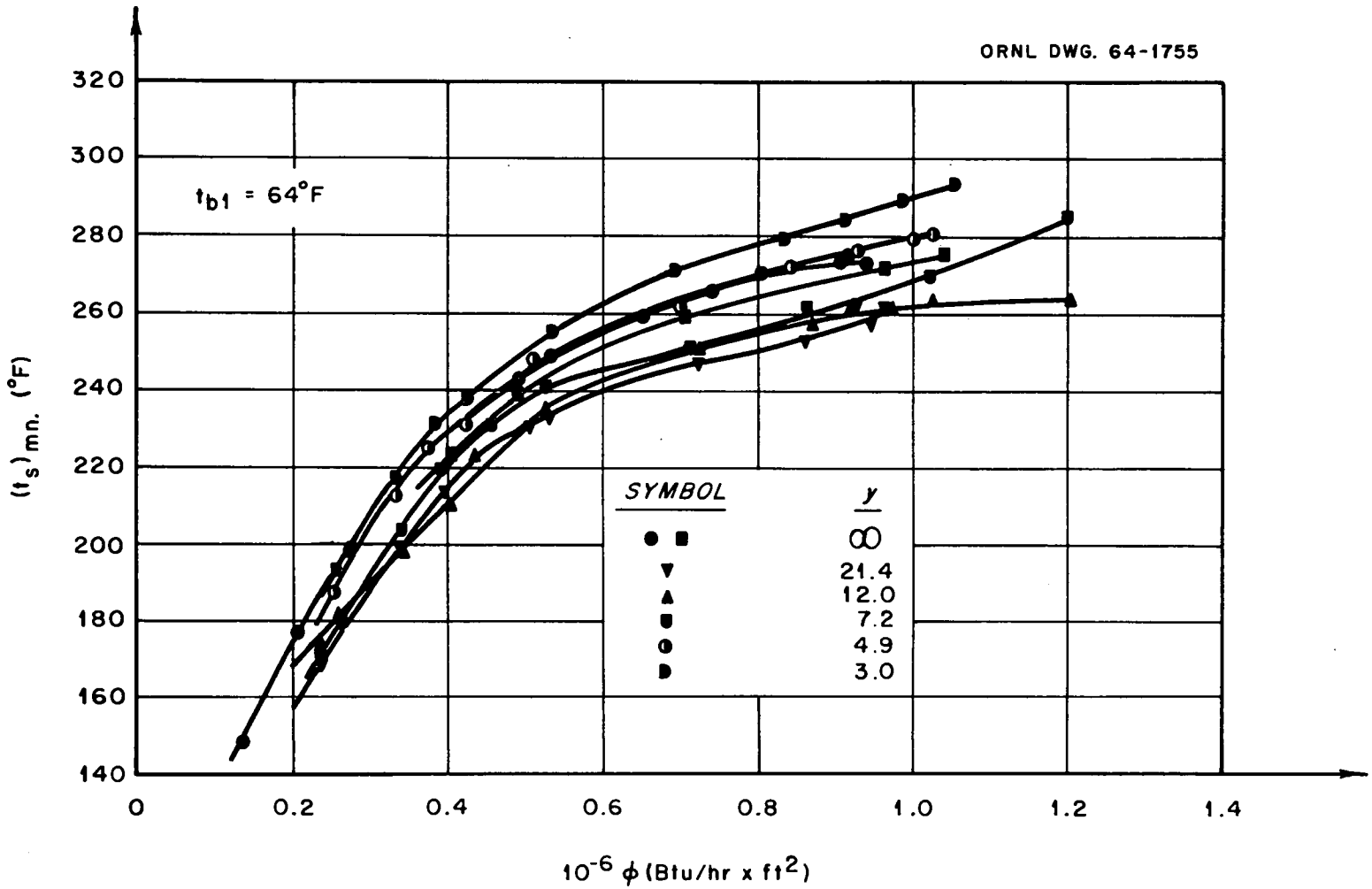

Fig. 2.26. Variation of Mean-Tube-Surface Temperature with Heat Flux for Heated Tapes of Several Twist Ratios. Each curve terminates at the burnout point.

Table 2.3. Heated-Tape Critical-Flux Data

Test No.	y[a]	t_{b_1}, °F	Δt_{sub},[b] °F exit	Δt_{sub},[b] °F bo site	$(V_a)_{bo}$,[c] fps	$(\Delta t_{sat})_{bo,mn}$, °F	ϕ_{bo},[e] 10^6 Btu/hr·ft^2
1–12	∞	64.4 ± 1.4	41.0	47.0	6.4	61.6	0.942
7–5	∞		44.3	44.3	6.8	63.6	1.041
2–9	21.4		25.1	44.0	5.7	50.9	0.967
4–12	12.0		60.9	63.0	6.7	51.8	1.204
3–11	7.2		67.4	67.4	6.7	73.9	1.200
6–10	4.9		39.1	39.1	5.6	69.8	1.028
5–10	3.0		46.8	48.3	5.6	82.6	1.058
8–6	∞	121.0 ± 3.6	51.3	51.3	7.8	63.0	0.661
19–7	∞		17.0	17.0	7.5	35.6	0.708
11–5	11.2		46.5	50.2	7.1	50.0	0.700
12–6	7.0		42.1	46.6	7.4	51.1	0.730
13–4	4.7		39.5	39.5	7.2	59.6	0.735
14–3	2.7		31.0	31.0	6.2	76.2	0.677
15–9	∞	170.4 ± 1.0	17.1	28.9	7.5	53.4	0.352
20–4	∞		18.8	29.4	7.7	32.0	0.328
17–5	9.7		16.0	24.3	7.6	40.7	0.347
21–5	6.3		13.3	13.3	7.3	35.5	0.354
18–4	2.9		6.3	23.0	4.7	62.1	0.315
16–2	2.7		0.91 Wt % Quality		3.3[d]	72.2	0.320

[a]Tape twist ratio, units of inside tube diameters per 180-deg twist.

[b]Mean t_{sat} at exit = 210.8°F (±0.35°F).

[c]Three auxiliary adiabatic tests gave a flow rate through the empty tube 1.30 times that through the tube with a flat tape ($y = \infty$).

[d]Lowest velocity measured in any test; flow rate decreased significantly just before burnout.

[e]The heat-balance convergence was usually within 12% (16% maximum).

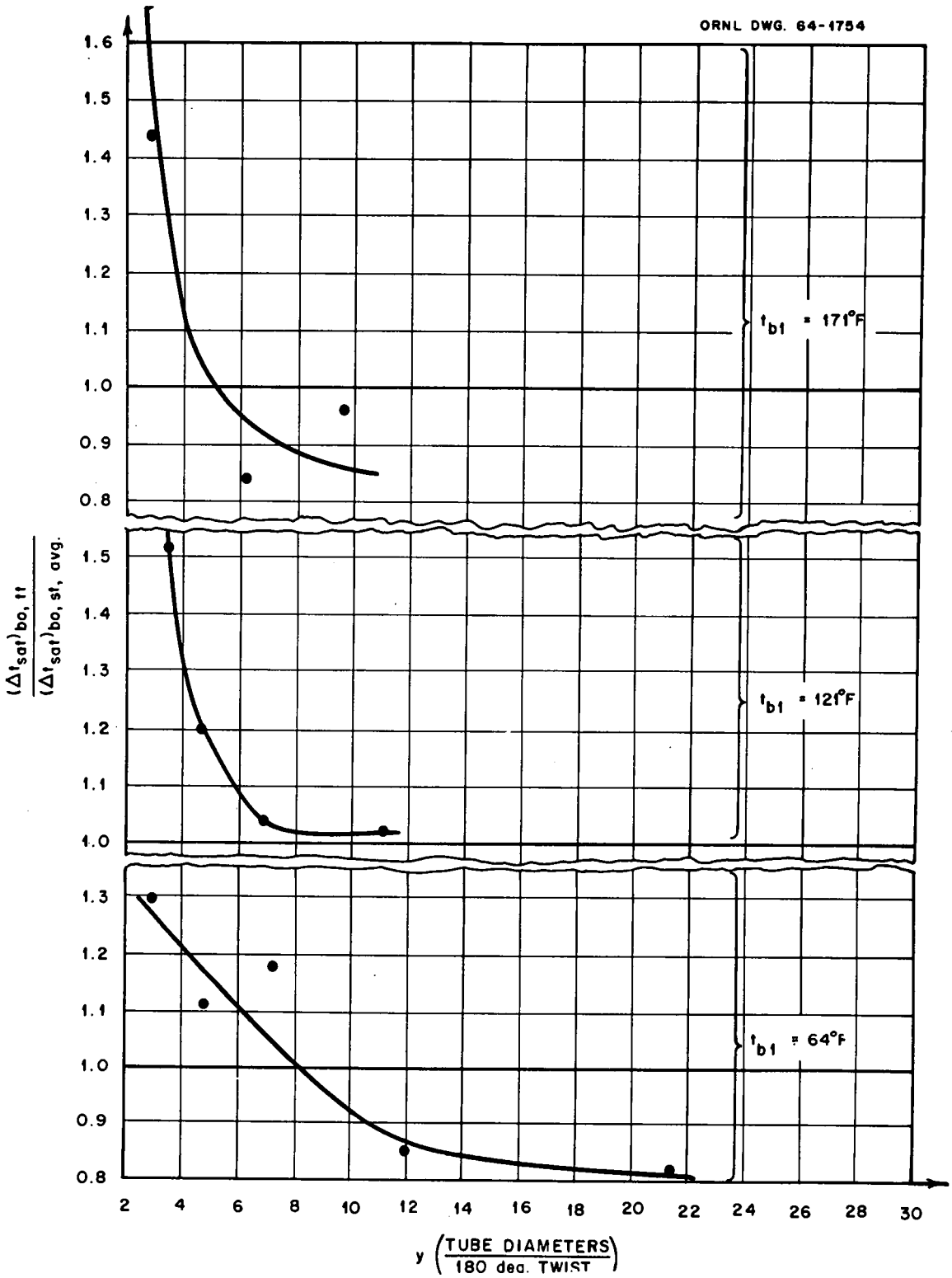

Fig. 2.27. Variation of the Superheat at Burnout with Tape-Twist Ratio at Several Inlet Water Temperatures. Data are normalized with respect to the average critical wall superheat for straight tapes.

increases continuously with decrease of the numerical tape-twist ratio, and the increment is smallest at the lowest inlet temperature. Similarly, in Fig. 2.28, the ratio of the twisted-tape burnout heat flux to the average straight-tape burnout flux is shown as a function of the tape-twist ratio for each inlet water temperature. With the subject geometry, the swirl does not appear to have a marked influence on the burnout flux. The maximum enhancement of the ϕ_{bo} (~20%), which occurs at y = 7 to 10, is largest at the lowest inlet temperature. Comparisons were made between the experimental burnout data and the representative burnout correlations of Gunther[15] and of Ivashkevich,[16] which gave average deviations of 31.3% and 28.0%, respectively.

It was originally felt that a considerable decrease in the critical heat flux might result from heating the surface toward which vapor bubbles are transported by the acceleration field produced by the curvilinear flow pattern, and it is postulated that such decrements were not observed with swirl flow because of the secondary circulation of the main flow itself in the plane normal to the tube wall (as measured for single-phase water flow by Smithberg and Landis[17]). In the entrance region where swirl flow is established, a probable further factor in vapor removal is inertial impingement of the liquid onto the tape surface, which is inclined to the axial flow direction when the tape is twisted.

On a basis of constant heat loss, it is concluded that with the heated-tape configuration little or no burnout penalty is associated with swirl flow for $y \geq 3$ and that the burnout heat flux for heated twisted tapes can be approximated by flat-surface predictions. The results also indicate that a considerable increase in the burnout power density of tubular-core reactors can be realized by the use of internal swirl flow

---

[15]F. C. Gunther, "Photographic Study of Surface-Boiling Heat Transfer to Water with Forced Convection," Trans. Am. Soc. Mech. Engrs., 73: 115–123 (February 1951).

[16]A. A. Ivashkevich, "Critical Heat Flows in the Forced Flow of Liquids in Channels," Soviet J. of Atomic Energy, 8(1): 44–47 (1961).

[17]E. Smithberg and F. Landis, "Friction and Forced Convection Heat-Transfer Characteristics in Tubes with Twisted Tape Swirl Generators," ASME J. Heat Transfer, 39–49 (February 1964).

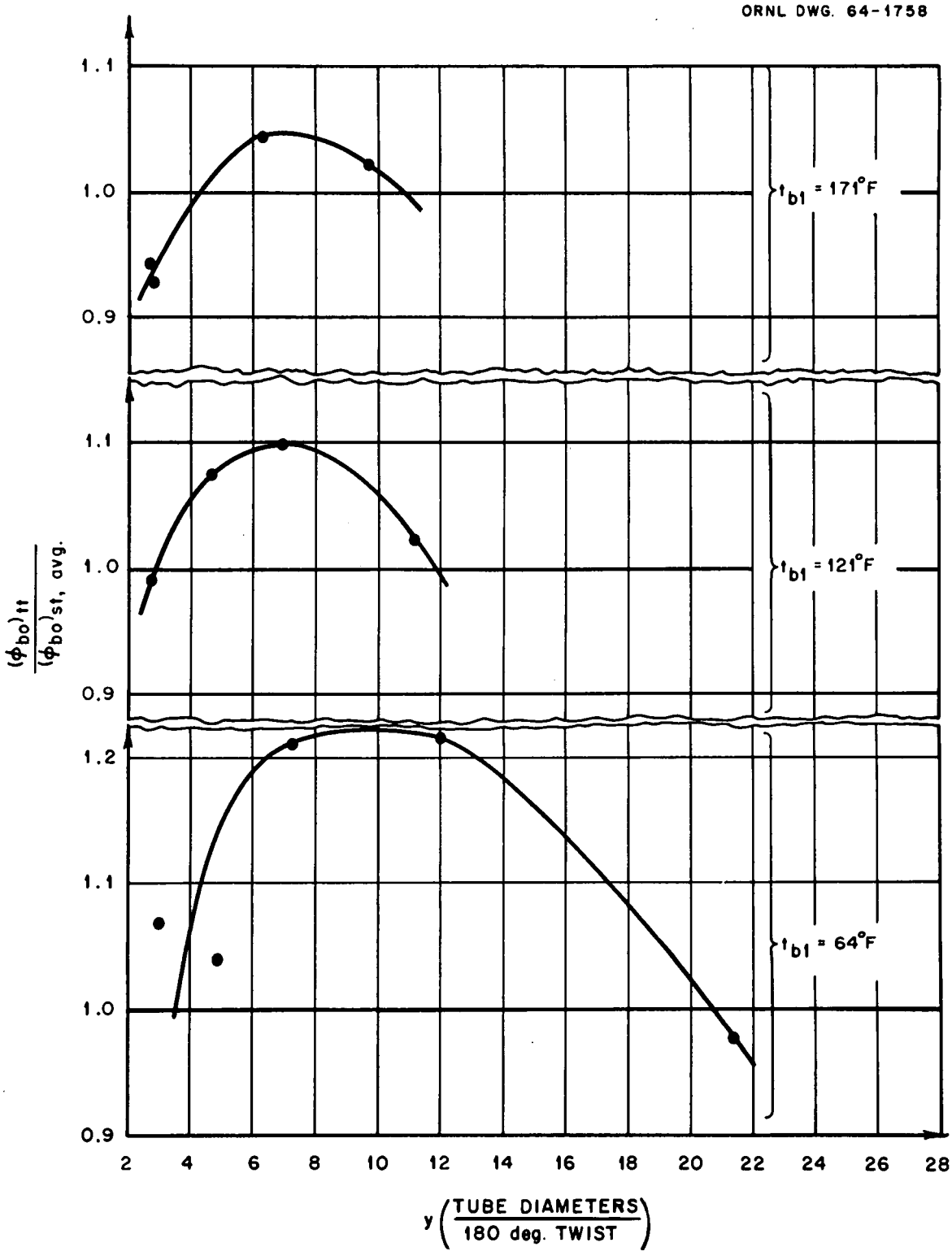

Fig. 2.28. Variation of the Burnout Heat Flux with Tape-Twist Ratio at Several Inlet Water Temperatures. Data are normalized with respect to the average burnout flux for straight tapes.

with heat generation in the twisted tape (combined, perhaps, with external axial-flow wall cooling).

2.5. Analysis of Parallel Flow in Rod Clusters

T. C. Min

As an aspect of the study into the heat-transfer and fluid-dynamic characteristics of a rod cluster of limited extent contained within a circular channel and cooled by a boiling liquid in longitudinal flow exterior to the rod surfaces,[18] an analytic description of the velocity distribution and pressure drop with annular flow in such a geometry is being attempted. The annular flow regime was chosen not only for simplicity in mathematical treatment, but also because there are strong indications that this flow pattern occurs most frequently (particularly with the alkali liquid metals) in the flow range of interest. Because of the difficulties involved in such an analysis, a number of separate problems of increasing complexity will be consecutively considered: (1) laminar, single-phase flow, (2) annular flow with a laminar liquid film, (3) annular flow with a laminar liquid film and heat transfer, (4) annular flow with a turbulent liquid film, and finally (5) annular flow with a turbulent liquid film and heat transfer. It is planned, in a later phase of this program, to assess the validity of these predictions by experimental studies which will include the measurement of the pressure drop and the film thickness in an isothermal system. The effects of heat addition will be considered in a subsequent experiment.

The geometry to be considred reduces by reason of symmetry to the cross-hatched segment shown in Fig. 2.29 for a cluster of seven rods contained within a circular shroud or in Fig. 2.30 for nineteen rods in delta array in a circular channel (one of two common arrangements). The most obvious feature in both of these figures is the complex shape of the flow channel.

---

[18]H. D. Conway, "The Bending, Buckling, and Flexural Vibration of Simply Supported Polygonal Plates by Point-Matching," J. Appl. Mech., 288–291 (June 1961).

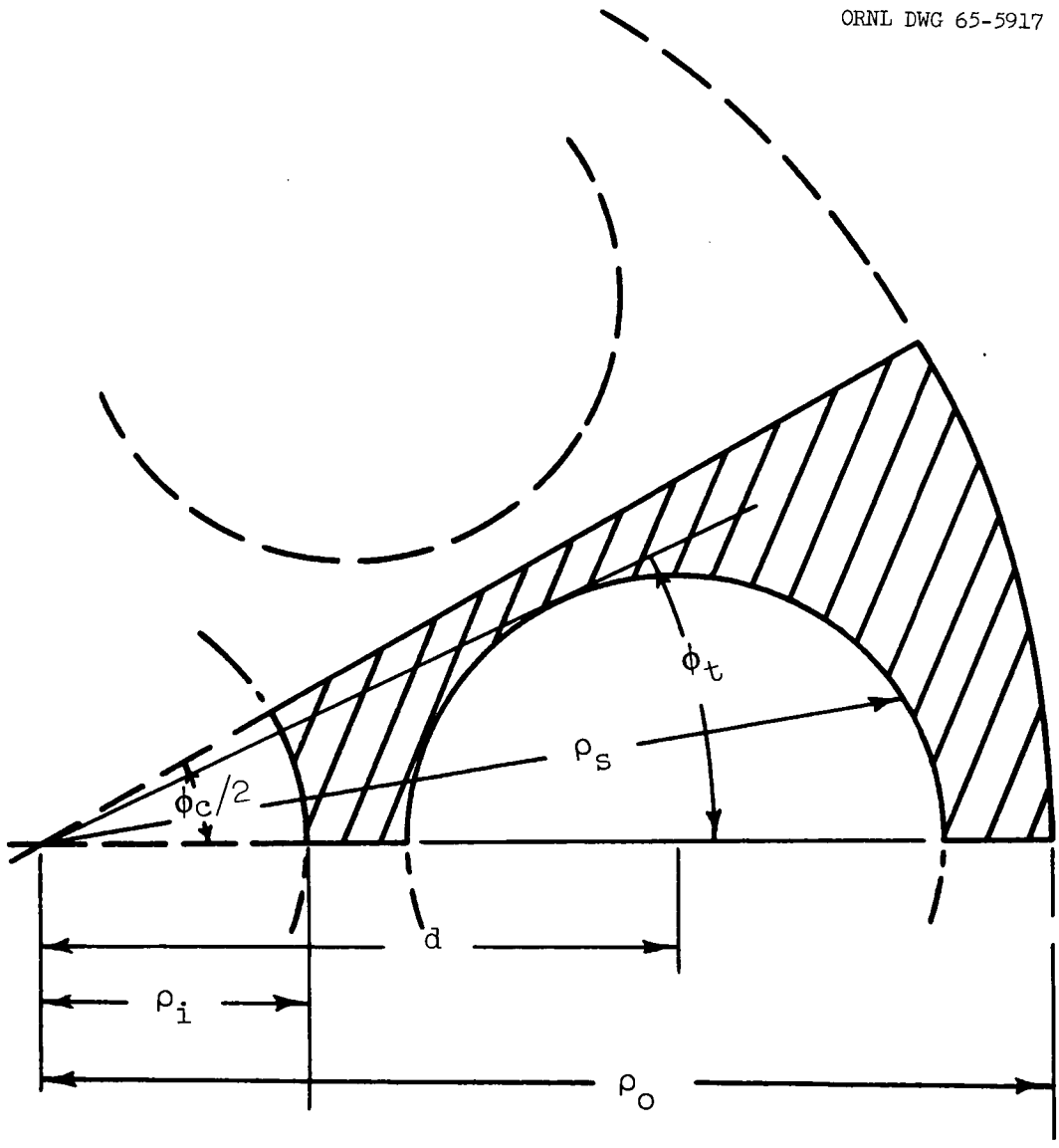

Fig. 2.29. Unit Channel Used in Analysis of Flow Through a Seven-Rod Cluster Contained Within a Circular Shroud.

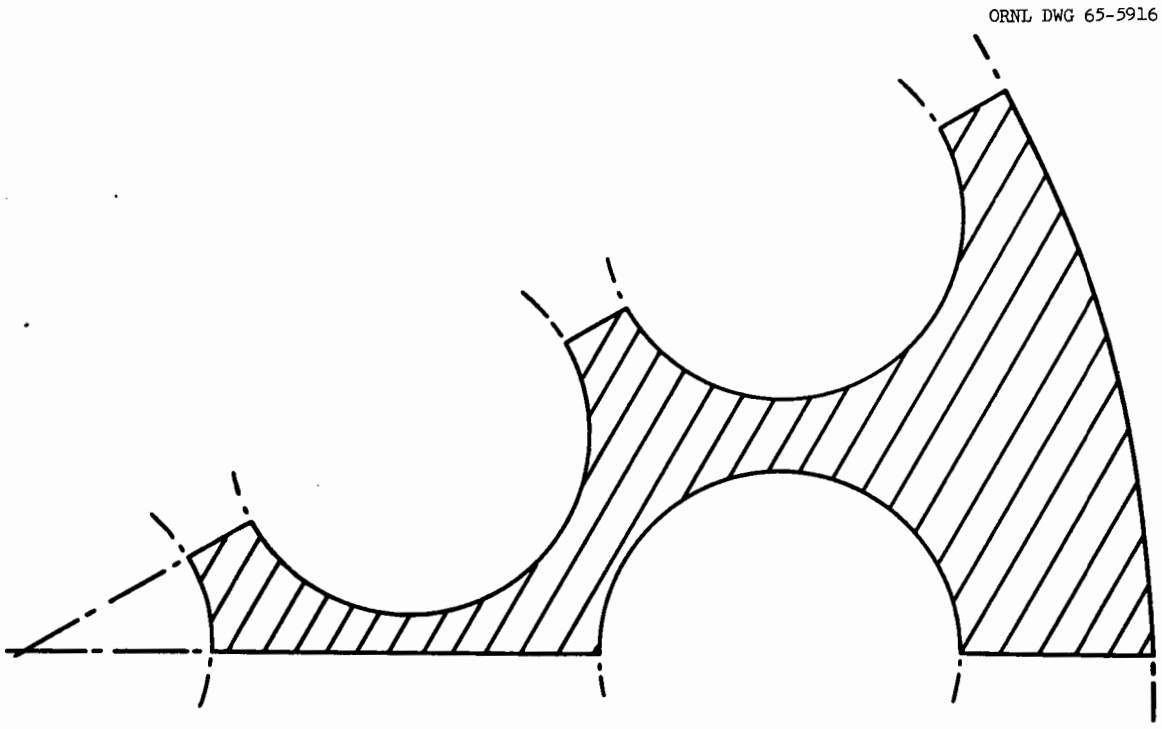

Fig. 2.30. Unit Channel in One of Two Possible Arrangements of Nineteen Rods Within a Circular Shell.

The Navier-Stokes equations for an incompressible flow with constant viscosity reduce to Poisson's equation for steady, laminar flow in a duct of constant cross section; thus,

$$\frac{\partial^2 u}{\partial \rho^2} + \frac{1}{\rho}\frac{\partial u}{\partial \rho} + \frac{1}{\rho^2}\frac{\partial^2 u}{\partial \phi^2} - c_1 = 0 \quad \text{for} \begin{cases} \rho_i \leq \rho \leq \rho_o \\ \frac{-\phi_c}{2} > \phi > \frac{\phi_c}{2} \end{cases} , \tag{2.6}$$

where $\phi_c/2$ is the angle subtended by a typical flow element; ρ_i, the radius of the central rod; and ρ_o, the radius of the outer shell. The constant, c_1, is given by

$$c_1 = \frac{g_c}{\mu}\frac{dP}{dz} + \frac{\gamma g}{\mu} , \tag{2.7}$$

in which dP/dz is the pressure gradient in the direction of flow; γ, the density; μ, the viscosity; g, the local acceleration due to gravity; and g_c, a conversion factor.

The accompanying boundary conditions are:

$$u(\rho_i, \phi) = 0 \quad \text{for} \quad \frac{-\phi_c}{2} < \phi < \frac{\phi_c}{2} ,$$

$$u(\rho_o, \phi) = 0 \quad \text{for} \quad \frac{-\phi_c}{2} < \phi < \frac{\phi_c}{2} ,$$

$$u\left(\rho_1, \frac{\phi_c}{2}\right) = u\left(\rho_i, \frac{-\phi_c}{2}\right) \text{for } \rho_i < \rho < \rho_o ,$$

$$u(\rho_s, \phi_s) = 0 \quad \text{for} \begin{cases} 0 < \phi < \phi_t \\ \rho_i < \rho_s < \rho_o \end{cases} ,$$

where

ρ_s = radial distance to the peripheral rod from the origin at the center of the central rod,

ϕ_t = angle between a tangent to the peripheral rod and $\phi = 0$.

The geometric quantities involved in this analysis are indicated for the seven-rod geometry in Fig. 2.29.

By means of the transformation,

$$u^*(\rho, \phi) = \frac{u(\rho, \phi)}{\frac{-\rho_i^2 c_1}{4}} = W(\rho, \phi) - \zeta^2 ,$$

Eq. (2.6) can be simplified to the Laplace equation; thus,

$$\frac{1}{\rho} \frac{\partial}{\partial \rho} \left(\rho \frac{\partial W}{\partial \rho} \right) + \frac{1}{\rho^2} \frac{\partial^2 W}{\partial \phi^2} = 0 . \tag{2.8}$$

The boundary conditions in turn become,

$$W(\rho_i, \phi) = 1 \text{ for } \frac{-\phi_c}{2} < \phi < \frac{\phi_c}{2} , \tag{2.9}$$

$$W(\rho_o, \phi) = \zeta_o^2 \text{ for } \frac{-\phi_c}{2} < \phi < \frac{\phi_c}{2} , \tag{2.10}$$

$$W\left(\rho, \frac{\phi_c}{2}\right) = W\left(\rho, \frac{-\phi_c}{2}\right) \text{ for } \rho_i < \rho < \rho_o , \tag{2.11}$$

$$W(\rho_s, \phi) = \zeta_s^2 \text{ for } \begin{cases} -\phi_t < \phi < \phi_t \\ \rho_i < \rho_s < \rho_o \end{cases} , \tag{2.12}$$

where $\zeta_o = \frac{\rho_o}{\rho_i}$ and $\zeta_s = \frac{\rho_s}{\rho_i}$.

Fourier Method

To solve Eqs. (2.8) through (2.12), the technique of separation of variables (Fourier's method) is applied to Eq. (2.8). Thus, it is assumed that the dependent variable, W, can be expressed in the form:

$$W(\rho, \phi) = R(\rho) \; \Phi(\phi) . \tag{2.13}$$

Substituting Eq. (2.13) into Eq. (2.8), the partial differential equation reduces to two ordinary differential equations:

$$-\frac{1}{\phi}\frac{d^2\Phi}{d\phi^2} = \frac{1}{R}\left(\rho^2\frac{d^2R}{d\rho^2} + \rho\frac{dR}{d\rho}\right) = \pm n^2 \quad . \tag{2.14}$$

In employing the Fourier method* of solving the Poisson equation with a novel boundary such as for flow in a rod-cluster geometry, one is faced with two judgments. The first is the choice of the eigenvalue $+n^2$ or $-n^2$; this requires anticipation of some of the properties of the final solution. The other is the division of the flow field into regions and the selection of boundary conditions in these regions in addition to the no-slip condition on the solid surfaces; again, this requires defining the proper boundary conditions and an anticipation of the properties of the final solution. Inexperience in these choices can — and did — lead to catastrophes when computer techniques are applied to the solution of Eq. (2.8) for flow in complex channels.

It is recognized qualitatively that the velocity at a fixed angle ϕ will first increase when departing along an outward normal from the surface of the central rod and then decrease as the outer shell is approached. This behavior suggests that $R(\rho)$ should be in the periodic form of sine and cosine functions. The fact that the velocity at a fixed radial distance increases with angle ϕ as ϕ increases from zero implies that $\Phi(\phi)$ is in the nonperiodic form of hyperbolic sine and cosine functions. This also is in accord with the known property of two-dimensional Poisson or Laplace equations that if $R(\rho)$ is a trigonometric function then $\Phi(\phi)$ is a hyperbolic function, and vice versa. The above line of reasoning dictates the choice of $-n^2$ as the proper eigenvalue.** From this, there results:

$$\Phi(\phi) = f(\sinh n\phi,\ \cosh n\phi) \text{ and } R(\rho) = g\ [\sin(n\,\ell n\,\rho),\ \cos\ (n\,\ell n\,\rho)] \quad .$$

---

*Other possible methods which have been explored are discussed later in this section.

**The choice of $+n^2$ should lead to the same solution, if properly obtained, as that found with $-n^2$; this aspect is discussed later in this section.

An early choice of the boundary condition,

$$\left.\frac{\partial u}{\partial \phi}\right|_{\phi = \phi_c/2} = 0 \quad ,$$

was found to be incorrect in that symmetry in velocity with respect to the radial plane, $\phi = \phi_c/2$, does not necessarily mean that the derivative is zero in this plane. Symmetry in $\Phi(\phi)$ with respect to the radial plane $\phi = 0$ remains; however, while u or Φ are continuous at $\phi = \phi_c/2$, $\partial\Phi/\partial\phi$ or $\partial u/\partial\phi$ exhibit a discontinuity. Further, investigation showed $u(\rho, \phi_c/2) = u(\rho, -\phi_c/2)$ to be the appropriate boundary condition for symmetry at $\phi = \phi_c/2$. As a result, the problem to be solved is not as simple as that originally formulated; in contrast, the solution is not as complicated as that found earlier.

Having chosen the eigenvalue, $-n^2$, the functions Φ and R take the following form:

$$\left.\begin{aligned} \Phi_n &= A_n \cosh n\phi + B_n \sinh n\phi \\ R_n &= C_n \cosh (n \ln \rho) + D_n \sin (n \ln \rho) \end{aligned}\right\} \text{for } n \neq 0 \qquad (2.15)$$

and

$$\left.\begin{aligned} \Phi_o &= A_o + B_o \phi \\ R_o &= C_o + D_o \ln \rho \end{aligned}\right\} \text{for } n = 0 \quad . \qquad (2.16)$$

Applying the first two boundary conditions [Eqs. (2.9) and (2.10)], there results

$$\left.\begin{aligned} C_n \cos (n \ln \rho_i) + D_n \sin (n \ln \rho_i) &= 0 \\ C_n \cos (n \ln \rho_o) + D_n \sin (n \ln \rho_o) &= 0 \end{aligned}\right\} \text{for } n \neq 0 \qquad (2.17)$$

and

$$\left.\begin{aligned} 1 &= C'_o + D'_o \ln \rho_i \\ \zeta_o^2 &= C'_o + D'_o \ln \rho_o \\ B_o &= 0 \end{aligned}\right\} \text{for } n = 0 \quad . \qquad (2.18)$$

For a nontrivial solution, it is necessary that

$$\cos(n \ln \rho_i) \sin(n \ln \rho_o) - \sin(n \ln \rho_i) \cos(n \ln \rho_o) = 0 \tag{2.19}$$

or

$$\sin(n \ln \zeta_o) = 0 \quad ; \tag{2.20}$$

i.e., that the eigenvalue be $n = mk$ for $m = 1, 2, 3 \ldots$

where

$$k = \frac{\pi}{\ln \zeta_o}$$

and

$$D_o' = \frac{\zeta_o^2 - 1}{\ln \zeta_o} \tag{2.21}$$

$$C_o' = \frac{(\zeta_o^2 - 1) \ln \rho_i}{\ln \zeta_o} \quad . \tag{2.22}$$

Thus,

$$C_m = -D_m \tan (mk \ln \rho_i) \tag{2.23}$$

and

$$W(\zeta, \phi) = 1 + (\zeta_o^2 - 1) \frac{\ln \zeta}{\ln \zeta_o} + \sum_{m=1}^{\infty} F_m \cosh mk\phi \sin(mk \ln \zeta); \tag{2.24}$$

and the solution is obtained in dimensionless form as:

$$u^*(\zeta, \phi) = \frac{u(\zeta, \phi)}{\left(\frac{-C_1 \rho_i^2}{4}\right)} = \left\{(\zeta_o^2 - 1) \frac{\ln \zeta}{\ln \zeta_o} - (\zeta_o^2 - 1) + \right.$$

$$\left. + \sum_{m=1}^{\infty} F_m \cosh mk\phi \sin(mk \ln \zeta) \right\} \tag{2.25}$$

$$1 < \zeta < \zeta_o, \quad \frac{-\phi_c}{2} < \phi < \frac{\phi_c}{2} \qquad m = 1, 2, 3 \ldots$$

and

$$k = \frac{\pi}{\ln \zeta_o}, \quad \zeta_o = \frac{\rho}{\rho_i}, \quad \zeta = \frac{\rho}{\rho_i} \qquad n = mk \quad .$$

The coefficients, F_m, can be determined by the extended point-match method[18,19] applied to the last boundary condition [Eq. (2.12)]. Thus,

$$\sum_{m=1} F_m \cosh mk\,\phi_s \sin(mk\,\ln \zeta_s) = (\zeta^2 - 1) - (\zeta_o^2 - 1)\frac{\ln \zeta}{\ln \zeta_o} \text{ for } 0 < \phi_s < \phi_t \,, \tag{2.26}$$

where

$$k = \frac{\pi}{\ln \zeta_o} \,, \quad \zeta_s = \frac{\rho_s}{\rho_i} \qquad m = 1, 2, 3 \ldots$$

$$\zeta_s^2 - 1 = \alpha^2 + 2\,\alpha \cos\theta \,,$$

$$\alpha = \epsilon\,(\zeta_o - 1) = \frac{d}{\rho_i} \,, \quad \epsilon = \frac{d}{\rho_o - \rho_i} = \text{eccentricity} \,,$$

$$\zeta_s = \sqrt{\alpha^2 + 2\,\alpha \cos\theta + 1} \,,$$

$$\phi_s = \arctan \frac{\sin\theta}{\alpha + \cos\theta} \quad \text{for } 0 < \theta < \pi \,,$$

and

d = distance between the centers of the central and peripheral rods.

A crude estimate of F_m for a seven-rod cluster with $\zeta_o = 5$ and $\epsilon = 0.8$ gives the result:

$$F_1 = -6.30558$$

$$F_2 = -1.55819$$

$$F_3 = -0.13553$$

$$F_4 = -1.28565$$

$$F_5 = -0.58302$$

Hence, the dimensionless velocity distribution for this arrangement is approximated by the expression:

---

[19] H. D. Conway, "Triangular Plates Analyzed by Point-Matching," J. Appl. Mech., 755–756 (December 1962).

$$u^*(\zeta, \phi) = (\zeta_o^2 - 1) \frac{\ln \zeta}{\ln \zeta_o} - (\zeta^2 - 1) - 6.30558 \cosh k\phi \sin(k \ln \zeta) +$$

$$+ 1.55819 \cosh 2k\phi \sin(2k \ln \zeta) - 0.13553 \cosh 3k\phi \sin(3k \ln \zeta) -$$

$$- 1.28565 \cosh 4k\phi \sin(4k \ln \zeta) - 0.54302 \cosh 5k\phi \sin(5k \ln \zeta) \quad . \tag{2.27}$$

A computer program will be written to determine more precisely the values of F_1, F_2, F_3, ..., F_{10} by point-match in the least-squares sense at 37 points (every 5 deg) along the boundary of the peripheral rod for the following configurations:

	ϕ_c	ζ_o	ϵ
5 rod	$\pi/2$	4, 5	0.8, 0.9
7 rod	$\pi/3$	4, 5	0.8, 0.9
9 rod	$\pi/4$	5	0.8, 0.9
13 rod	$\pi/2$	7	0.9
19 rod	$\pi/3$	7	0.9
25 rod	$\pi/4$	7	0.9

The velocity distribution will be calculated for these several configurations to allow for later comparisons as to flow rates and pressure drops, friction factors, local and average shear stresses, and heat transfer in a study of geometry optimization. The problem of forced-convection heat transfer will be tackled before turning to the more difficult two-phase annular flow problem.

Complex-Conjugate Method

The possibility of employing the complex-conjugate technique has been exlored,[20] since it is known that this method renders a solution in a very simple and elegant manner. Equation (2.6) [Poisson's equation] may be neatly expressed in the complex-conjugate coordinate system as,

$$\frac{\partial^2 u}{\partial z\, \bar{z}} = \frac{C_1}{4} \quad \text{at } \underline{R} \text{ (region)} \tag{2.28}$$

[20] L. V. Ahlfors, Complex Analysis, Chap. 5, pp. 175–208, McGraw-Hill Book Company, New York, 1953.

and

$$u = 0 \quad \text{at C (boundary)} \ . \tag{2.29}$$

The solution of this Dirichlet problem is simply:

$$u = \frac{C_1}{4} \cdot [z\,\bar{z} - f(g) - g(\bar{z})] \ . \tag{2.30}$$

The proof is relatively simple but is omitted here, since the solution satisfies the differential equation and hence is obviously correct. The problem then becomes one of finding $f(z)$ and $g(\bar{z})$; this depends entirely on whether the equation of the boundaries can be separated and expressed in the form:

$$z\,\bar{z} - f(z) - g(\bar{z}) = 0 \ . \tag{2.31}$$

A Dirichlet problem with boundary geometries (channel configurations) such as a triangle, half-moon, ellipse, or even a cardioid which is very difficult to solve in a Cartesian coordinate formulation becomes strikingly simple when the equation of the boundaries is written out. The equation of the boundaries of a simply connected domain would be the product of the boundaries. However, this does not apply for multiply connected domains. Even in a simply connected region, if the boundaries involve two or more segments of circular arc, this method fails due to the fact that the equation of boundaries would be $f(z\,\bar{z})$ instead of the more desirable form of Eq. (2.31). Since the boundaries in our problem of a rod cluster within a circular shell involve both the multiply connected domain and circular arcs, the possibility of using the complex-conjugate approach does not appear promising. However, this inquiry has helped greatly in understanding the close connection between the boundary and the solution.

Conformal-Mapping Method

Exploration of the method of conformal mapping indicated that only simply connected domains can be mapped conformally on a circle in a one-to-one manner.[21] This method depends vitally on the knowledge of the

[21] L. N. Tao, "Method of Conformal Mapping in Forced Convection Problems," Proceedings of the 1961-62 International Heat Transfer Conference, pp. 598–606, The American Society of Mechanical Engineers, New York, 1963.

mapping function. Again, this approach is ruled out by the multiply connected domain of this problem.

Green's-Function Method

It was found that the determination of the Green's function for a particular system as complicated as the one being considered here poses a more difficult problem than the original boundary-value problem.[22]

Alternate Eigenvalue Selection

If $+n^2$ is chosen as the eigenvalue in Eq. (2.14) instead of $-n^2$, the functions Φ and R would be in the form:

$$\left.\begin{aligned} \Phi_n(\phi) &= A_n \cos n\,\phi + B_n \sin n\,\phi \\ R_n(\rho) &= C_n\,\rho^n + D_n\,\rho^{-n} \end{aligned}\right\} \text{for } n \neq 0 \tag{2.32}$$

and

$$\left.\begin{aligned} \Phi_o &= A_o + B_o\,\phi \\ R_o &= C_o + D_o \ln \rho \end{aligned}\right\} \text{for } n = 0 \quad , \tag{2.33}$$

since on the boundary of the central rod and the outer shell the function W requires:

$$W\,(\rho_i,\ \phi) = 1 \tag{2.34}$$

$$W\,(\rho_o,\ \phi) = \zeta_o^2 \tag{2.35}$$

W is seen to be independent of ϕ on these surfaces. Hence,

$$\left.\begin{aligned} C_n\,\rho_i^n + D_n\,\rho_i^{-n} &= 0 \\ C_n\,\rho_o^n + D_n\,\rho_o^{-n} &= 0 \end{aligned}\right\} \text{for } n \neq 0 \tag{2.36}$$

and

$$\left.\begin{aligned} 1 &= C_o + D_o \ln \rho_i \\ \zeta_o^2 &= C_o + D_o \ln \rho_o \\ B_o &= 0 \end{aligned}\right\} \text{for } n = 0 \quad . \tag{2.37}$$

---

[22]S. H. Crandall, Engineering Analysis, McGraw-Hill Book Co., New York, p. 214, 1956.

If n is an integer, then the nontrivial solution W_n (for $n \neq 0$) is impossible.

On the other hand, there is a nontrivial solution of W_n if we do not impose the restriction that n be integral; i.e.,

$$\rho_o^{-n}\,\rho_i^{n} = \rho_o^{n}\,\rho_i^{-n} \quad \text{or} \quad \left(\frac{\rho_o}{\rho_i}\right)^{2n} = 1$$

or

$$n = \frac{i\,m\,\pi}{\ln \dfrac{\rho_o}{\rho_i}} \qquad m = 1,\ 2,\ 3\ \ldots$$

The negative values of m are omitted because they yield essentially the same characteristic functions as the positive ones.

$$\therefore\ R_n(\rho) = E_n\left[\left(\frac{\rho}{\rho_i}\right)^{n} - \left(\frac{\rho_i}{\rho}\right)^{n}\right]$$

or

$$R_n(\zeta) = E_n[\exp\,(n \ln \zeta) - \exp\,(-n \ln \zeta)] \quad ,$$

where

$$\zeta = \frac{\rho}{\rho_i} \quad .$$

When the value of n is replaced by m, there obtains:

$$R_m(\zeta) = F_m \sin\,(m\,k \ln \zeta)$$

and

$$\Phi_m(\phi) = A_m \cosh mk\phi + B_m' \sinh mk\phi \quad ,$$

where

$$k = \frac{\pi}{\ln \zeta_o} \quad .$$

Thus, the solution is in the same form as that derived from the one in which $-n^2$ is chosen. The only difference is that by selecting the alternate eigenvalue $+n^2$, the solution first appears in terms of cos $n\phi$, sin $n\phi$,

ρ^n, and ρ^{-n} and must be converted to the form cosh $mk\phi$, sinh $mk\phi$, sin $(mk \ln \rho)$, and cos $(mk \ln \rho)$ through the definition of $n = im\pi/\ln \zeta_o$. In contrast, when $-n^2$ is selected, the solution in the form of cosh $mk\phi$ and sin $(mk \ln \rho)$ is more apparent.

3. FLOW DYNAMICS AND TURBULENCE

3.1. Vortex Fluid Mechanics – Hydromagnetic Stabilization

T. S. Chang J. J. Keyes, Jr. W. K. Sartory

The analytical and experimental investigation into the dynamics of vortex-like flows was continued,[23,24] with emphasis on the effect of a uniform axial magnetic field on the stability of vortex motion of an electrically conducting fluid.

3.1.1. Theoretical Studies

With regard to the analytical program, more general characteristic solutions for hydromagnetic stabilization have been considered. For example, equations for vortex-like flow with or without radial flow have been derived and the associated boundary conditions established. Recent analyses[25,26] have shown that for an incompressible, conducting, inviscid pure-vortex flow,* or nondissipative vortex-like flow,** exact criteria for hydromagnetic stabilization may be deduced. Additional analyses[27,28]

---

[23]H. W. Hoffman et al., "Fundamental Studies in Heat Transfer and Fluid Mechanics, Status Report July 1, 1959 – February 29, 1960," USAEC Report ORNL CF-60-10-6, Oak Ridge National Laboratory, October 1960.

[24]H. W. Hoffman and J. J. Keyes, Jr., "Studies in Heat Transfer and Fluid Mechanics Progress Report for Period Jan. 1 – Sept. 30, 1963," USAEC Report ORNL-TM-915, pp. 41–78, Oak Ridge National Laboratory, October 1964.

[25]T. S. Chang, "Hydromagnetic Stabilization of Nondissipative Vortex Flow," Proceedings of the Second Southeastern Conference on Theoretical and Applied Mechanics, Pergamon Press, New York (to be published in 1964).

[26]T. S. Chang, "Exact Criterion of Hydromagnetic Stability of Inviscid Vortex Flow with Finite Conductivity," presented at the First Annual Meeting and Technical Display of the American Institute of Aeronautics and Astronautics, Washington, D. C., June 28 – July 2, 1964.

[27]T. S. Chang and W. K. Sartory, "Hydromagnetic Stability of Dissipative Vortex Flow," submitted for publication in the Physics of Fluids (1964).

[28]T. S. Chang and W. K. Sartory, "Hydromagnetic Stability of Vortex-Like Flow," USAEC Report ORNL-3707, Oak Ridge National Laboratory (in preparation).

*A two-dimensional, axisymmetric flow whose tangential velocity varies as $(\text{radius})^{-1}$.

**Any axisymmetric flow satisfying the basic steady-state equations [see Eqs. (3.1) through (3.4)].

pertaining to the stability of dissipative, pure-vortex flow, and vortex-like flow have also been completed.

The following is a detailed description of the recent analytical work:

I. A Class of Stationary Vortex-Like Solutions with Axial Symmetry

It was found that the basic equations of magnetohydrodynamics contain a class of exact stationary solutions with axial symmetry. They are listed as follows:

$$Q_r = \frac{K_2}{r} , \tag{3.1}$$

$$Q_\theta = \frac{K_4}{r} + \frac{K_3}{K_2/\nu + 2} r^{K_2/\nu + 1} , \tag{3.2}$$

$$Q_z = 0 , \tag{3.3}$$

$$P = \rho \left[K_5 - \frac{K_2^2 + K_4^2}{2 r^2} + \frac{2 K_3 K_4}{K_2/\nu (K_2/\nu + 2)} r^{K_2/\nu} + \right.$$

$$\left. + \frac{K_3^2}{2 (K_2/\nu + 1)(K_2/\nu + 2)^2} r^{2(K_2/\nu + 1)} \right] , \tag{3.4}$$

where Q_r, Q_θ, and Q_z are the cylindrical components of the flow velocity, P is the fluid pressure, K's are constants, ν is the kinematic viscosity, r is the radial coordinate, and z is the axial coordinate. This class of two-dimensional solutions is independent of the finite conductivity of the fluid medium and the externally applied uniform axial magnetic field.

II. Perturbation Equations for the Study of the Stabilization of Vortex-Like Flow

Neglecting the effect of axial flow, the perturbation equations for the stability of vortex-like flow are found to reduce to a set of coupled equations given in Eq. (3.5):

$$\left(i\,\alpha - \frac{F}{N_{Re_\theta,\eta}} + G_-\right) F\, y_1 + 2\,\beta^2 \left[\frac{L}{x^2} + \frac{2\,M}{N_{Re_r,\eta} + 2}\, x^{N_{Re_r,\eta}}\right] y_2 -$$

$$- \frac{\beta}{\eta^2\, N^2_{A\ell,\eta}}\, F\, y_3 = 0 \;,$$

$$2\,M\, x^{N_{Re_r,\eta}}\, y_1 + \left(i\,\alpha - \frac{F}{N_{Re_\theta,\eta}} + G_+\right) y_2 - \frac{\beta}{\eta^2\, N^2_{A\ell,\eta}}\, y_4 = 0 \;,$$

$$\beta\, y_1 + \left(i\,\alpha - \frac{F}{N_{Re_m,\eta}} + G_+\right) y_3 = 0 \;, \tag{3.5}$$

$$\beta\, y_2 + 2\left(\frac{L}{x^2} - \frac{M\, N_{Re_r,\eta}}{N_{Re_r,\eta} + 2}\, x^{N_{Re_r,\eta}}\right) y_3 + \left(i\alpha - \frac{F}{N_{Re_\theta,\eta}} + G_-\right) y_4 = 0 \;,$$

where

$$F = \frac{d^2}{dx^2} + \frac{1}{x}\frac{d}{dx} - \frac{1}{x^2} - \beta^2 \;,$$

$$G_\pm = \frac{k}{x}\left(\frac{d}{dx} \pm \frac{1}{x}\right) \;,$$

where $N_{Re_\theta,\eta}$ is the characteristic transverse (tangential) Reynolds modulus, $N_{Re_r,\eta}$ is the characteristic radial Reynolds modulus, $N_{Re_m,\eta}$ is the characteristic magnetic Reynolds modulus, $N_{A\ell,\eta}$ is the characteristic Alfvén modulus, k is the ratio of the characteristic radial velocity to the transverse velocity, α is the dimensionless frequency parameter, β is the dimensionless wave number, y_1, y_2, y_3, and y_4 are the dimensionless perturbation functions, x is the dimensionless radial coordinate, L and M are constants, $\eta = r_o/r_2$, r_2 is the outer cylinder radius, and r_o is an arbitrary radius used in defining the dimensionless parameters.

III. Stabilization of Nondissipative Pure-Vortex Flow

It was found[25,28] that pure vortex flow of a perfectly conducting, nondissipative medium enclosed within two concentric cylindrical walls can be stabilized against the breakdown of laminar motion by means of an axially applied magnetic field. The following conclusions were reached during this phase of the analysis:

1. An exact criterion for magnetic stabilization may be obtained for an inviscid, perfectly conducting, pure-vortex flow contained within two nonpermeable walls. The criterion expressed in algebraic form is as follows:

$$J_1 \; (2 \; N_{A\ell}) \; Y_1 \; (2 \; N_{A\ell}/\kappa) - J_1 \; (2 \; N_{A\ell}/\kappa) \; Y_1 \; (2 \; N_{A\ell}) = 0 \quad , \qquad (3.6)$$

where J_1 and Y_1 are Bessel functions of the first and second kind or order of one, respectively; and $N_{A\ell}$ is the peripheral Alfvén modulus. Numerical results are presented graphically in Figs. 3.1 through 3.3.

2. There exists a close agreement among the approximate results of the earlier analyses[29-31] and the exact criterion.

3. Such a pure vortex flow is intrinsically unstable without an axially applied magnetic field. The paradox between this conclusion and Rayleigh's criterion[32] lies in the assumption of the nondissipative nature of the fluid medium.

4. The magnetic field for marginal stabilization decreases with the increase of the radius ratio (Fig. 3.1).

---

[29]T. S. Chang, "Magnetohydrodynamic Stability of Vortex Flow — a Nondissipative, Incompressible Analysis," USAEC Report ORNL-TM-402, Oak Ridge National Laboratory, October 23, 1962.

[30]E. P. Velikhov, "Stability of an Ideally Conducting Liquid Flowing Between Cylinders Rotating in a Magnetic Field," J. Exptl. Theoret. Phys. (USSR), 36: 1398–1404 (1959).

[31]S. Chandrasekhar, "The Stability of Nondissipative Couette Flow in Hydromagnetics," Proc. Natl. Acad. Sci., 46: 253–257 (1960).

[32]Lord Rayliegh, "On the Dynamics of Revolving Fluids," Scientific Papers, Cambridge, England, 6: 447–463 (1920).

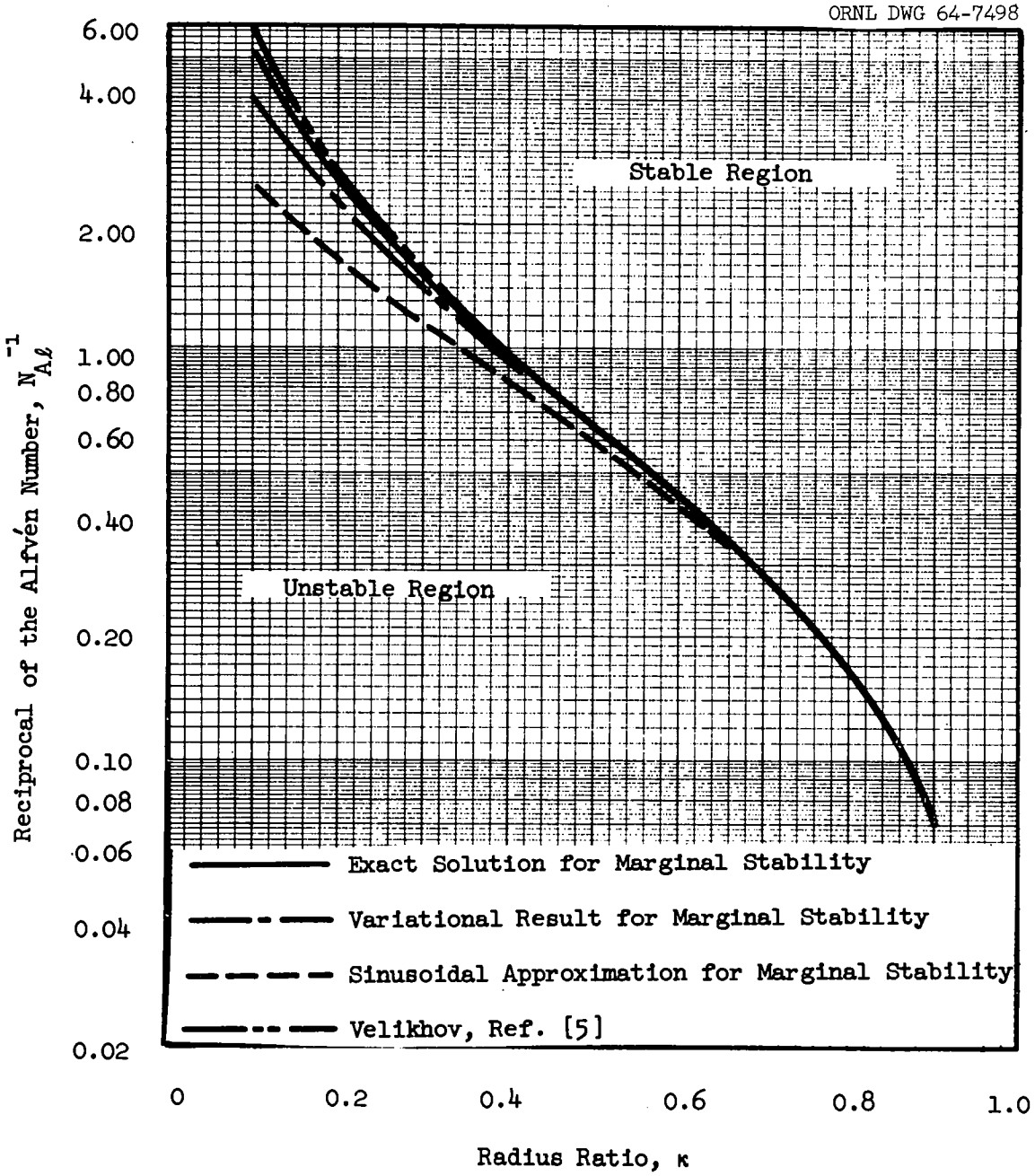

Fig. 3.1. Criterion for Magnetic Stabilization of Nondissipative Vortex Flow.

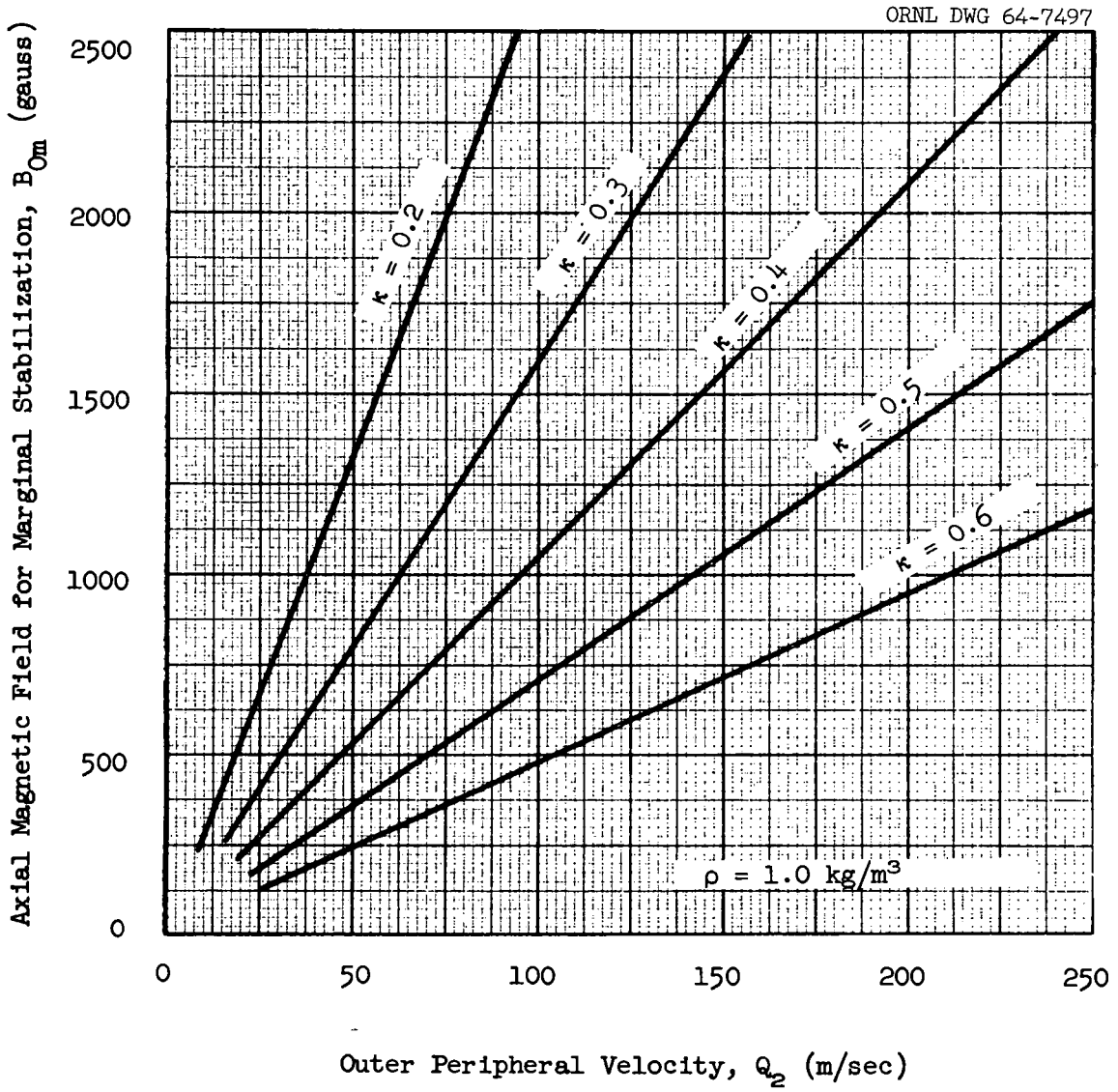

Fig. 3.2. Dependence of the Magnetic Field for Marginal Stabilization on the Outer Peripheral Velocity of the Vortex.

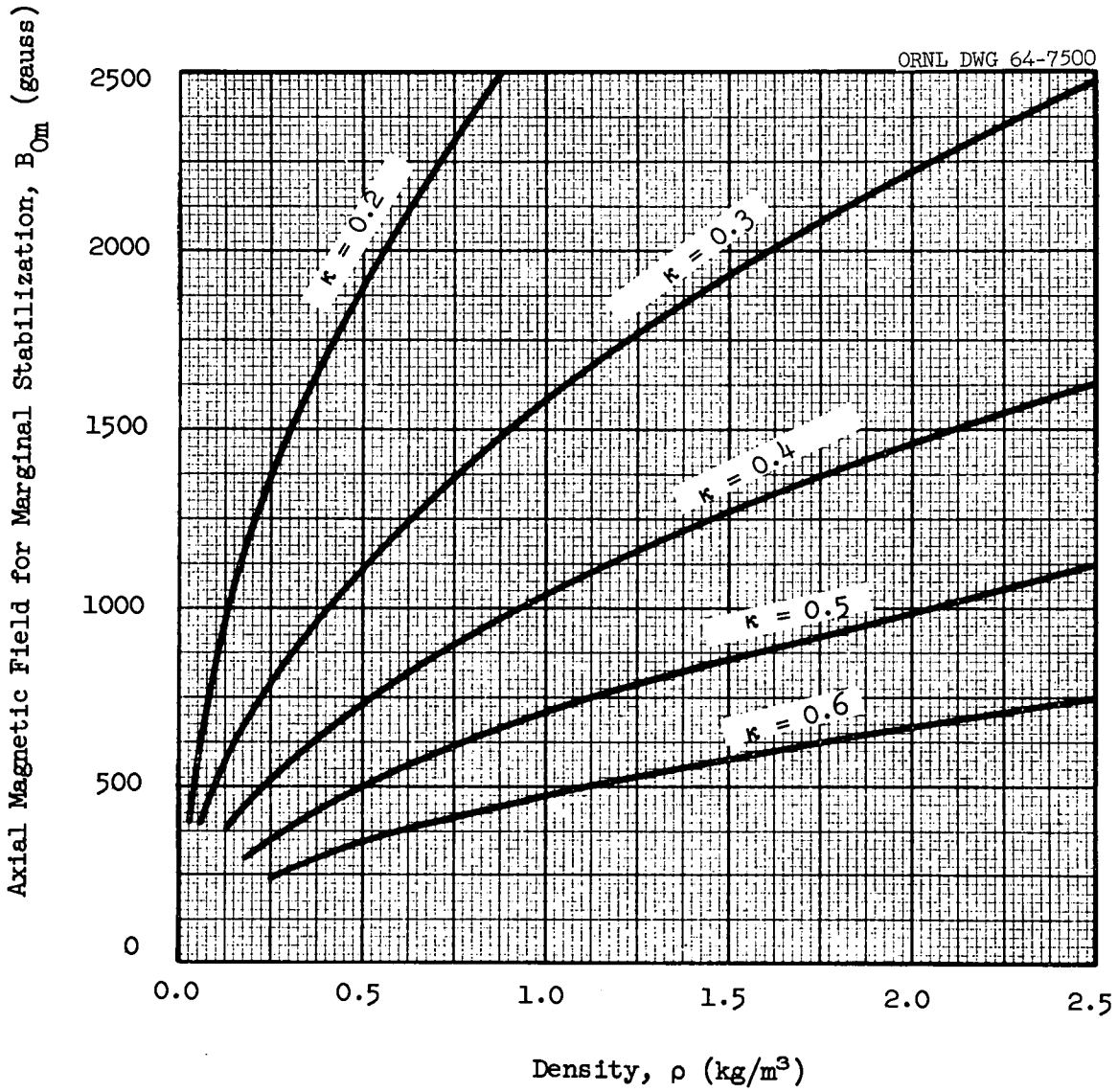

Fig. 3.3. Dependence of the Magnetic Field for Marginal Stabilization on the Fluid Density.

5. The magnetic field for marginal stabilization increases linearly with the outer peripheral velocity of the vortex (Fig. 3.2).

6. The magnetic field for marginal stabilization increases parabolically with the density of the fluid (Fig. 3.3).

IV. Exact Criterion of Hydromagnetic Stability of Inviscid Vortex Flow with Finite Conductivity

The purpose of this portion of the investigation was to consider the possible effects of the finite conductivity of the working medium on the criterion of magnetic stabilization. The following conclusions were reached during this phase of the analysis:[26]

1. It is possible to stabilize the motion of an inviscid pure vortex motion with finite conductivity by means of an axially applied uniform magnetic field.

2. The criterion for magnetic stabilization may be expressed in terms of a simple algebraic expression identical to that for nondissipative flow [Eq. (3.6)].

3. The exact criterion for magnetic stabilization is determined by the marginal value of the reciprocal of the peripheral Alfvén modulus.

4. The marginal magnitude of the applied magnetic field is related to the radius ratio, the density of the fluid, and the peripheral speed of the vortex.

5. The criterion for magnetic stabilization is related indirectly to the finite conductivity of the fluid medium. It is derived by assuming that the marginal state of stability is due to a secondary flow and that the finite conductivity of the medium is not negligibly small.

V. Exact Criterion of Hydromagnetic Stabilization of Nondissipative Vortex-Like Flow

An exact solution[28] considering the stabilization of nondissipative, perfectly conducting, vortex-like flow by means of an axially applied magnetic field was obtained; and it was shown that algebraic expressions may be deduced for the determination of the criterion if the critical

perturbations are assumed to be due to the axisymmetrical normal modes. The parameters which determine the stability criterion are a new characteristic Alfvén modulus and a dimensionless number characterizing the shape of the velocity profile. The criterion includes the result for pure-vortex flow as a special case. For small radius ratios and velocity profiles approaching that of a pure vortex, the criterion converges toward the pure-vortex result.

The deduced results are summarized as follows:

1. An exact criterion for hydromagnetic stabilization of nondissipative, vortex-like flow must be stated separately for the following cases:

a. "$\lambda = 0$"

The dimensionless parameter λ characterizes the shape of the transverse velocity profile. For $\lambda = 0$, we have a pure vortex and the result is given in Eq. (3.6).

b. "$0 > \lambda > -\kappa^{-2}$"

The criterion for this case is:

$$J_p\,(2\,N_{A\ell})\,Y_p\,(2\,N_{A\ell}/\kappa) - J_p\,(2\,N_{A\ell}/\kappa)\,Y_p\,(2\,N_{A\ell}) = 0 \quad , \qquad (3.7)$$

$$p = (1 - 4\,N_{A\ell}^2\,\lambda)^{1/2} \quad ,$$

where J_p and Y_p are Bessel functions of the first and second kind of order p, respectively, and $N_{A\ell}$ is the new characteristic Alfvén modulus.

Some typical graphs of the above expressions are shown in Fig. 3.4.

c. "$\lambda < -\kappa^2$"

The velocity profile in this case is always stable.

d. "$\lambda > 0$ and $4\,N_{A\ell}^2\,\lambda \leq 1$"

In this case, the criterion is the same as case b. Typical curves are shown in Fig. 3.4.

e. "$\lambda > 0$ and $4\,N_{A\ell}^2\,\lambda \geq 1$"

The criterion in this case becomes:

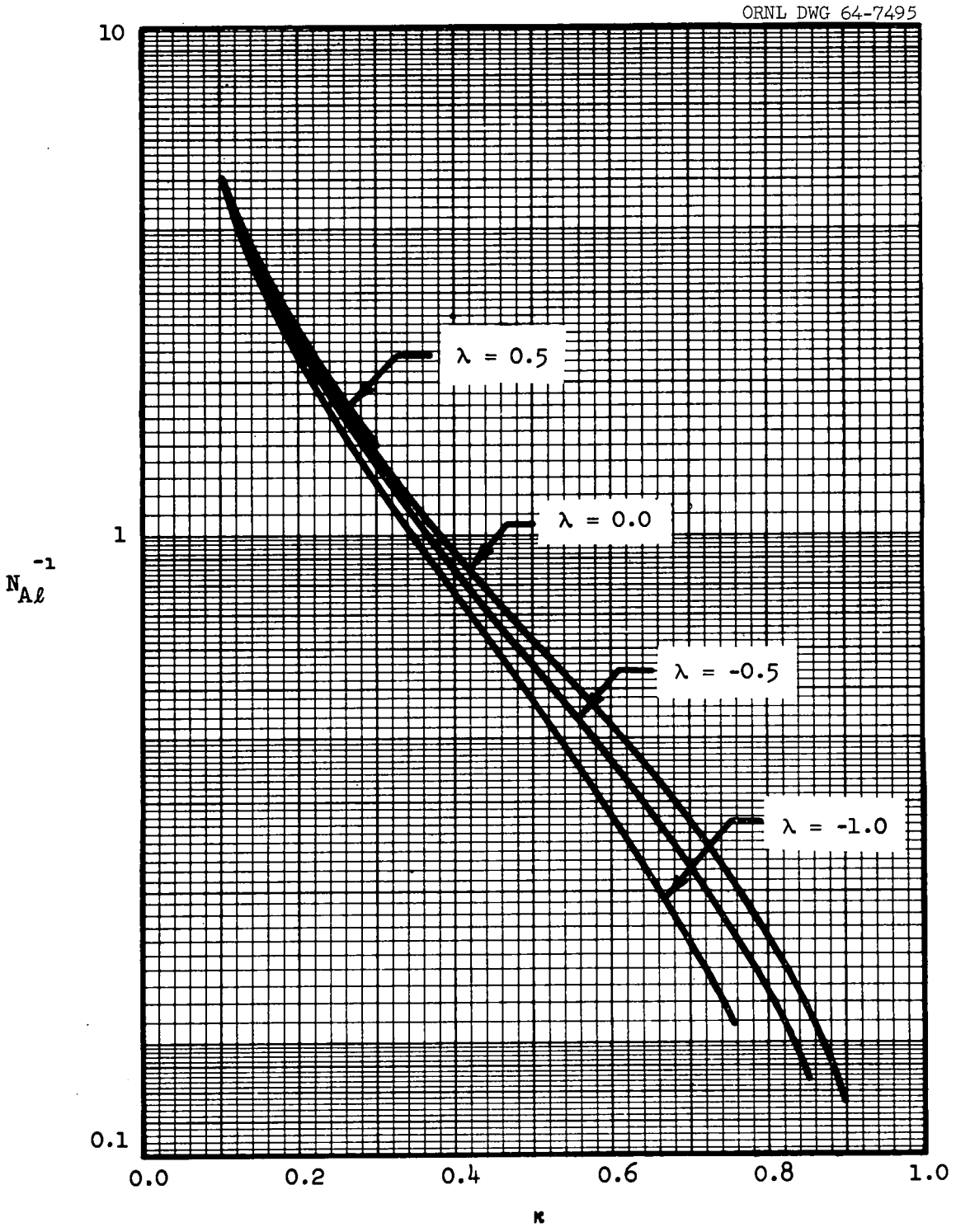

Fig. 3.4. Criterion for Magnetic Stabilization of Nondissipative Vortex-Like Flow.

$$K_{o,m}(2\ N_{A\ell})\ S_{o,m}(2\ N_{A\ell}/\kappa) - K_{o,m}(2\ N_{A\ell}/\kappa)\ S_{o,m}(2\ N_{A\ell}) = 0 \quad , \qquad (3.8)$$

$$m = (4\ N_{A\ell}^2\ \lambda - 1)^{1/2} \quad ,$$

where $K_{o,m}$ and $S_{o,m}$ are the Boole functions[33] of the first and second kind of order (o,m), respectively.

The calculations for the above expressions are being considered and should be available in the near future.

2. The criterion is applicable to any vortex-like profile with the exception of rigid body rotation which yields a trivial result.

3. For small values of the radius ratio, it is expected that the condition for larger values of $4\ N_{A\ell}^2\ \lambda$ is only of formal interest. In fact, for very small values of the radius ratio and relatively small values of λ, the criterion converges toward the pure-vortex result.

VI. Dissipative Pure-Vortex Flow

This case is obtained from Eq. (3.5) by putting $N_{Re_r} = k = M = 0$. It is convenient to choose $\eta = 1.0$ and to drop the subscript η from the dimensionless parameters. The stability can be characterized by the radius ratio, κ, the parameter $\overline{Q} = (1 - \kappa)^2\ N_{Re_\theta}\ N_{Re_m}\ N_{A\ell}^{-2}$, and $N_{\overline{Re}_\theta} = (1 - \kappa)^2\ N_{Re_\theta}\ N_{Re_m}\ f^{-2}$ where f is a function of κ only, defined as the smallest solution of the equation:

$$J_1(2\ f)\ Y_1(2\ f/\kappa) - J_1(2\ f/\kappa)\ Y_1(2\ f) = 0 \quad . \qquad (3.9)$$

Comparing Eqs. (3.9) and (3.6), we see that <u>if the flow were nondissipative</u> f would be equal to the critical Alfvén modulus.

The results were obtained by numerical solution of the stability equations and are graphed in Fig. 3.5.

It was found that:

1. In the limit as both the viscosity and electrical resistivity approach zero, agreement is obtained with the nondissipative results of

---

[33]G. Boole, Phil. <u>Trans. Roy. Soc. (London)</u>, 239 (1844).

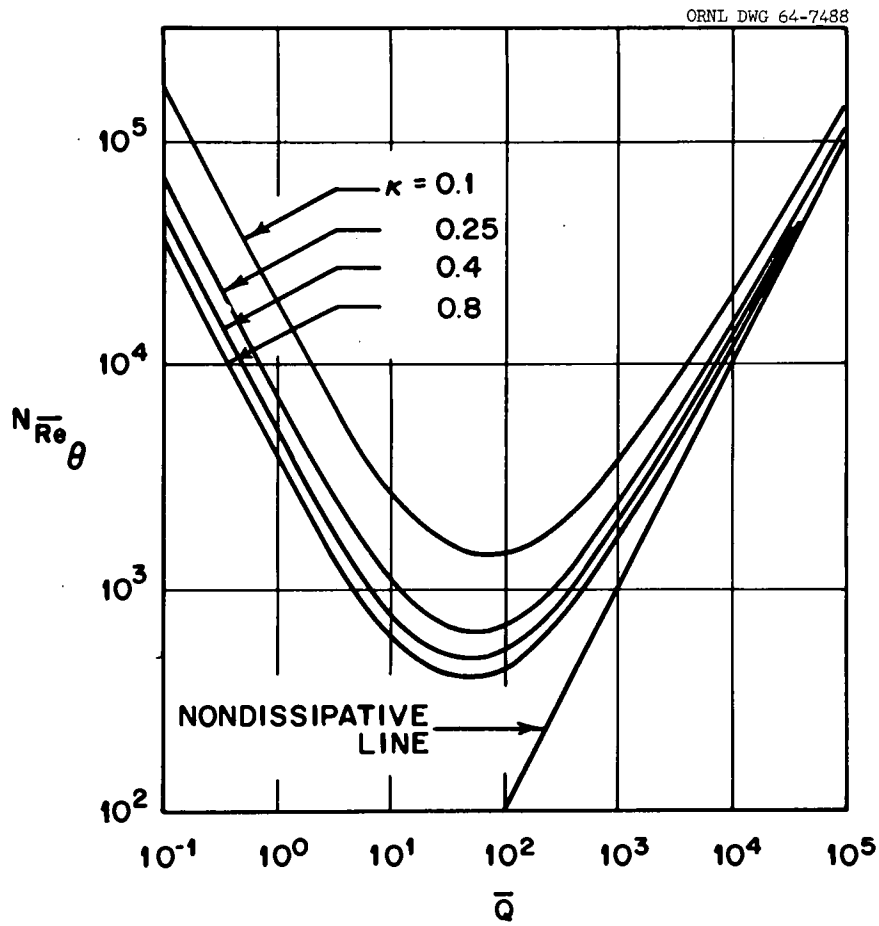

Fig. 3.5. Critical Tangential Reynolds Modulus vs $\overline{Q}$.

Section III; and as the viscosity approaches zero with finite conductivity, the results are in agreement with Section IV.

2. As the magnetic field approaches zero, the results are consistent with the nonmagnetic stability criterion of Rayleigh[34] and Taylor.[35]

3. When $\overline{Q}$ is large, an increase in the magnetic field strength tends to stabilize the flow; but when $\overline{Q}$ is small, an increase in the field can make the flow less stable.

4. An increase in the electrical conductivity never stabilizes the flow but, particularly with a weak magnetic field, can cause instability.

VII. Dissipative Vortex-Like Flow

When the effects of finite viscosity and electrical conductivity are included in the analysis of vortex-like flow, the following parameters are useful in characterizing the stability:

$$N_{\overline{Ta}} = -2 \frac{(1-\kappa)^4 (1-\kappa^2)}{\kappa^2} M L N^2_{Re_{\theta},\eta}, \text{ the Taylor number,}$$

$$\overline{Q} = (1-\kappa)^2 \frac{N_{Re_{\theta},\eta} N_{Re_m,\eta}}{\eta^2 N^2_{A\ell,\eta}},$$

κ = radius ratio,

μ = the ratio of angular velocity of the inner cylinder to that of the outer cylinder,

$$N_{Pr_m} = N_{Re_m,\eta}/N_{Re_{\theta},\eta} .$$

The definitions are given in terms of quantities appearing in Eq. (3.5). For this case, there is no radial flow, $N_{Re_r} = 0$.

N_{Pr_m} is a fluid property which, for most fluids, is less than about 10^{-6} so the approximation $N_{Pr_m} = 0$ has been made. Thus far only the case of a stationary outer wall, $\mu = 0$, has been completed.

---

[34]Lord (J. W. S.) Rayleigh, Scientific Papers, Cambridge, England, 6: 447 (1920).

[35]G. I. Taylor, Phil. Trans. Roy. Soc. (London), A223: 289 (1923).

The results were obtained by numerical solution of the stability equations and are graphed in Fig. 3.6.

It was found that:

1. Unlike the case of pure-vortex flow, an increase in magnetic field strength is always stabilizing.

2. When $\bar{Q}$ is small, approximate agreement is obtained with the narrow-gap results of Chandrasekhar.[36]

3. As $\bar{Q}$ becomes very large, $N_{\overline{Ta}}$ becomes proportional to $\bar{Q}^2$, indicating that the stability becomes independent of viscosity. Chandrasekhar's narrow-gap results, on the other hand, indicate that $N_{\overline{Ta}}$ becomes proportional to $\bar{Q}$ itself.

4. When $\bar{Q}$ is very large, the disturbance which produces instability becomes smaller and is confined to a narrow region near the inner cylinder. The stability is then determined by the shape of the velocity profile in some small neighborhood of the inner wall.

VIII. The Effect of Superimposed Radial Flow

The calculations of Section VII have been extended to include the effect of outward radial flow superimposed on the primary rotating flow. Numerical solution of the stability equations was used; and the results are reported in Figs. 3.7 through 3.10 in terms of the tangential Reynolds modulus defined by

$$N_{Re_\theta,0.8} = \frac{Q_{\theta,0.8}\, r_2}{\nu} ,$$

where $Q_{\theta,0.8}$ is the tangential velocity at 0.8 of the outer radius, r_2. The radial Reynolds modulus, N_{Re_r}, is also important in the correlation of the results.

The following conclusion can be drawn:

1. The effect of increasing the outward radial flow is usually stabilizing, although there are some regions in which a slight decrease in

[36] S. Chandrasekhar, Hydrodynamic and Hydromagnetic Stability, Oxford University Press, New York, 1961.

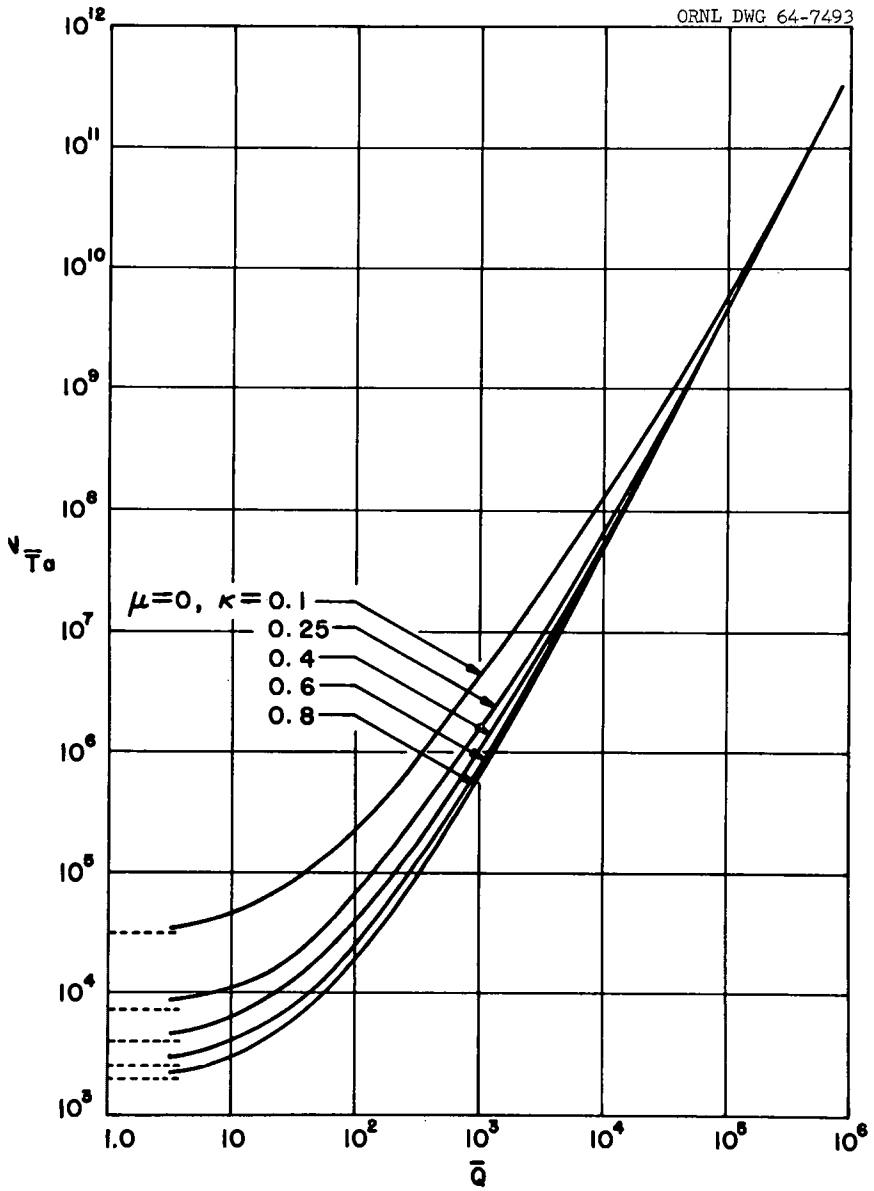

Fig. 3.6. Critical Taylor Modulus vs $\overline{Q}$.

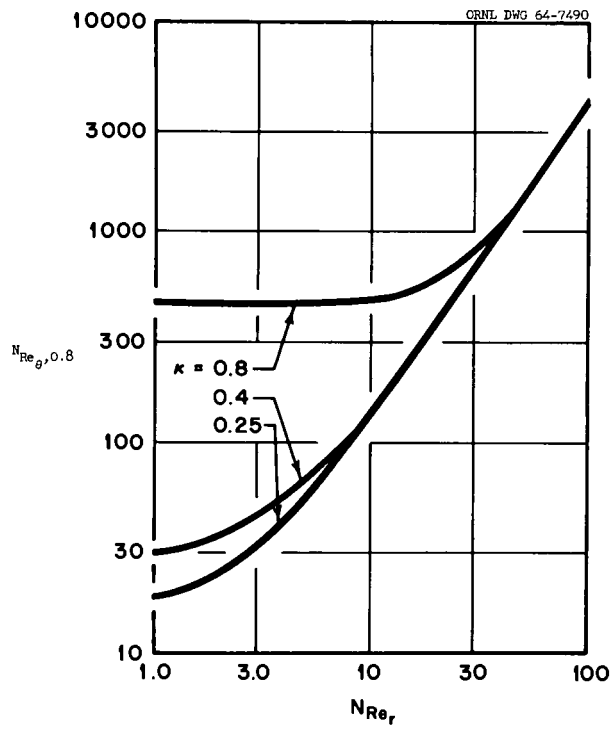

Fig. 3.7. Critical Tangential Reynolds Modulus Versus Radial Reynolds Modulus, $\overline{Q} = 0$.

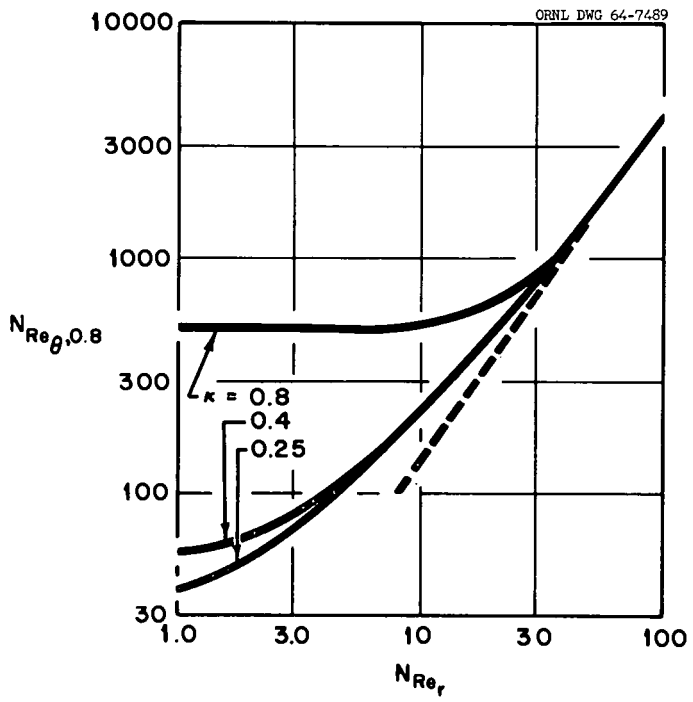

Fig. 3.8. Critical Tangential Reynolds Modulus Versus Radial Reynolds Modulus, $\overline{Q}$ = 100.

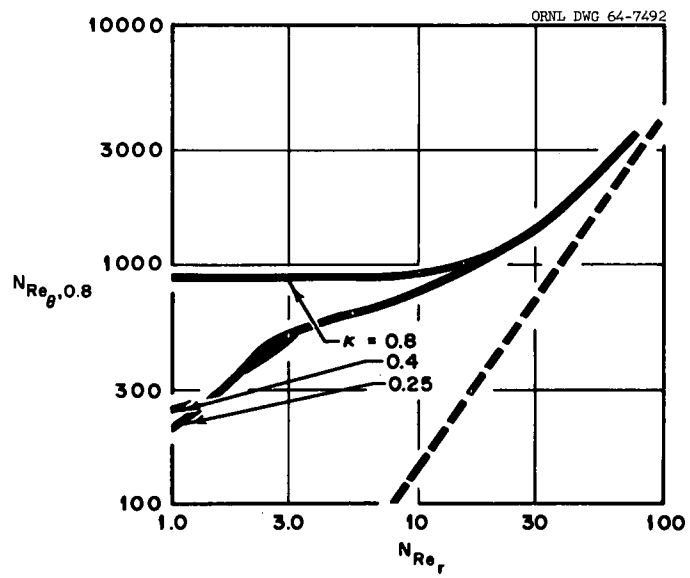

Fig. 3.9. Critical Tangential Reynolds Modulus Versus Radial Reynolds Modulus, $\overline{Q}$ = 1000.

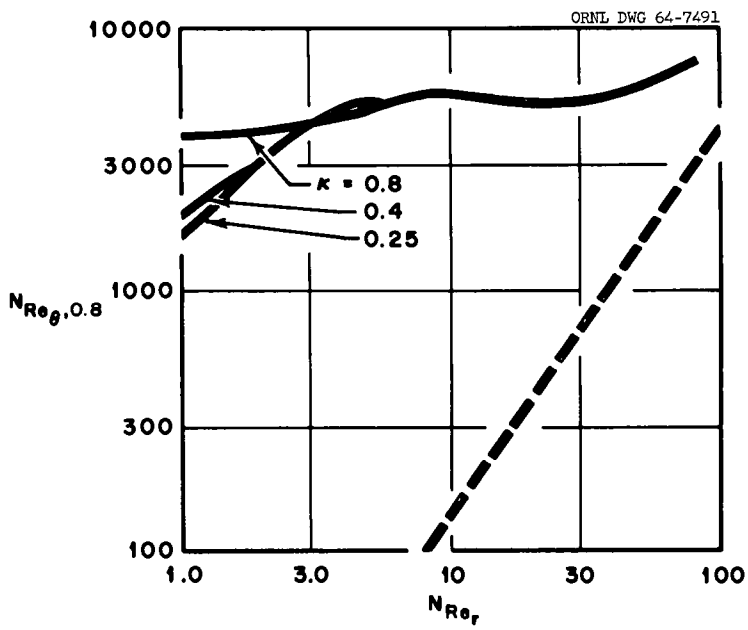

Fig. 3.10. Critical Tangential Reynolds Modulus Versus Radial Reynolds Modulus, $\bar{Q}$ = 10,000.

stability occurs.

2. As N_{Re_r} is increased, the disturbance becomes confined to a region near the outer wall. When this occurs, the location of the inner wall becomes unimportant and the curves for various values of the radius ratio converge.

3. Although both radial flow and an axial magnetic field tend to stabilize the flow, a large value of $\overline{Q}$ tends to decrease the effectiveness of radial flow as a means of stabilization. Similarly, a large value of N_{Re_r} decreases the effectiveness of a magnetic field.

4. When N_{Re_r} is very large, the critical value of $N_{Re_\theta,0.8}$ becomes asymptotically proportional to $N_{Re_r}^{3/2}$ and all of the curves approach the same asymptote.

Future analytical work will extend the numerical results to include inward radial flow, as well as rotation of the outer wall, for comparison with published wide-gap, Couette flow, hydromagnetic stability theory. A one-term nonlinear perturbation effect will also be considered in conjunction with the hydromagnetic stability of dissipative Couette flow for the special case of the outer wall stationary. It is further proposed to initiate an investigation of the stability of a single, two-dimensional, jet impinging tangentially on a concave boundary layer in order to include a case more directly related to the physical problem.

3.1.2. Experimental Studies

The exploratory experimental investigation was extended to include a study of the effect of injection geometry on hydromagnetic stability of confined, jet-driven vortex flow. Recall that the working fluid employed in this investigation is a concentrated aqueous solution of ammonium chloride (NH_4Cl) whose electrical conductivity at 200°F, the temperature of the experiments, is 0.84 mho/cm or about that of a low-temperature, alkali-metal seeded plasma. A uniform axial magnetic field of up to 74,000 gauss was provided by the double coil, 6.5-in. diameter, Large Volume Test Magnet (LVTM) located in the ORNL Magnet Laboratory. Figure 3.11 depicts the flow diagram for the experiment. Photographs were

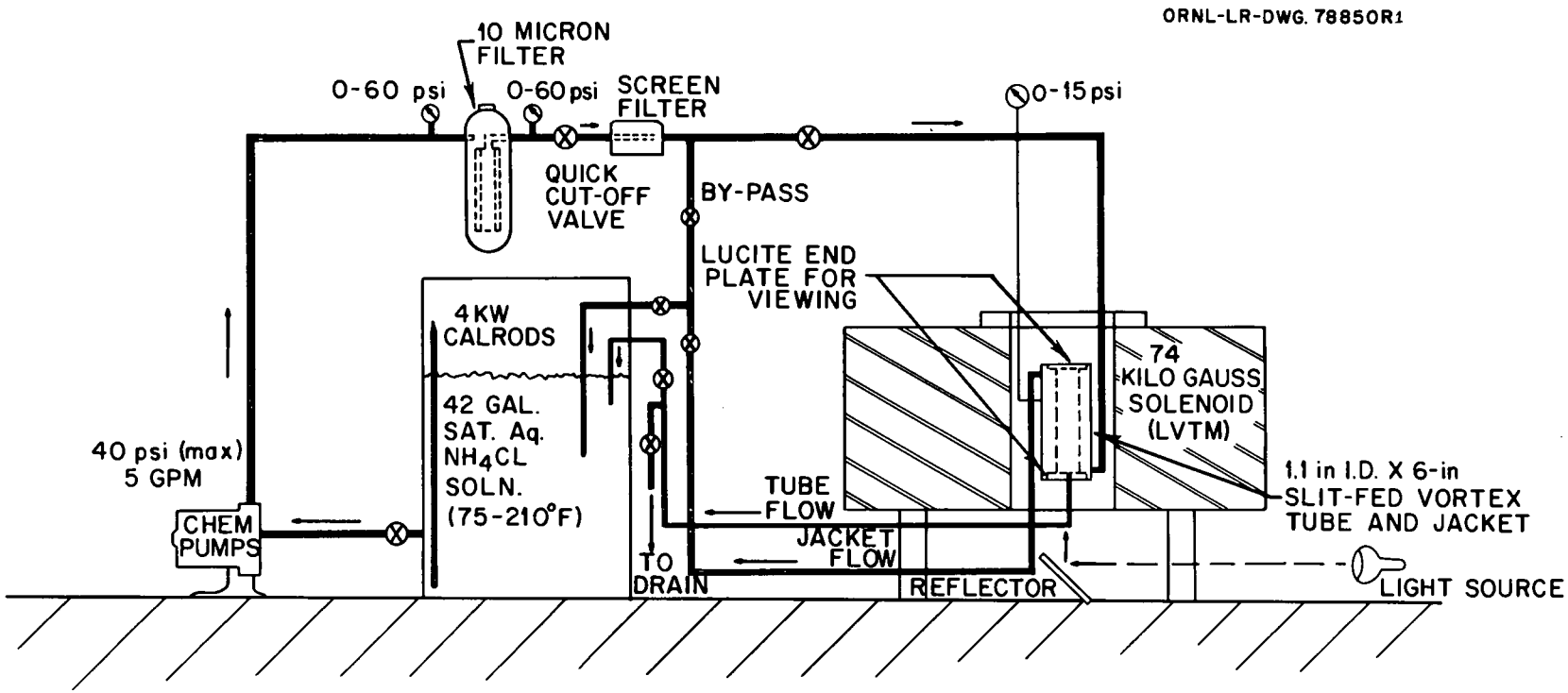

Fig. 3.11. Schematic Flow Diagram for MHD Experiment No. 1.

obtained by viewing in the axial direction (from above) through transparent plastic end walls.

Two vortex tubes employed in the recent studies are illustrated in cross section in Fig. 3.12. The tubes are each 1.1-in. ID by 6 1/2 in. long, fabricated of brass, and differ only in the geometry of the fluid injection system. The tube depicted at the left has eight 0.007-in. wide by 5 3/4-in. long slits (wall jets) for vortex generation, while the tube at the right has 880 round nozzles of 0.020-in. diameter arranged in eight rows and uniformly spaced along the length of the tube; the total area of these eight slits is about the same as that of the 880 round nozzles. The axes of both the slits and the nozzles intersect a radial position of 9/10 of the tube radius. The theoretical average ratio of tangential-to-radial velocity near the periphery with this geometry is about 40. The jets are fed from an annulus as indicated, and the fluid is withdrawn at the center of one end. The flow pattern is thus an inward spiral with increasing axial velocity corresponding to decreasing radius. There is no evidence of a recirculation pattern at the conditions of this study.

Observation of dye filaments injected into the boundary layer on the concave wall at the three circumferential positions indicated is the primary technique employed for determining effects of the magnetic field on flow stability. These dye injection positions are located approximately midaxially with respect to tube length.

The principle similarity parameters employed in correlating the experimental results include the tangential Reynolds modulus based on a radius ratio of 0.8,

$$N_{Re_\theta,0.8} = r_2 \, Q_{\theta,0.8} \, \rho/\mu \quad ,$$

the peripheral radial Reynolds modulus,

$$N_{Re_r} = r_2 \, Q_r \, \rho/\mu \quad ,$$

the peripheral magnetic interaction parameter,

$$N_S = \sigma \, r_2 \, B_0^2/\rho \, Q_{\theta,0.8} \quad ,$$

ORNL-DWG. 64-5410

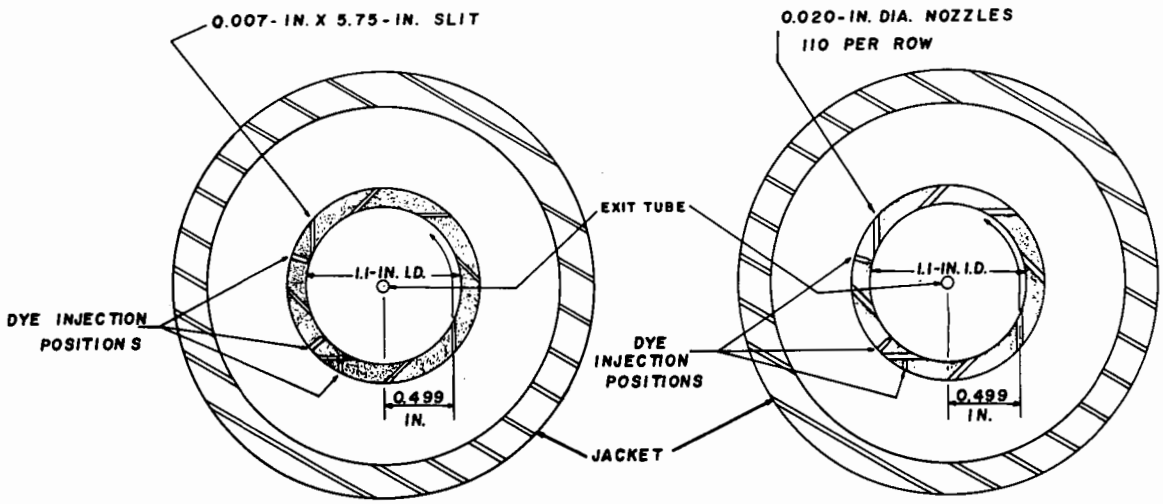

Fig. 3.12. Vortex Tubes (1.1-in. Diameter) for MHD Studies.

and the square of the Hartmann modulus,

$$N_{Ha}^2 = \frac{\sigma}{\mu} r_2^2 B_0^2 .$$

In these expressions, r_2 is the tube radius, $Q_{\theta,0.8}$ is the tangential velocity at a radius ratio of 0.8, Q_r is the peripheral radial velocity, B_0 is the magnetic induction, ρ is the density, μ is the absolute viscosity,* and σ is the electrical conductivity.

The most striking observation of the effect of the axial magnetic field is the suppression of what might generally be described as "flow instabilities of an apparent oscillatory nature," which seem to originate in the boundary layer along the concave wall at low values of the peripheral tangential Reynolds modulus and to initiate instability, characterized by gross radial convection, in the interior of the flow field. The influence of the magnetic field for the case of the vortex flow generated by 8 by 0.007-in. plane slits is shown in Fig. 3.13, in which dye is injected downstream from one of the slits. With no applied magnetic field, $N_{Ha} = 0$ (upper half of the figure), instability is already evident at $N_{Re\theta,0.8} = 700$ by the apprearance of significant radial mixing and absence of any well-defined spiral flow pattern. Note also the large-scale vortex shedding from the lip of an injection slit. When the 74-kilogauss axial field is applied to give $N_{Ha} \cong 47$, strong stabilization is evidenced by the formation of a well-defined spiral dye trace with suppression of the radial velocity perturbations. The magnetic field also effects reduction in scale of the lip-shed eddies.

Further evidence of the hydromagnetic stabilization effect is seen in Fig. 3.14, in which time-sequence exposures for $N_{Re\theta,0.8} = 1400$ are depicted ($N_{Ha} = 0$, upper; $N_{Ha} = 47$, lower). As a matter of fact, the field is effective in completely stabilizing the wall layer for Reynolds modulus up to ~4000 for this case. Figure 3.15 indicates that the stabilization effect is still significant in the interior at $N_{Re_\theta,0.8} = 4500$.

The effect of the magnetic field for the case of the vortex generated by injection through eight rows of 20-mil-diam round nozzles was studied

*Note that μ is also used (page 76) for the ratio of angular velocities of the outer and inner cylinders.

PHOTO 70586

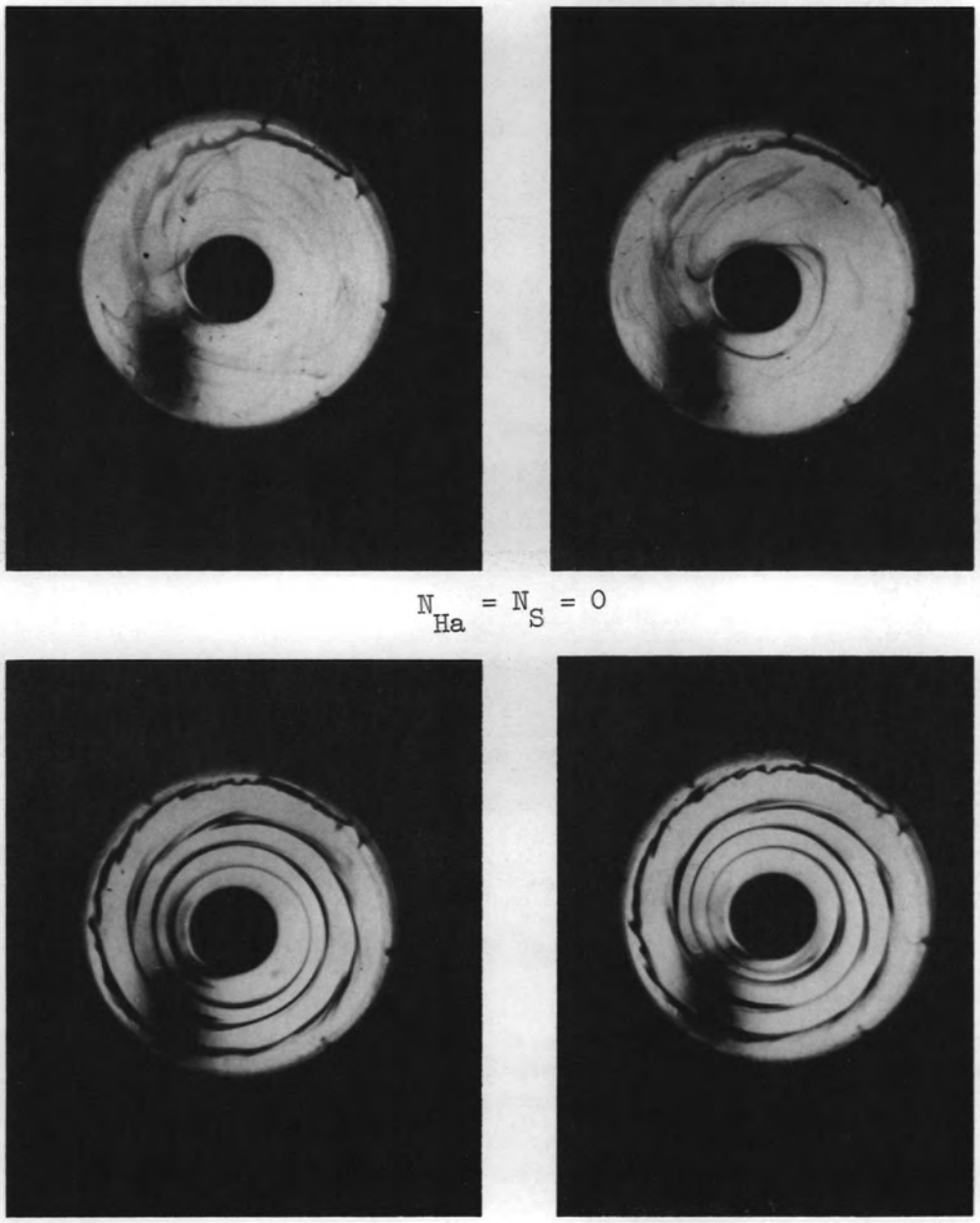

$N_{Ha} = N_S = 0$

$N_{Ha} = 47;\ N_S = 3.1$

Fig. 3.13. Dye Injection Traces — Nozzle-Fed Vortex Tube; $N_{Re_\theta, 0.8} = 700.$

PHOTO 70589

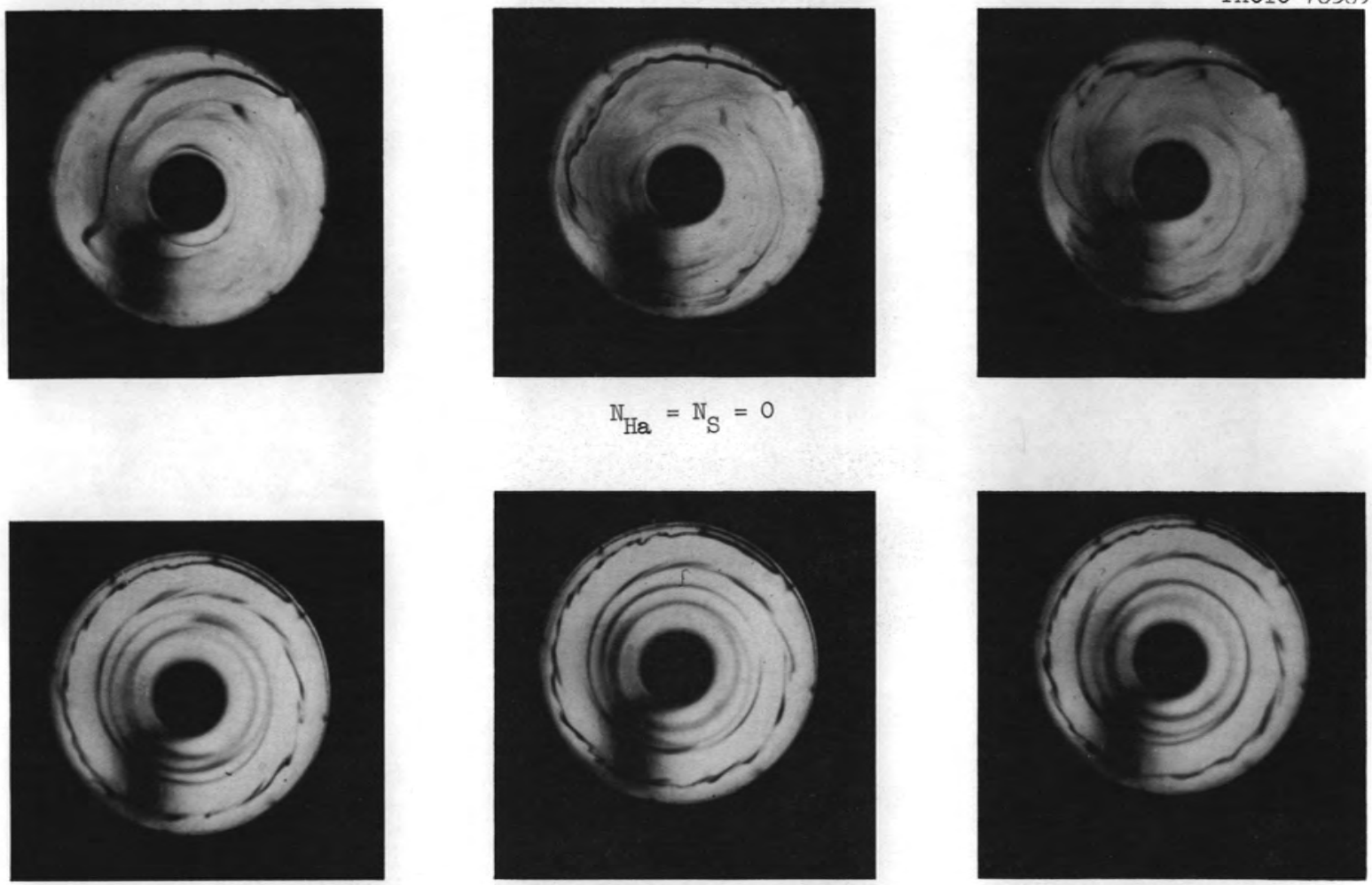

$N_{Ha} = N_S = 0$

$H_{Ha} = 47;\ N_S = 1.6$

Fig. 3.14. Dye Injection Traces — Nozzle-Fed Tube; $N_{Re_\theta, 0.8} = 1400$.

PHOTO 70587

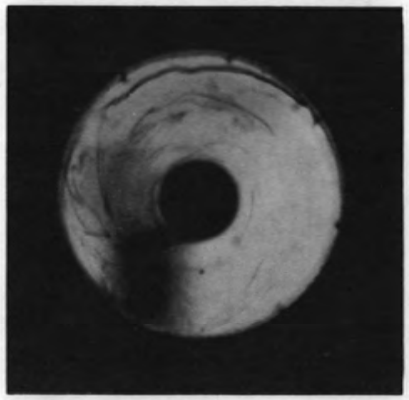

$N_{Ha} = N_S = 0$

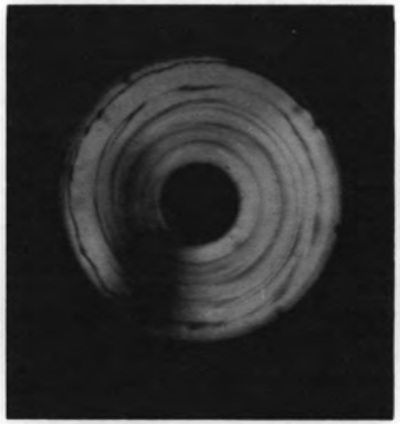

$N_{Ha} = 47;\ N_S = 0.48$

Fig. 3.15. Dye Injection Traces — Nozzle-Fed Vortex Tube; $N_{Re_{\theta},0.8} = 4500$.

by means of motion picture photography. For this case, the value of peripheral tangential Reynolds modulus observed at transition to instability in the boundary layer along the concave wall is ~500 with no applied magnetic field and ~1500 with the full magnetic field. The following observations are based on a detailed analysis of this film:

1. $N_{Re_\theta,0.8} = 400$: With no magnetic field ($N_{Ha} = 0$), evidence of a stable layer near the wall is observed with a definite instability detectable in the interior which may arise from nonaxisymmetric fluid injection. When a magnetic field of 74 kilogauss is applied ($N_{Ha} = 47$), the instability is eliminated completely with formation of a well-defined laminar spiral dye trace. Spreading of the dye trace in the jet-mixing zone near the wall is evident.

2. $N_{Re_\theta,0.8} = 860$, $N_{Ha} = 0$: Dye entering just downstream from a row of nozzles reveals the instability along the concave wall and the disordering of flow in the interior. Separation of the dye filament from the wall at the downstream row of jets leaves a residual trace which diffuses out of what is probably a recirculation region downstream from a nozzle. Disturbances which originate in the boundary layer-jet interaction zone seem to amplify in the interior into irregular vortex loops. It is also noted that the instability is a more or less periodic wave-like phenomenon, not typical random turbulence.

3. $N_{Re_\theta,0.8} = 1200$: With no applied magnetic field, oscillation of the dye trace near the wall is noted, inducing large-scale radial mixing in the interior. Both the amplitude and frequency of the disturbance are observed to increase with increasing $N_{Re_\theta,0.8}$ above the critical point. With the magnetic field applied, stable laminar ring structure with suppression of the local radially directed velocity perturbations is noted. There is no question as to the complete stabilization except in the core of the vortex where axial flow predominates.

4. $N_{Re_\theta,0.8} = 1950$: Without the field, there is evidence of a three dimensionality in the fully developed perturbations as indicated by the twisting motion of the dye which suggests that the origin of the instability may indeed be similar to that of the Taylor-Göertler instability.[35,37]

---

[37]H. Göertler, "Uber eine Dreidimensional Instabilität Laminaer Grenzchichten an Konkaven Wanden," Nachr. Wiss. Ges., Göttingen, Math. Phys. Klasse (New Series), 2, No. 1 (1940).

However, because of the strong radial and axial convection and the influence of the nonaxisymmetric jet driving sources, the steady secondary pattern of vortex cells does not appear, at least when viewed in two dimensions from a fixed frame of reference. The instability also appears to have certain characteristics of a jet influence separation phenomenon. Because of the complication in interpretation, a satisfactory explanation of the transition phenomenon has not been elucidated (see page 94). Since the Reynolds modulus is above the critical value (1500) with full magnetic field, the flow is no longer completely stabilized at $N_{Ha} = 47$. Partial stabilization is, however, evident by reduction in the scale of the internal eddy structure and hence reduction in the radial dispersion. A dampening effect of the field on small perturbations which originate near the wall is also evident; the field acts to prevent growth of these perturbations into full-scale disturbances.

5. $N_{Re_{\theta},0.8} = 3100$: Here the primary influence of the field is a strong reduction in the frequency of the observed flow oscillations near the concave wall and a moderate reduction in the amplitude of the disturbances in the interior of the flow field.

The effect of slowly decreasing Hartmann modulus (by decreasing B_0) from 47 to 0, at constant Reynolds modulus of 860, was investigated; and it was observed that the instability appears first in the interior, spreading outward as the magnetic field is further decreased to zero.

When the Hartmann modulus is slowly increased from 0 to 47, at constant Reynolds modulus of 860, the interior of the flow field stabilizes first. Migration of the dye trace toward the wall as the field is raised suggests a change in velocity profile in the wall layer which appears to be correlated with the stabilization effect.

Figure 3.16 compares the effect of the magnetic field on the jet velocity recovery ratio ($\alpha_{0.8}$) for four configurations of driving jets: 2-, 4-, and 8-plane slits, 8 rows of round nozzles. $\alpha_{0.8}$ is defined as the ratio of the tangential velocity at a radius of 0.8 r_2, to the injection velocity. The significant increase in $\alpha_{0.8}$ for 2- and 4-slit configurations is evident. No significant increase was observed for 8 slits or 8 rows of nozzles. This observation correlates with the fact that $Q_{r_2}/Q_{\theta,0.8}$ is about

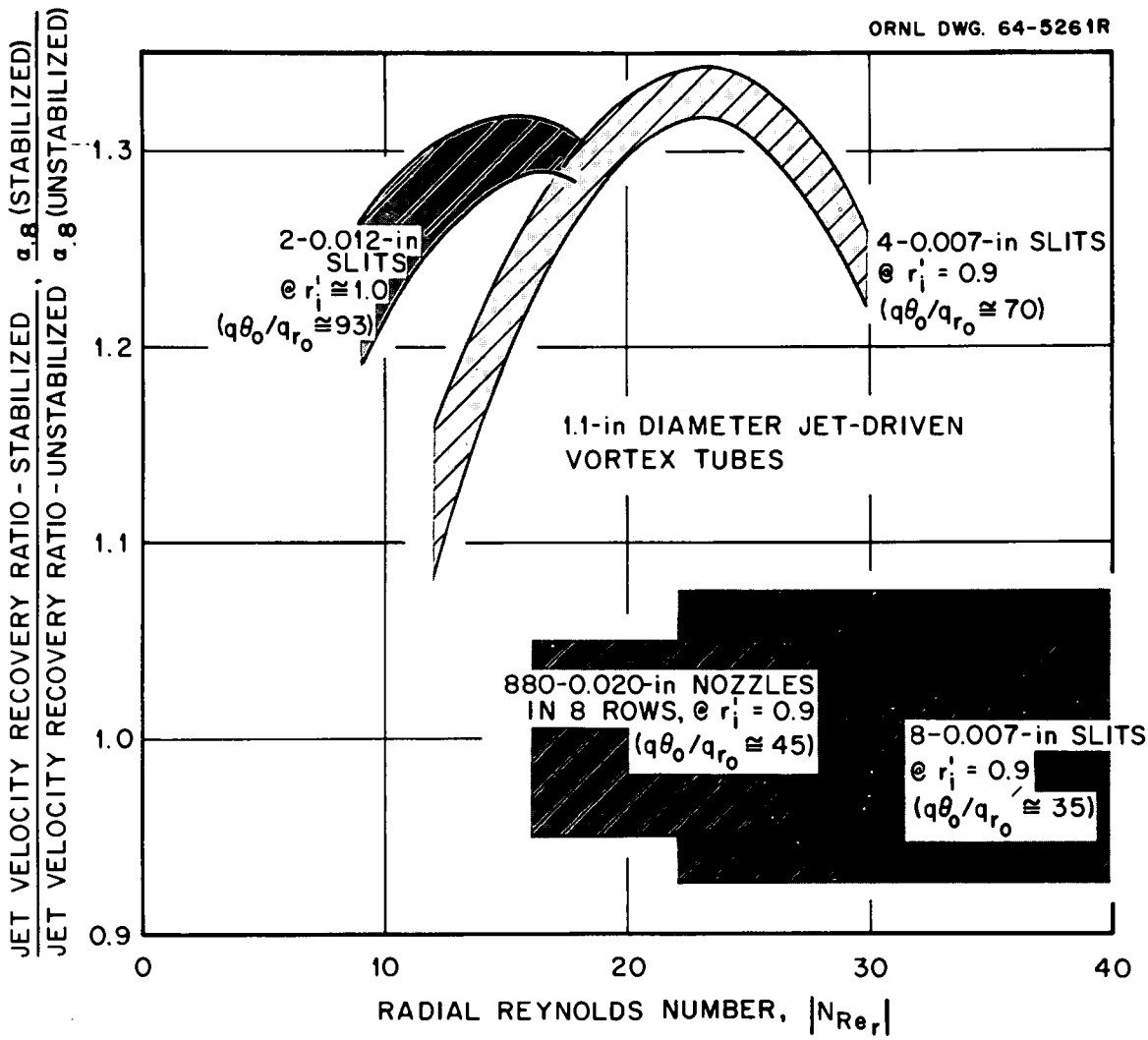

Fig. 3.16. Summary of the Effect of Hydromagnetic Stabilization.

twice as high for the latter cases where there appears to be no effect, suggesting that at least part of the effect of the field on α may be due to increase in radial flow in the interior due to suppression of the "short-circuit" flow on the end walls. The lower the $Q_{r_2}/Q_{\theta,0.8}$ ratio, the more significant this effect becomes.

Figure 3.17 summarizes quantitatively the experimental hydrodynamic stabilization results for vortex flows generated by 2-, 4-, and 8-slit injection, and by injection through 8 rows of round nozzles. In this correlation, the peripheral tangential Reynolds modulus at transition to instability along the concave wall, $N^*_{Re_{\theta},0.8}$, is plotted as a function of the square of the Hartmann modulus, N^2_{Ha}, obtained by variation in the magnetic field strength. For all but the 8-slit tube results, $N^*_{Re_{\theta},0.8}$ is seen to increase approximately linearly with N^2_{Ha} for $N^2_{Ha} > 600$. The results for 8 slits are anomalous in this respect. Note also that, with no magnetic field, $N^*_{Re_{\theta},0.8}$ is in the range from ~400 to ~950, while for the maximum magnetic field, $N^*_{Re_{\theta},0.8}$ varies from ~1600 to ~4000 depending on injection geometry. The graph thus suggests the influence of injection geometry, since the transition Reynolds modulus is observed to increase with increasing numbers of injection slits, at least at the higher values of N^2_{Ha}. This observation correlates with the growth of the wall boundary layer between slits. The round jet data, however, fall more nearly in line with the data for two tangential feed slits.

A comparison of the experimental hydromagnetic stabilization results with the numerical results for dissipative vortex-like flow (Cases VII and VIII, page 76 and 77) may be of some interest. It is important to bear in mind, however, that significant dissimilarities exist between the actual jet-driven vortex flow system and the idealized mathematical model. For example, the azimuthal variation in tangential velocity induced by the jets has not been considered, nor has the interaction of the jets with the concave boundary layer. The unperturbed flow has been assumed two dimensional, and furthermore the instability treated in the analysis is the transition to a stationary three-dimensional motion. In the experiment we see an "apparent" oscillatory, time <u>dependent</u>, perturbed state. Based on binocular microscopic observation (40X) through plastic end walls of a dye trace injected just downstream from one of the slits, it appears as though the

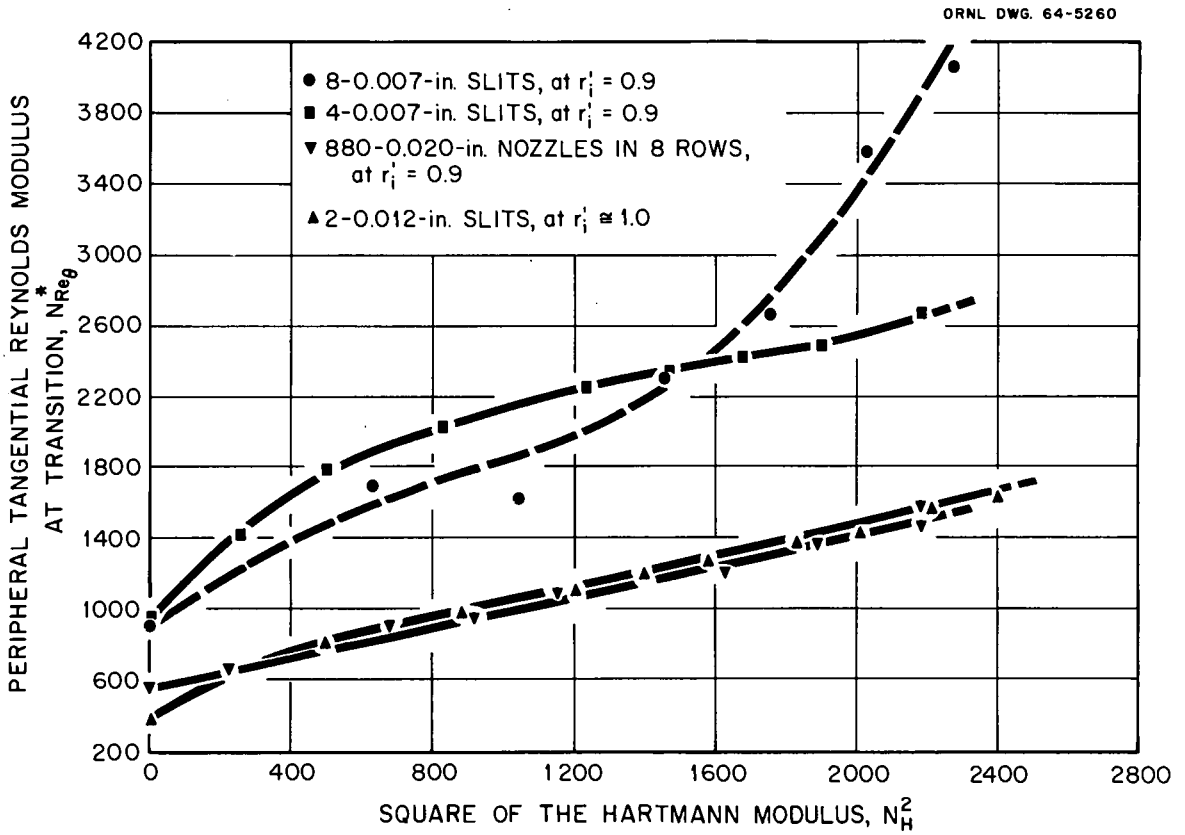

Fig. 3.17. Summary of Hydromagnetic Stabilization Experiments with 1.1-in.-diam Jet-Driven Vortex Tubes.

initial phase of transition may be an oscillatory two-dimensional expansion and contraction of the wall layer which may be associated with incipient separation of the decelerated jet flow. The fully developed instability, however, appears to be three dimensional in which the dye trace rotates in an irregular manner about a circumferential streamline. The oscillatory behavior of this phenomenon may be the result of convection of a stationary perturbed state with reference to the fixed point of observation, rather than a truly time-dependent fluctuation. If such is the case, the instability is probably of the stationary Taylor-Göertler type as assumed in the analysis. A transparent plastic model is in fabrication which will enable observation in both radial and axial directions to establish more conclusively the nature of the observed instability.

With these limitations in mind, consider the following comparison. Let the tangential flow in the vicinity of the stationary concave wall be generated by rotation of a hypothetical cylinder of radius, $r = \kappa\, r_2$, with respect to a fixed outer cylinder, so that $\mu = 0$. Three special cases have been considered analytically:

1. $N_{Re_r} = 0$ (no radial flow — Case VII)

   $\kappa = 0.8$ (corresponding to what may be a typical boundary-layer thickness)

2. $N_{Re_r} > 0$ (outward radial flow — Case VIII)

   $\kappa = 0.25$ (corresponding nearly to the actual outlet radius)

3. $N_{Re_r} > 0$, RRC = 0

   $\kappa = 0.25$, but the convective terms involving N_{Re_r} directly are eliminated in the equations of motion (RRC = 0)

There is a certain artificiality in each of these cases:

1. The velocity profile for this case does not look much like a boundary-layer profile.

2. The actual radial flow is inward on the average. Use of outward radial flow in the calculations gives a more nearly correct velocity profile, however.

3. Here we have removed the convective contribution of radial flow but retained the desired velocity profile — hence, in this case, N_{Re_r} can be considered as a shape factor governing the velocity profile only.

These three cases are plotted in Fig. 3.18 and compared with the experimental results for two slits (tangential entry). N_{Re_r} has been adjusted in the upper two curves to give an intersection with the experimental results at low N_{Ha}^2. The curve for $\kappa = 0.8$, $N_{Re_r} = 0$ exhibits approximately the same linear slope as the data, the $\kappa = 0.25$, $N_{Re_r} = 17.8$ curve is slightly steeper than the data, and the $\kappa = 0.25$, $N_{Re_r} = 31.6$ (RRC = 0) curve exhibits appreciably more curvature than the experimental results. Keeping in mind the possible dissimilarities between the experimental jet-driven vortex flow situation and the analysis plus the fact that two adjustable parameters are employed, any apparent agreement over such a limited range could be fortuitious.

A 4-in.-diam stainless steel vortex tube model is in fabrication which will employ four tangential slits for vortex generation and which will enable operation at values of N_{Ha}^2 of up to about 32×10^4, or a factor of 13 higher than possible using the present 1.1-in.-diam tubes. The new model will be used to study the hydromagnetic stabilization effect in the boundary layers in the flat end walls as well as on the concave cylindrical wall. It is intended to investigate in particular the effect of the field on the undesirable short-circuiting end-wall flow discussed in ref. 38 and in the following Section 3.2.

---

[38]W. S. Lewellen and W. S. King, "Boundary-Layer Similarity Solutions for Rotating Flows with and Without Magnetic Interaction," Report No. ATN-63(9227)-6, Aerospace Corporation, July 1963.

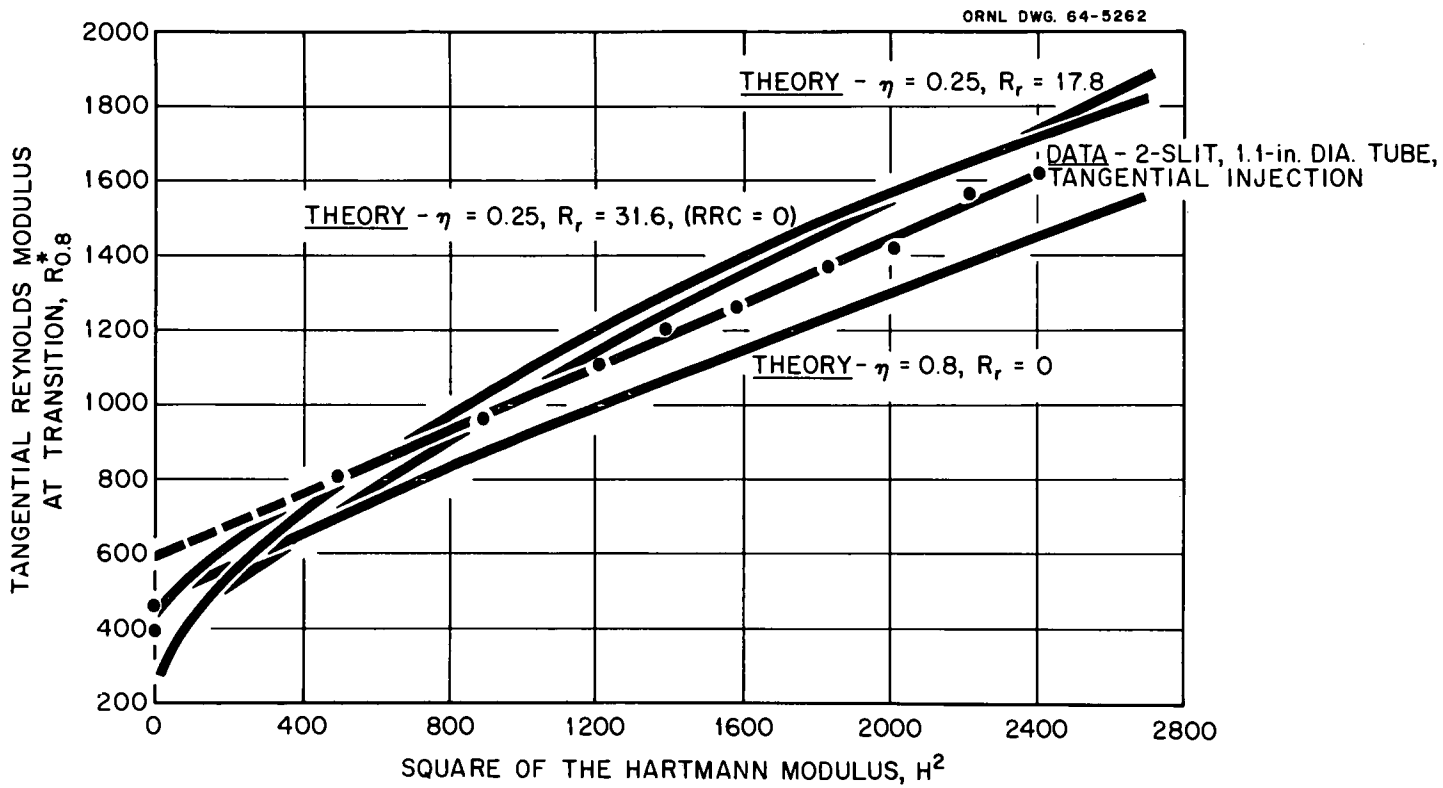

Fig. 3.18. Comparison of Chang-Sartory Theory with Experimental Results.

3.2. Potential Vortex Flow Near a Stationary Disk

G. J. Kidd, Jr.

In the design and operation of confined vortex systems, the flow in the boundary layers on the stationary surfaces is not satisfactorily understood at present. In jet-driven vortexes of the type proposed for certain advanced energy-conversion applications, this flow amounts to a significant fraction of the total for the system. To aid in understanding this phenomenon, a study is being initiated in which the interaction between a vortical flow and a stationary disk, perpendicular to the axis of the vortex, will be examined. A two-dimensional swirling flow closely approximating a potential vortex* can be generated experimentally by passing water radially inward through a rotating drum made of expanded aluminum honeycomb and exhausting it through a small porous tube at the axis (Fig. 3.19). Several previous analytical and experimental studies[39-41] have shown that for cases where the inward flow per unit length is small compared to the circulation, i.e.,

$$2 \pi K_2 \frac{1}{L} q_r \ll 2 \pi K ,$$

the tangential velocity in the free stream is given by:

$$q_\theta = \frac{c_1}{r} + c_2 r^n ,$$

*The free stream in a jet-driven vortex chamber is essentially a potential vortex; the potential vortex is one in which angular momentum per unit mass is conserved so that the tangential velocity varies inversely with the radius; i.e., $q_\theta = K r$, where q_θ is the tangential velocity, $2 \pi K$ is the circulation, and r is the radius.

[39]H. A. Einstein and H. Li, "Steady Vortex Flow in a Real Fluid," Proceedings of the 1951 Heat Transfer and Fluid Mechanics Institute, p. 33, Stanford University Press, Stanford, California, 1951.

[40]W. S. Lewellen, "A Solution for Three-Dimensional Vortex Flows with Strong Circulation," J. Fluid Mech., 14(3): 420 (1962).

[41]C. duP. Donaldson and R. D. Sullivan, "Behavior of Solutions of the Navier-Stokes Equations for a Complete Class of Three-Dimensional Viscous Vortices," Proceedings of the 1960 Heat Transfer and Fluid Mechanics Institute, p. 16, Stanford University Press, Stanford, California, 1960.

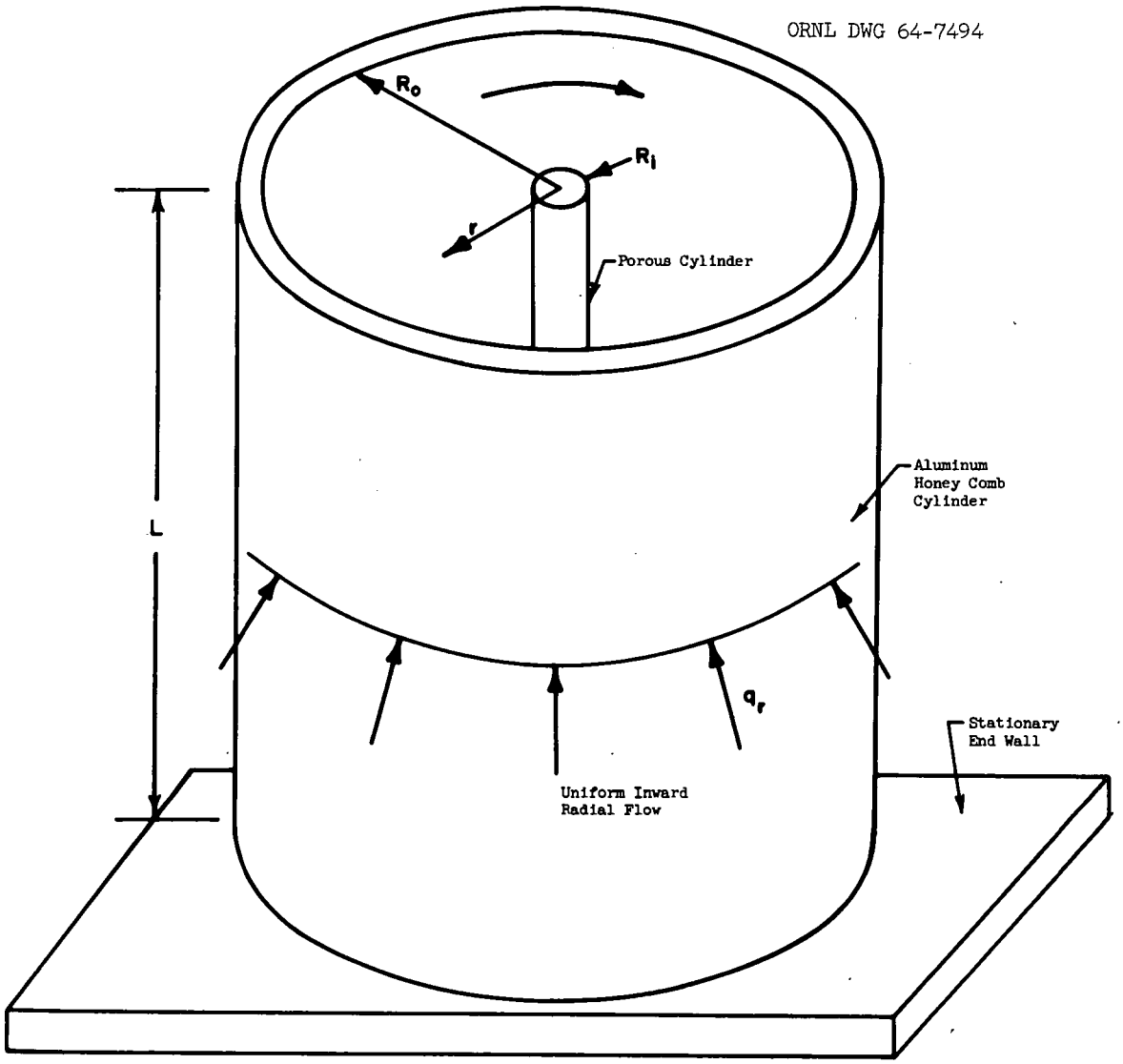

Fig. 3.19. Vortex Generator.

in which c_1 and c_2 depend on boundary conditions and n depends on the magnitude of the radial flow and is negative for inward flow. Since large values of n occur at very small radial flows, the potential vortex is easily approximated experimentally. By establishing the free stream flow in this way, it will be possible to study the boundary layer over a wide range of tangential Reynolds moduli:

$$N_{Re_\theta} = \frac{K}{\nu} ,$$

since K can be varied by simply changing the angular speed of the revolving drum.

The actual flow in the boundary layer will be studied using a number of dye tracer techniques,[42,43] the tellerium tracer technique,[44] and an electrochemiluminescent boundary-layer visualization technique.[45]

A theoretical study of the boundary-layer flow is being made by attempting to integrate the axisymmetric boundary-layer equations for the tangential and radial velocities simultaneously on an analog computer. An approach similar to that of Schwiderski and Lugt[46] will be used in which the usual boundary-layer simplification of dropping terms involving $\partial^2/\partial Z^2$ is not made, but rather all terms are included.

---

[42]Symposium on Flow Visualization, ASME Annual Meeting, Nov. 30, 1960.

[43]W. J. Rainbird, R. S. Crabbe, and L. S. Jurewicz, "A Water Tunnel Investigation of the Flow Separation about Circular Cones at Incidence," Aeronautical Report LR-385, National Research Council of Canada, September 1963.

[44]F. X. Wortman, "A Method for the Observation and Measurement of Water Flow with Tellerium," Zeitschrift für angewandte Physik, 5(6): 201 (June 1953).

[45]B. Howland, W. H. Pitts, and R. C. Gesteland, "Use of Electrochemiluninescense for Visualizing Fields of Flow," MIT Tech. Report 404, Massachusetts Institute of Technology, September 21, 1962.

[46]E. W. Schwiderski and H. Lugt, "Boundary Layer Along a Flat Surface Normal to a Vortex Flow," NWL-1835, Naval Weapons Laboratory, Dahlgren, Virginia, December 20, 1962.

3.3. Boundary-Layer Transient Phenomena

G. J. Kidd, Jr.

Fabrication of the new solid stainless steel test section incorporating brazed-in heaters, described previously,[47] has proceeded to the final stage: the formation of the junctions on the 16 gunbarrel thermocouples. During this reporting period, the gunbarrel thermocouples, along with other special wall surface temperature probes and heat flux meters, have been installed in the stainless steel body of the test section. In order to achieve good thermal contact between the probes and the body of the heater, it was necessary to hand fit each one into a taper-reamed hole. Once the probes were all fitted they were driven home and the portions extending into the flow channel were ground-off flush with the wall. The entire test section was then honed to a 4-μin. rms finish

The next and final step is the plating of a thin-nickel film over the inside ends of the gunbarrel thermocouples to form the hot junctions. It is desired that this be accomplished by a standard vacuum deposition technique. However, despite the fact that the same technique was used as on the previous two similar test sections,[48,49] it has not been possible thus far to effect a satisfactory junction. The problem appears to be an accumulation of honing oil in the ceramic insulator of the thermocouples which boils out and contaminates the section when the plating electrodes are heated under vacuum. Attempts are being made to remove this oil and/or to find an alternative means of plating the interior of the test section. Figure 3.20 is a photograph of the new test section preparatory to the

[47]H. W. Hoffman and J. J. Keyes, Jr., "Studies in Heat Transfer and Fluid Mechanics Progress Report for Period Jan. 1 – Sept. 30, 1963," USAEC Report ORNL-TM-915, pp. 86–96, Oak Ridge National Laboratory, October 1964.

[48]A. E. Higinbotham, T. J. Delaney, J. E. Danahue, and M. J. Friedman, "Study of Unsteady Heat Transfer Between a Surface and a Flowing Fluid," USAEC Report KT-397, MIT Practice School, Oak Ridge Gaseous Diffusion Plant, May 11, 1959.

[49]J. E. O'Connel, S. M. Fleming, and R. M. Roth, "Study of Unsteady Heat Transfer Between a Surface and a Liquid in Turbulent Flow," USAEC Report KT-566, MIT Practice School, Oak Ridge Gaseous Diffusion Plant, March 4, 1961.

PHOTO 66342

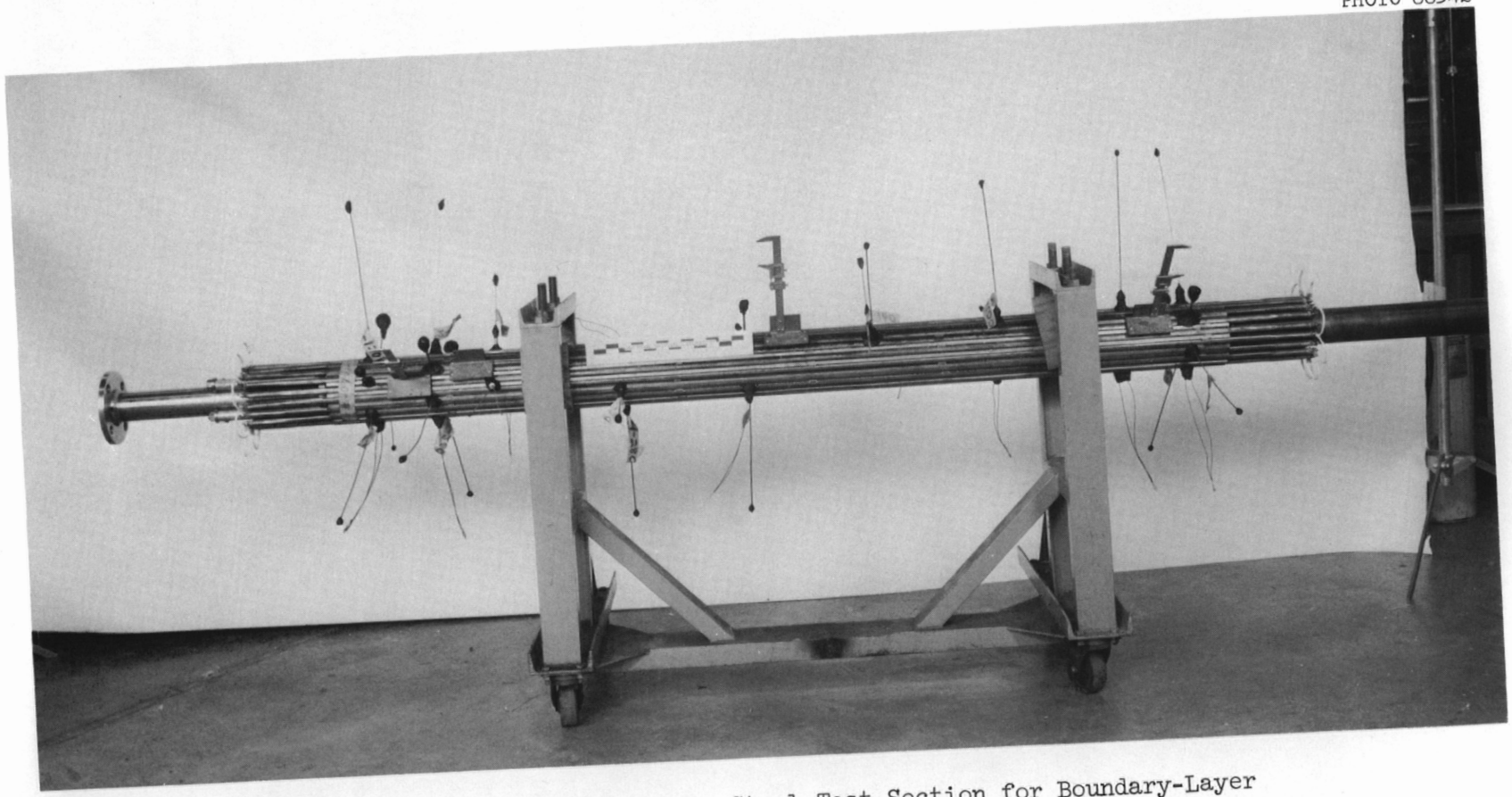

Fig. 3.20. Solid Stainless Steel Test Section for Boundary-Layer Transient Studies.

vacuum plating step.

Techniques for fabricating reliable, long-lived hot-film surface probes for the measurement of local, instantaneous heat-transfer rate and coefficient of heat transfer have been perfected. A number of probes have been made and are being evaluated for ease of forming the thin film, endurance, dimensional stability, etc. A new test section containing four of these probes and a hot-film anemometer in a chrome-plated brass tube is in fabrication.

Recent measurements have been made of the instantaneous local water film heat-transfer coefficient inside a 2-in.-diam pipe containing one hot-film probe. The results are shown in Fig. 3.21. The probe formed one leg of a constant temperature hot-film anemometer bridge. The mean voltage across that leg of the bridge is shown in the left-hand column of the figure and averaged about 3.3 volts; the maximum fluctuations were of the order of 200 mv (0.2 volts) peak to peak. Since the heat-transfer coefficient is directly proportional to the voltage in this circuit, the percentage fluctuation in heat-transfer coefficient about the mean was:

$$\frac{h'}{\bar{h}} = \frac{\pm 0.2}{3.3} \times 100 = \pm 6\%.^{*}$$

The data show a definite laminar behavior for Reynolds moduli below 2600 and a change to turbulent flow with a characteristic period of intermittency flow in between. Data for a Reynolds modulus of 17,000 was then analyzed manually to find the distribution in amplitude of the fluctuations as a function of the frequency, and the results are presented in Fig. 3.22. Some of the scatter is due to the technique used in evaluating the data; however, the curves do indicate a trend in the amplitude-frequency spectrum. These data, which represent the average values of the amplitudes, show that the largest amplitudes occur at the low end of the frequency spectrum. There were, of course, occasional fluctuations much greater than the average, in some cases as much as three times the average value.

---

*For small fluctuations in heat-transfer coefficient about the mean value, the conversion from voltage to power introduces a factor of 2 in in this relationship.

ORNL DWG 63-7866

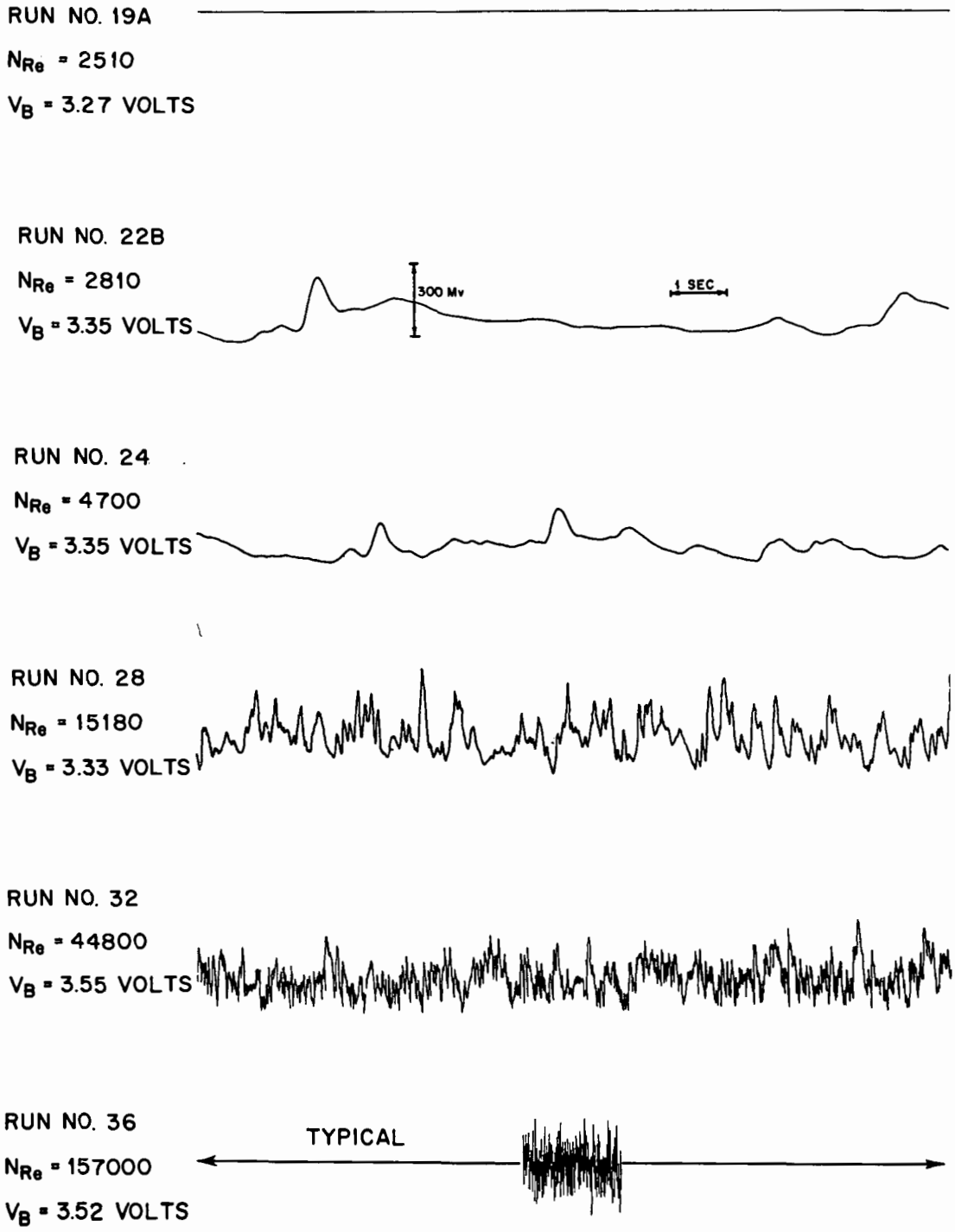

Fig. 3.21. Time-Dependent Fluctuations of Local Water Film Heat-Transfer Coefficient Inside a 2-in.-ID Pipe.

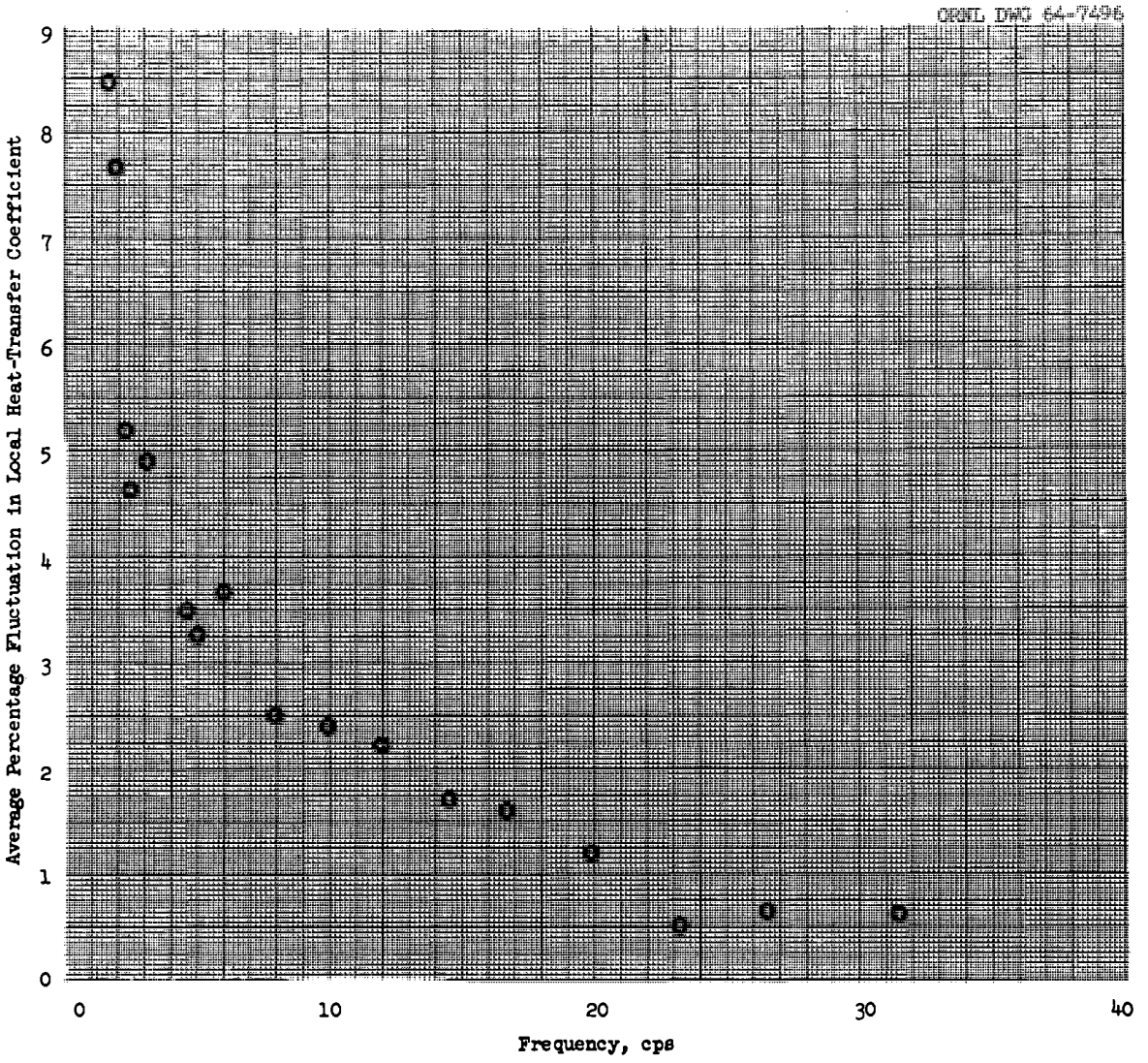

Fig. 3.22. Spectrum of the Fluctuations in Local Water Film Heat-Transfer Coefficient Observed at N_{Re} = 17,000 Inside a 2-in.-ID Pipe.

A Panoramic Subsonic Spectrum Analyzer is available to reduce the data automatically and methods for calibrating this instrument so it can produce quantitative results are now being devised.

A further analysis of the data was made in terms of the power spectral density (PSD), which relates the energy-per-unit frequency to the frequency of the fluctuations. This analysis was performed on a PACE TR 10 Analog Computer. Figure 3.23 presents the results of this analysis. At low Reynolds modulus, most of the energy is contained in the low-frequency fluctuations while at higher Reynolds modulus there can be a significant contribution to the energy at the very high frequencies. This energy-frequency relationship is important in the analysis of the thermal-cycling fatigue problem in reactor systems.

The latest series of runs have been designed to measure the correlation coefficient between the fluctuation, q', in the axial velocity near the wall and the fluctuation, h', in the heat-transfer coefficient as a function of Reynolds modulus. The correlation coefficient is defined by the equation:

$$R \equiv \frac{q' \; h'}{\sqrt{\overline{q'^2}} \; \sqrt{\overline{h'^2}}} \; .$$

The experiments were carried out in the same test section used previously with the addition of a hot-wire anemometer to measure the velocity near the wall. This data is being analyzed on the TR 10; however, the analysis has not reached the point where it can be interpreted quantitativley.

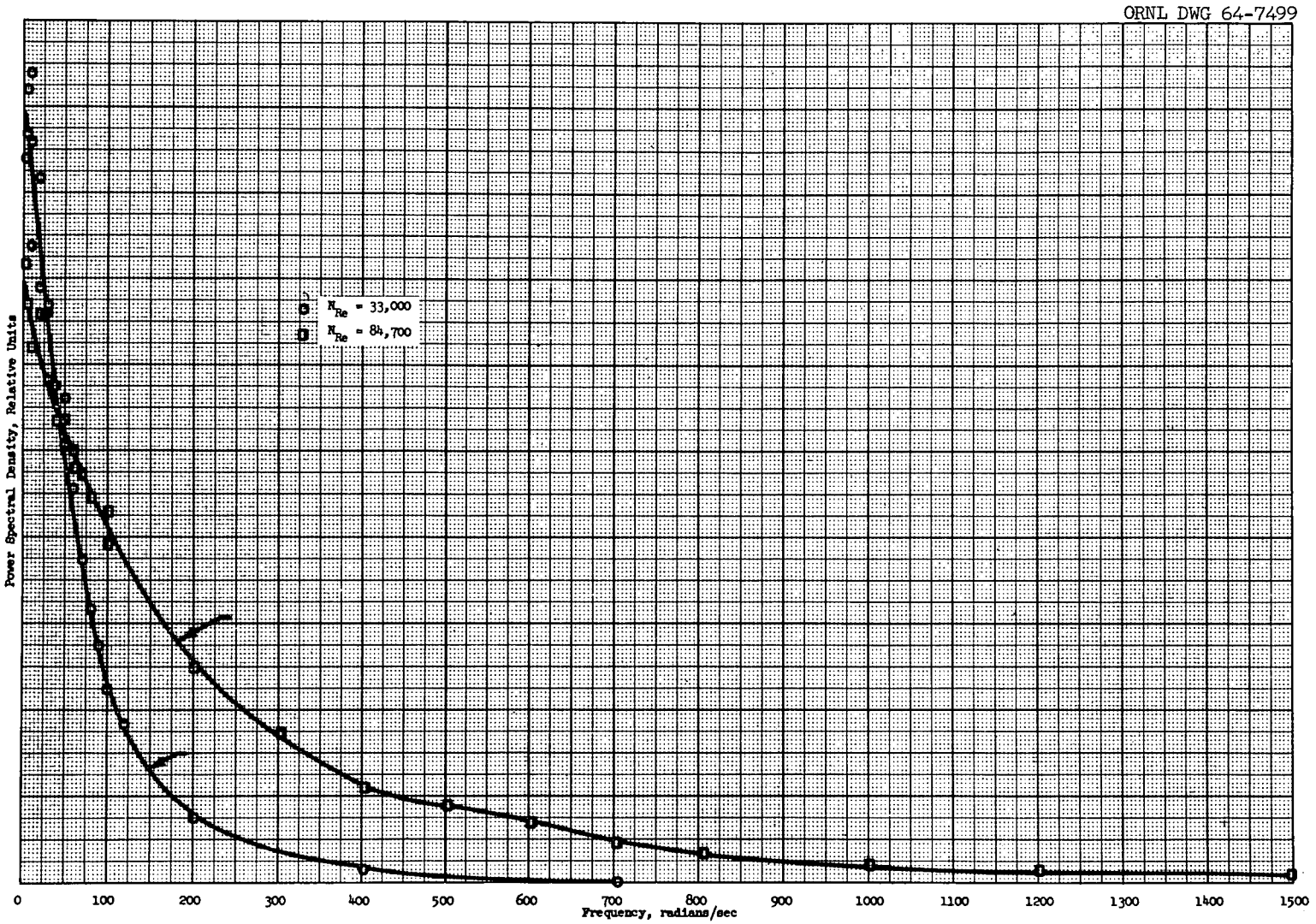

Fig. 3.23. Power Spectral Density of Fluctuations in Local Heat-Transfer Coefficient Inside a 2-in.-ID Pipe.

3.4. Turbulent Transport Studies

R. P. Wichner

It was reported previously[50] that preliminary data on the turbulence level in water at a Reynolds modulus of 158,000 as obtained in this study fell below published values which exist for air flows only.[51] To resolve this discrepancy, an air flow facility was assembled; a photograph of the apparatus is shown in Fig. 3.24. The test section, composed of two 21-ft lengths of 8-in. pipe, formed the suction line of the blower. Air was admitted through the filter box made up of fourteen 20-in. × 25-in. × 2-in.-wide Fiberglas air filter elements (shown at the extreme left of Fig. 3.24) into an inlet diffuser (to conserve pressure drop) containing straightening vanes and a wire screen. The wire screen flattened the inlet flow profile to conform more nearly with the fully developed profile, thereby reducing the required ℓ/d's to achieve fully developed pipe flow. The flow rate was varied by changing the diameter of the orifice on the blower outlet. Pressure measurements, from which wall shear stress and velocity profile values are derived, were made by means of an RGI Model G-1500 micromanometer capable of resolving a pressure difference of 0.001 in. of water.

In order to take advantage of the lower form drag in air flows (compared with water), new hot-wire probes were fabricated with thinner and longer wire supports. These supports should interfere less with the flow and, hence, have less influence on the measured turbulence properties. In addition, methods were developed for handling and mounting the very fine tungsten wires (0.00012-in. to 0.00016-in. diameter) required for air hot-wire anemometry. These wires are barely visible against the light background in the photograph of these probes shown in Figs. 3.25 and 3.26. The probes in Fig. 3.25 are designed to enter the flow stream in an approximately radial direction, while the one in Fig. 3.26 is designed to face directly into the flow.

---

[50] H. W. Hoffman and J. J. Keyes, Jr., "Studies in Heat Transfer and Fluid Mechanics Progress Report for Period Jan. 1 – Sept. 30, 1963," USAEC Report ORNL-TM-915, Oak Ridge National Laboratory, October 1964.

[51] J. Laufer, "The Structure of Turbulence in Fully Developed Pipe Flow," Nat. Adv. Com. on Aero. Report -1174, 1954.

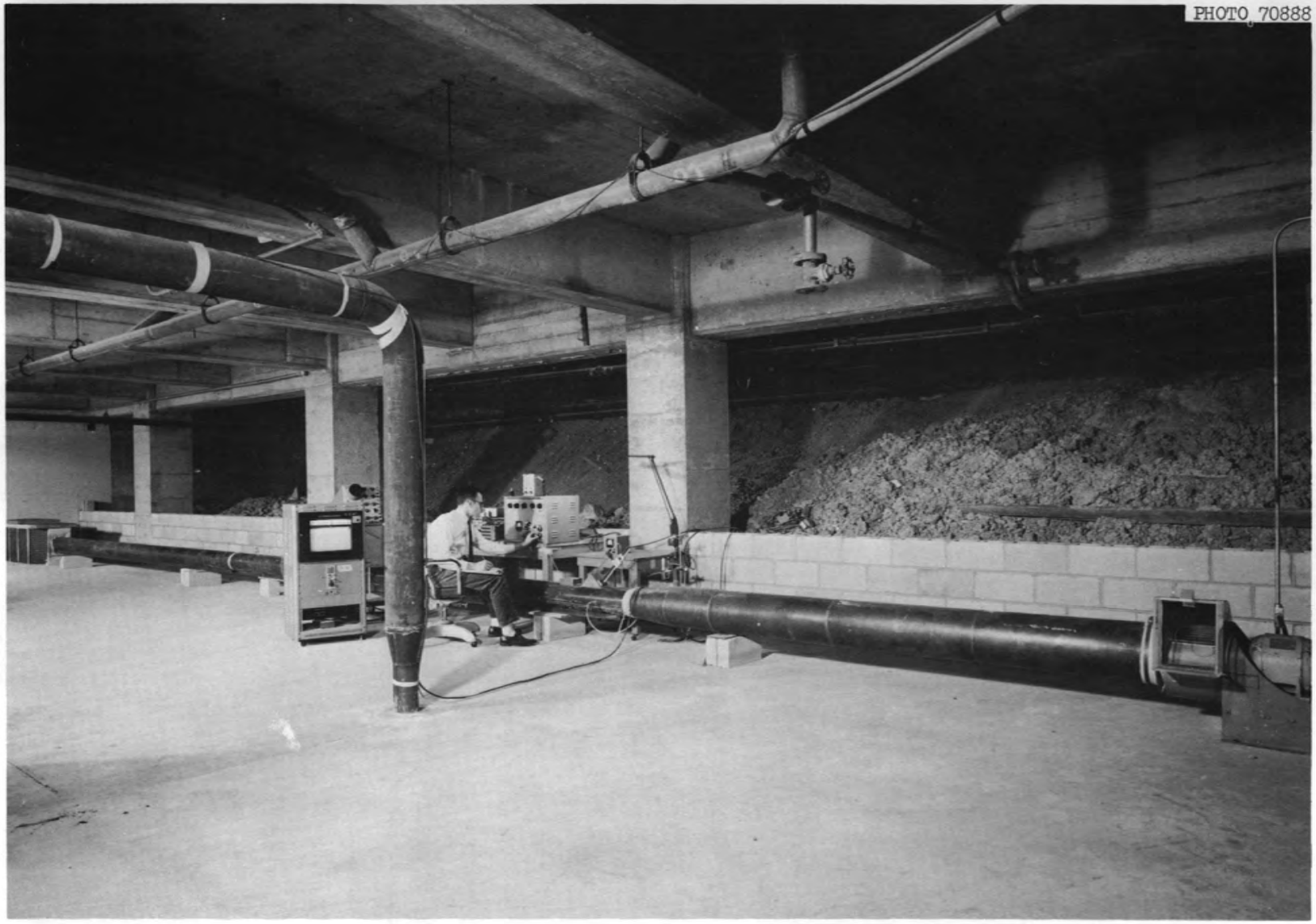

Fig. 3.24. Reynolds Stress Air Flow Facility.

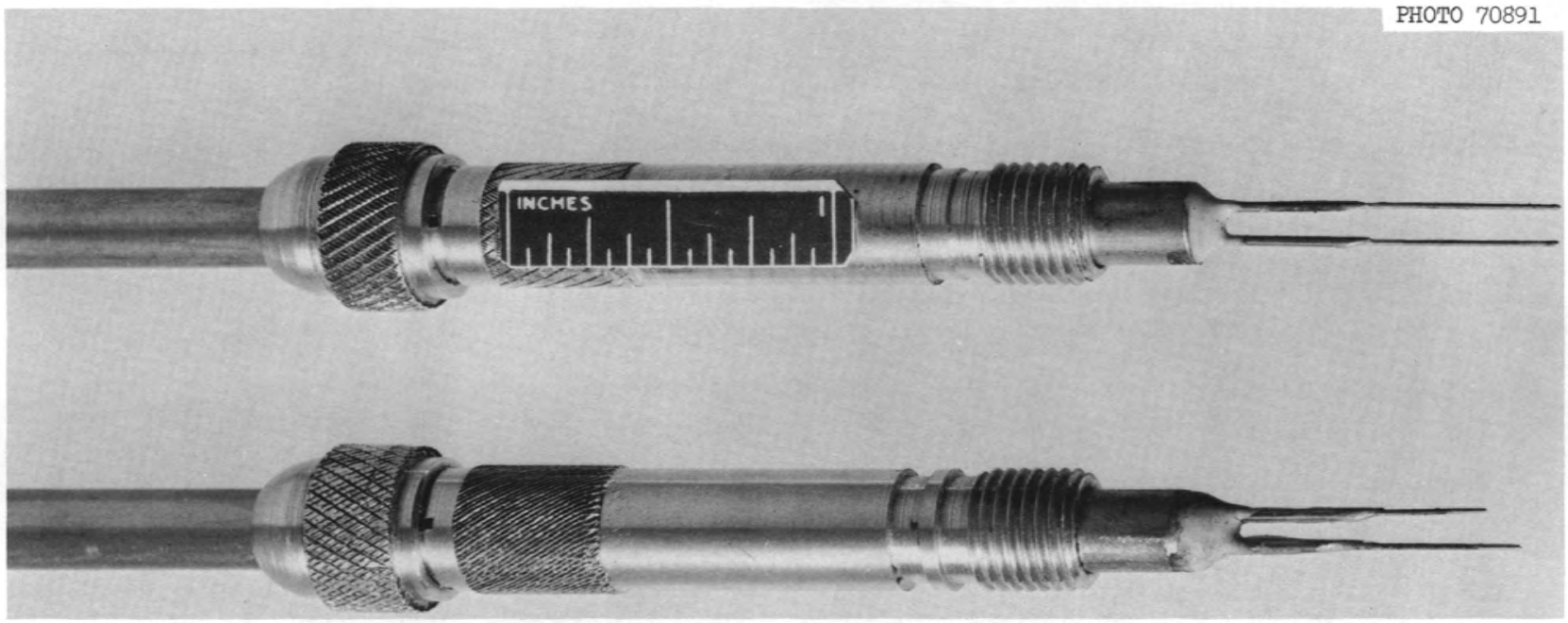

Fig. 3.25. Hot-Wire Probes with 0.00016-in.-diam Tungsten Wire.

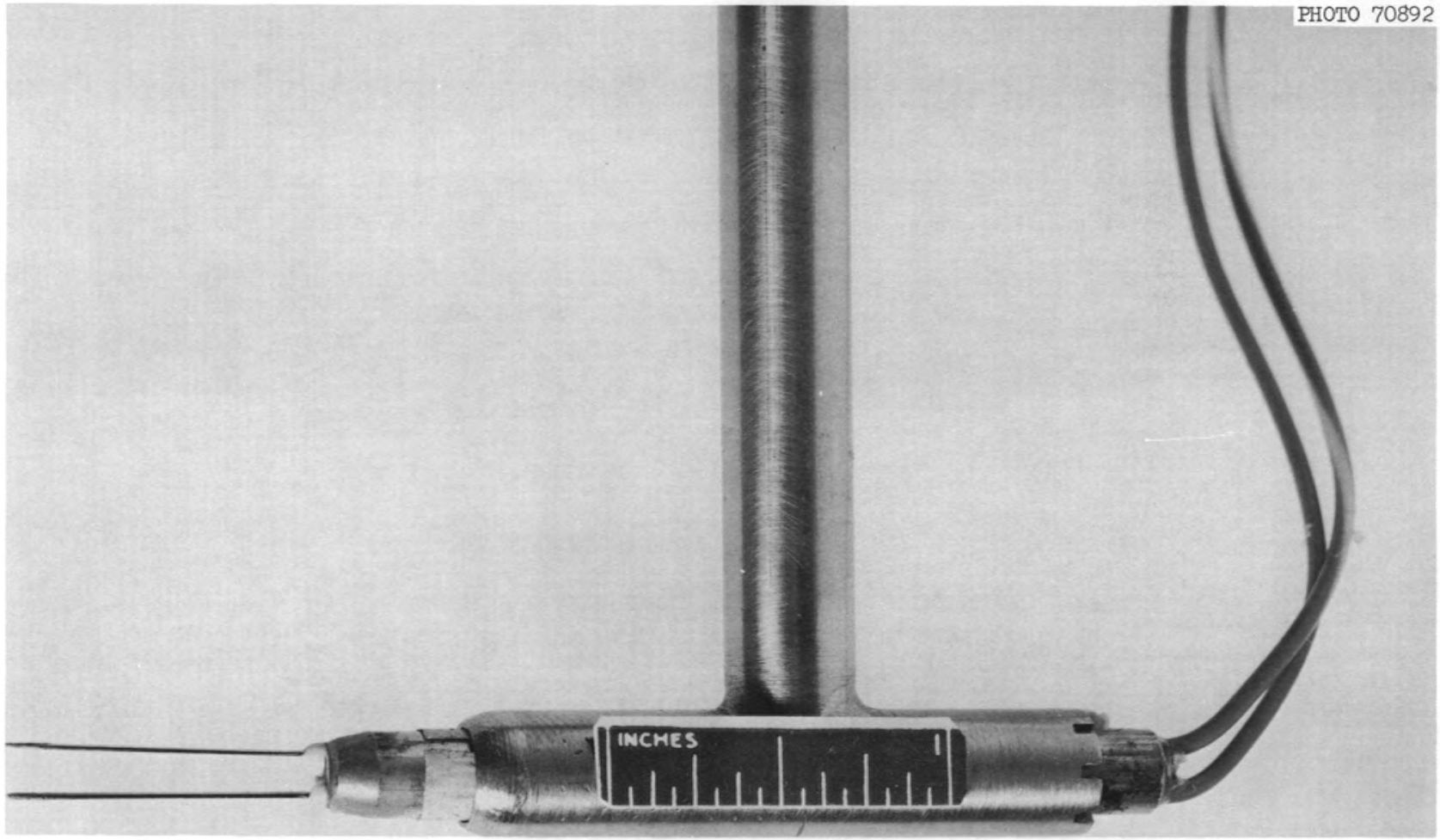

Fig. 3.26. Hot-Wire Probe for Axial Orientation to Flow.

The air Reynolds stress data taken to date has not yet been fully analyzed. These results, along with the eariler data with water, will be discussed in detail in a subsequent report.

4. THERMOPHYSICAL PROPERTIES

4.1. Alkali Liquid Metals

J. W. Cooke

4.1.1. Surface Tension of Potassium

The preliminary results reported previously[52] for the surface tension (relative to helium) of 99.96 wt % potassium have been extended to temperatures near the boiling point. A total of 202 separate determinations were made in the temperature range 70 to 713°C using a maximum-bubble pressure apparatus. All measurements were carried out at atmospheric pressure; data were obtained under both increasing and decreasing temperature conditions. Inconel capillary tubes of four different sizes (inside diameter between 1.54 and 1.66 mm) were used with two potassium samples. The contaminant concentration in these samples (before and after use) is given in Table 4.1.

The surface tension was calculated using the Rayleigh-Schroedinger equation;[53,54] the final results are plotted in Fig. 4.1 and compared with data reported by other investigators. The surface tension (in dynes/cm) may be described, in the temperature span between 70 and 710°C, by the least-squares derived equation,

$$\sigma = 115.36 - 0.0646\ t \quad , \tag{4.1}$$

with a mean-square deviation of ±0.72 dynes/cm. Several surface tension values around 200°C were as much as 5% below the average data and were not included in the least-squares analysis. All of these lower values were recorded within 10 to 20 minutes after a new capillary tube has been installed. Thus, it is possible that these lower values resulted from poor wetting of the capillary tube by the potassium.

---

[52]J. W. Cooke, Thermophysical Properties of Liquid Metals, pp. 116–121, "Space Power Program Seniann. Prog. Rep. June 30, 1963," USAEC Report ORNL-3489.

[53]Lord Rayleigh, "On the Theory of the Capillary Tube," Proc. Royal Soc., Sec A, 92: 184–195 (1915).

[54]E. Schroedinger, "Note on the Capillary Presure in Gas Bubbles," Ann. Physik, 46: 413 (1915).

Table 4.1. Spectrochemical Analysis of Potassium Sample Nos. 1 and 2 Before and After Surface Tension Determinations

Element	Sample Nos. 1 & 2 Before, ppm	Sample No. 1 After, ppm	Sample No. 2 After, ppm
Oxygen	26; 35	–	27; 117
Iron	<5	3.3	133; 210
Chromium	<1	<1	58; 80
Nickel	6.7	2.2	5
Lithium	<1	<1	–
Sodium	60[a]	110[b]	–
Rubidium	132	47	–
Cesium	20	22	–
Aluminum	<10	<10	–
Magnesium	<2	<2	–
Copper	<1	–	–
Cobalt	<5	<5	–
Calcium	11	3	–
Molybdenum	<3	–	–
Boron	10	–	–
Lead	<5	–	–
Titanium	<5	–	–
Silver	<1	–	–
Zirconium	<10	–	–
Potassium (by difference)		99.97 wt %	99.93%

[a]Sample taken in polyethylene bottle.

[b]Sample taken in glass bottle.

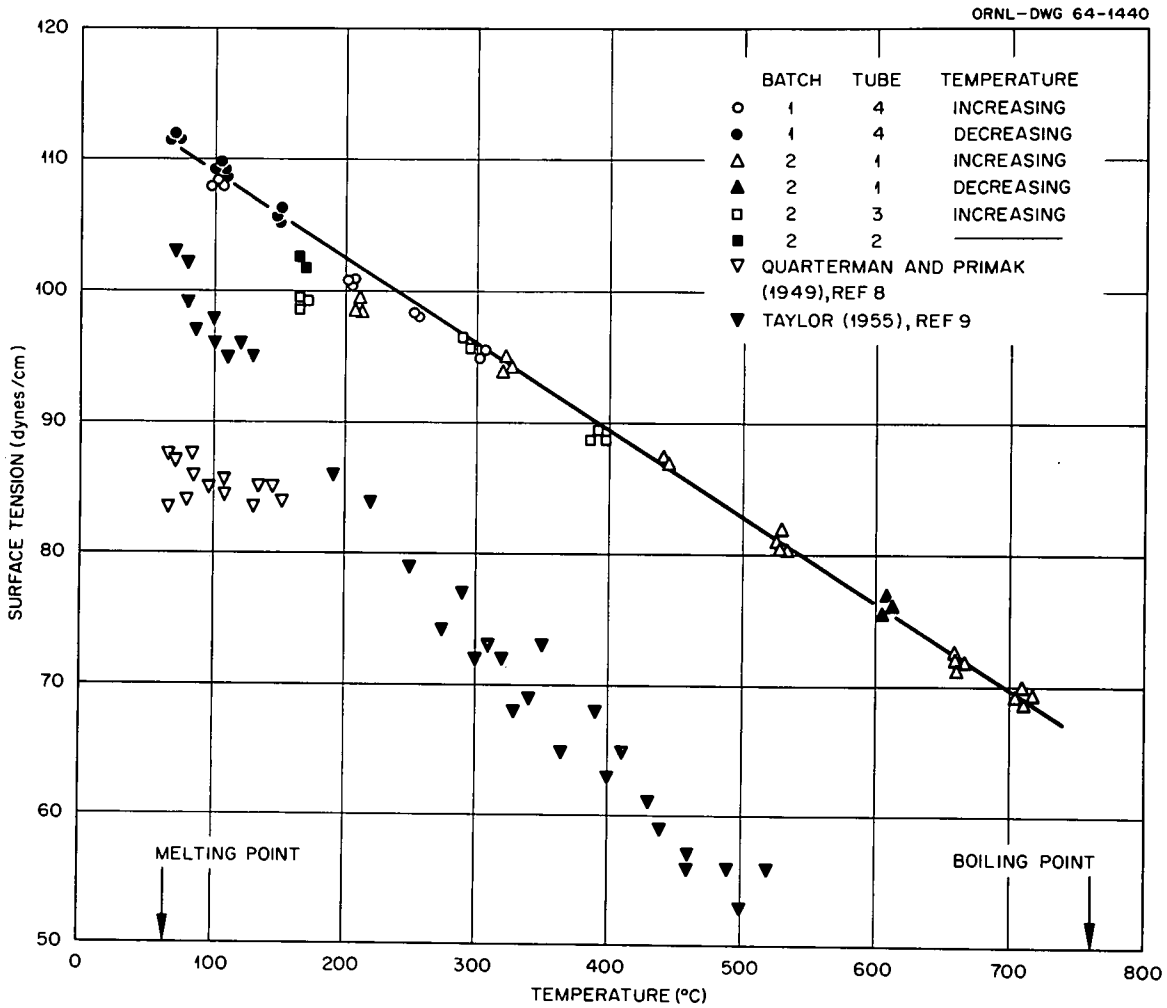

Fig. 4.1. Surface Tension of Molten Potassium as a Function of Temperature.

Figure 4.1 also shows earlier data on potassium obtained by Quarterman and Primak[55] (1949) and by Taylor[56] (1955); both sets of results fall significantly below the values found in the current investigation. Quarterman and Primak used a capillary rise technique to obtain the surface tension over the narrow temperature range between the melting point and 150°C; their results were ~20% below the values reported here. These investigators indicate that their data may be low by as much as 15% due to a possible contact angle between the potassium and their glass capillary tube and to difficulties in measuring the capillary height between the two concave menisci.

Taylor also used a maximum bubble-pressure technique but noted difficulties in establishing the peak pressure due to fluctuating manometer readings; these results lie between 9% (at 75°C) and 35% (at 500°C) below the present data. The extent of cesium and rubidium impurities in the potassium (contaminants most likely to affect the surface tension) were not reported by Taylor.

4.1.2. Density of Potassium

Data on the maximum bubble pressure at various depths of capillary immersion have been used to calculate the density of liquid potassium. The results are shown in Fig. 4.2; comparison is made with a composite of data from three investigations as reported by Lyon.[57] The agreement is quite good, with the present values averaging about 0.4% higher.

4.1.3. Contact-Angle Determinations

Determination of the contact angle between a potassium droplet and various horizontal supporting surfaces have been continued using the

---

[55]L. A. Quarterman and W. L. Primak, "The Capillary Rise, Contact Angle, and Surface Tension of Potassium," J. Am. Chem. Soc., 72: 3035 (1950).

[56]J. W. Taylor, "The Surface Energies of the Alkali Metals," British Atomic Energy Authority Report AERE M/R 1620, Feb. 22, 1955.

[57]R. N. Lyon, ed., Liquid Metals Handbook, 2nd ed., p. 42, U. S. Government Printing Office, Washington, D. C., 1952.

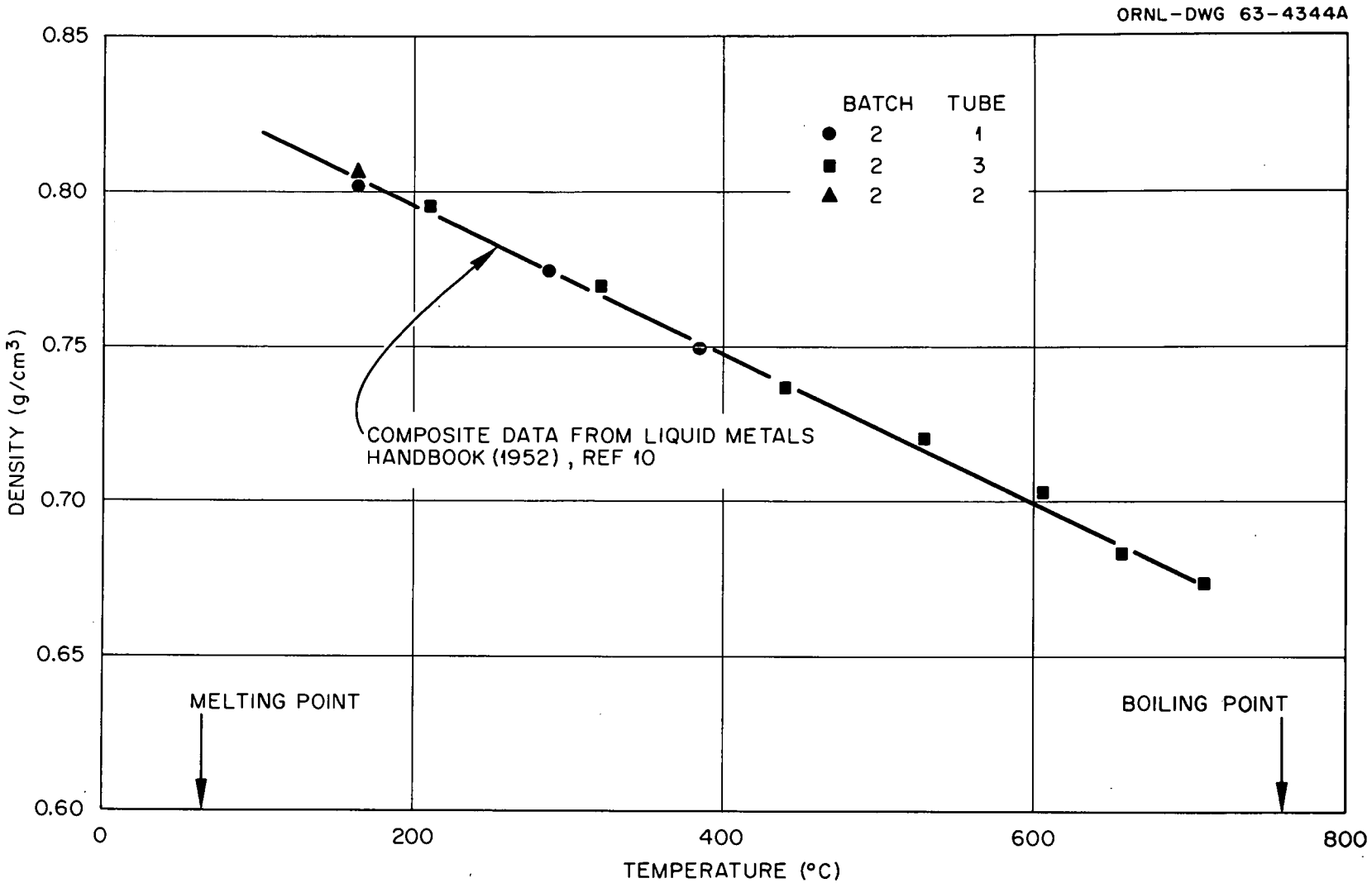

Fig. 4.2. Density of Molten Potassium as a Function of Temperature.

previously described technique.[52] At temperatures above 400°C, condensation of potassium vapor in the region of the droplet has made clear, sharp photography difficult to impossible. However, some tentative results have been obtained for an untreated, 32 μrms finish, type 304 stainless steel surface.

Immediate spreading (zero contact angle) occurred when a potassium droplet was placed on the surface preheated to 600°C in a purified helium atmosphere. A second droplet, placed on this same surface 160 min later after the surface temperature had been reduced to 300°C, showed a contact angle of 10 deg. The stainless specimen was then removed from the apparatus and cleaned so that only a thin coating of potassium remained on the surface. A third liquid potassium droplet placed on this surface (now considered as pretreated) gave an initial contact angle of 130 deg at 100°C. With increasing temperature, the angle was reduced to 90 deg for a specimen temperature at 150°C some 35 min later and finally to 15 deg at 250°C, 60 min later. These results are consistent with the earlier data with a type 316 stainless steel surface.

Further modification of the apparatus to maintain equilibrium vapor pressure near the droplet is in progress; this should afford a clean undistorted view of the droplet.

4.1.4. Surface Tension of Lithium

The surface tension (relative to helium) of 99.90 wt % lithium has been determined from 198 to 1005°C using the maximum bubble-pressure apparatus described previously.[52] The investigation was carried out at atmospheric pressure with both increasing and decreasing temperature steps. Four different size Inconel capillary tubes were used with three samples of lithium whose spectrochemical analyses before and after the experiment are given in Table 4.2.

The surface tension was calculated using the Rayleigh-Schroedinger equation.[53,54] The results are plotted in Fig. 4.3 and compared with published results. The surface tension (dynes/cm) may be expressed in the temperature range from 200 to 1000°C by the least-squares equation,

$$\sigma = 437.80 - 0.144\ t \quad , \qquad (4.2)$$

Table 4.2. Spectrochemical Analyses of Lithium Samples Nos. 1, 2, and 3 Before and After Surface Tension Determinations

Element	Samples Nos. 1, 2, & 3[a] Before, ppm	Sample No. 1 After, ppm	Sample No. 2 After, ppm
Oxygen	b	b	b
Nitrogen	11	<50	<50
Potassium	9	<15	<15
Sodium	51	65	110
Cesium	<100	<15	21
Rubidium	<8	<15	<15
Iron	<20	137	6
Chromium	<10	<5	9
Nickel	<50	62	23
Cobalt	<6	–	–
Titanium	<8	–	–
Zirconium	<20	–	–
Aluminum	<10	–	–
Magnesium	<3	–	–
Copper	<10	–	–
Silver	<1	–	–
Boron	<1	–	–
Lead	<40	–	–
Calcium	<100	–	–
Molybdenum	<10	–	–
Columbium	<20	<20	<20
Beryllium	<1	–	–
Bismuth	<3	–	–
Silicon	<10	–	–
Tin	<10	–	–
Platinum	<10	–	–
Vandaium	<10	–	–

[a]Sample No. 3 was accidently contaminated after the experiment but before an analysis could be made.

[b]Analyses not completed.

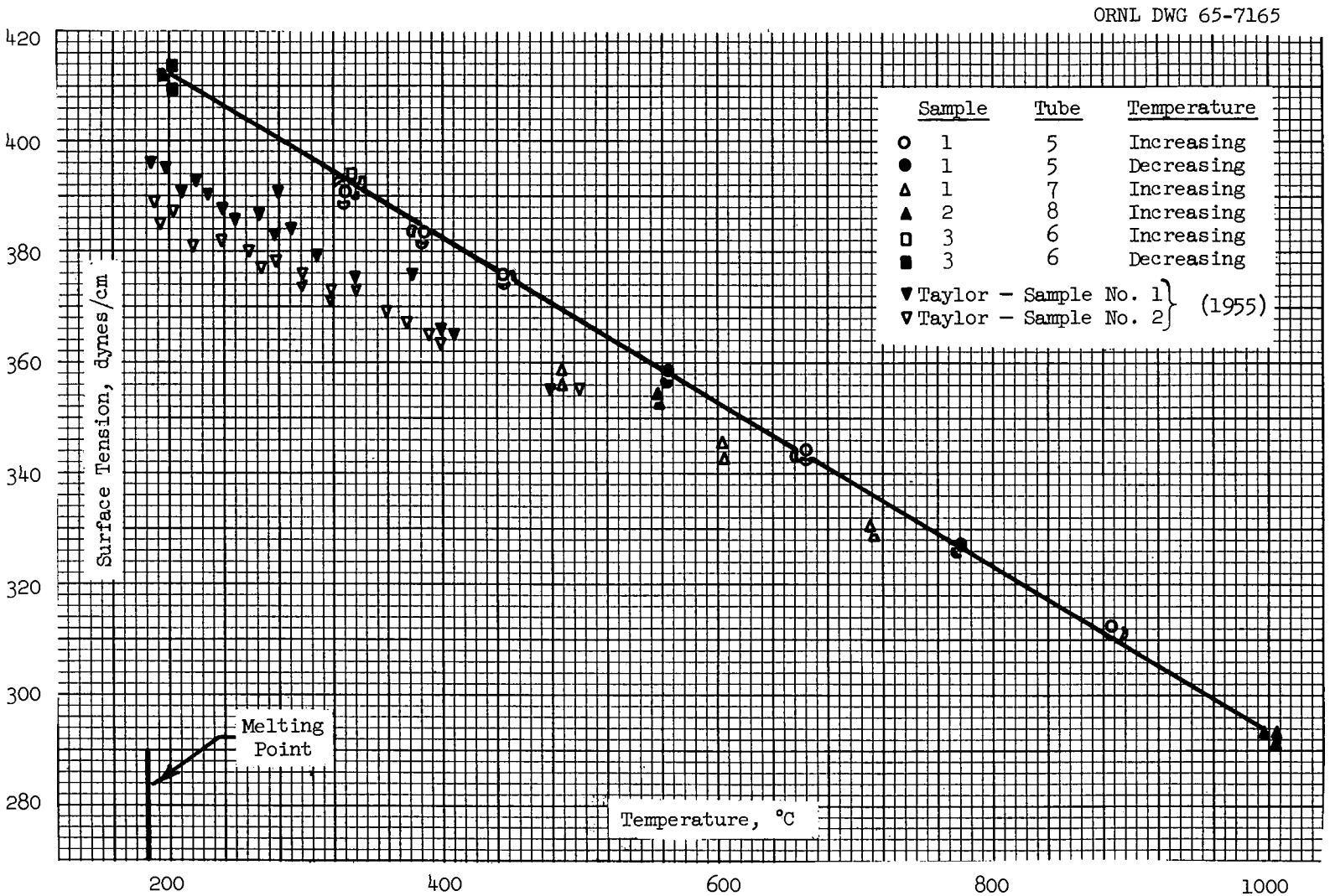

Fig. 4.3. Surface Tension of Molten Lithium as a Function of Temperature.

with a mean-square deviation of ±2.4 dynes/cm.

The experimental results of Taylor,[56] who also used the maximum bubble-pressure technique, average 5% below the present results (see Fig. 4.4). However, Taylor noted difficulties in establishing the maximum pressures due to fluctuating manometer readings and did not report the extent of potassium and rubidium impurities in the lithium (contaminants most likely to affect the surface tension).

Determinations of the surface tensions of cesium and rubidium are being planned. However, due to the highly reactive nature and low surface energy of these two alkali metals, extensive modification of the present experimental apparatus will be required.

4.1.5. Density of Lithium

The density of lithium was also calculated using the data obtained from the maximum bubble pressure at various depths of capillary immersion. The data of Been et al.[58] are compared with the present results in Fig. 4.4. Considering the very low density and high surface tension of the lithium, the agreement is quite good, with a maximum deviation of 2%.

---

[58]S. A. Been et al., "The Densities of Liquids at Elevated Temperatures: Part I. The Densities of Lead, Bismuth, Lead-Bismuth Eutectic, and Lithium in the Range Melting Point to 1000°C (1832°F)," NEPA-1585, Fairchild Engine Airplane Corp., NEPA Division, Oak Ridge, Tennessee, September 7, 1950.

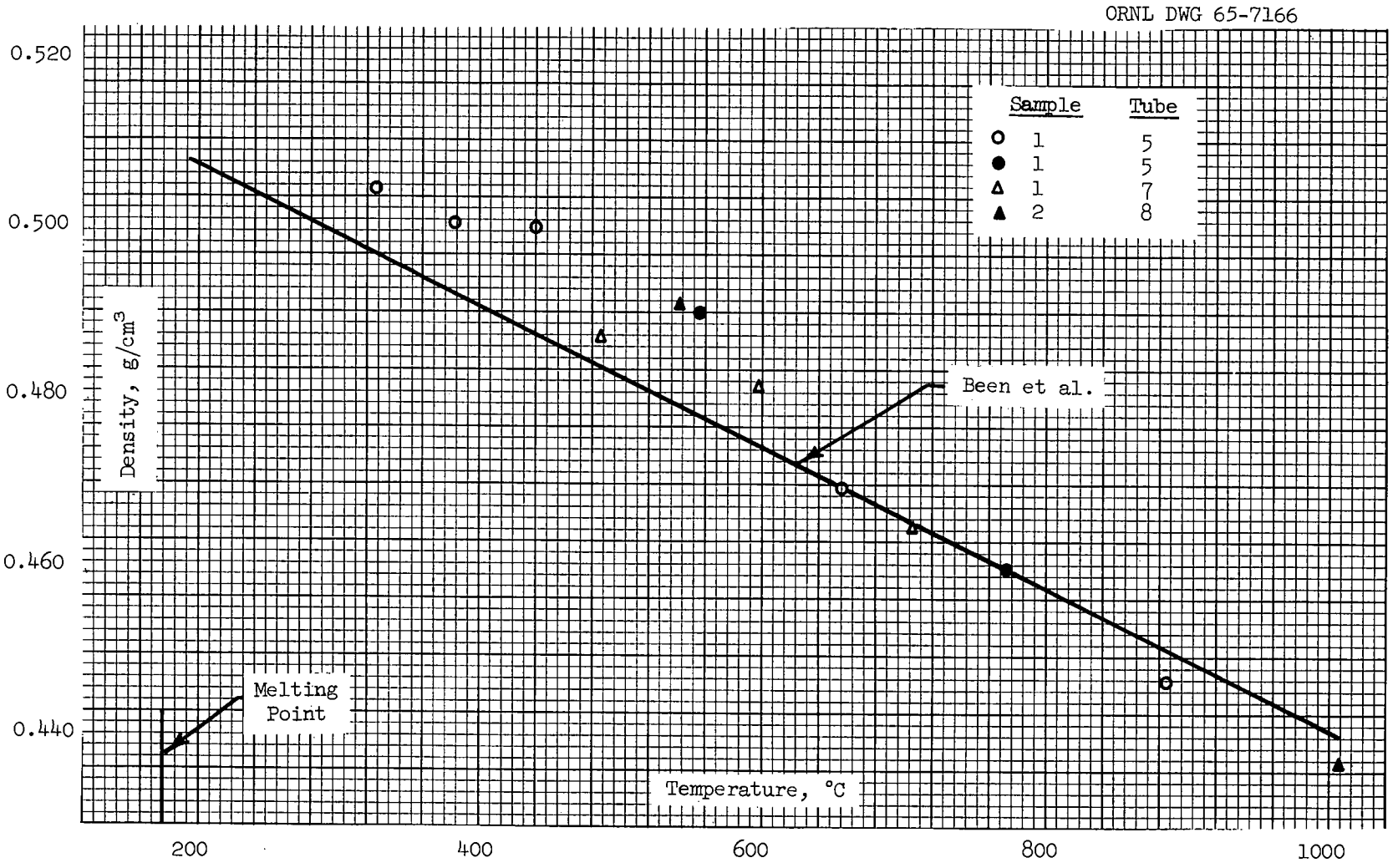

Fig. 4.4. Density of Molten Lithium as a Function of Temperature.

5. BIBLIOGRAPHY

The following lists company reports, conference proceedings, and open-literature articles published during this report period:

Boiling Potassium Heat Transfer

1. H. W. Hoffman and A. I. Krakoviak, "Convective Boiling with Liquid Potassium," Proceedings of the 1964 Heat Transfer and Fluid Mechanics Institute, W. H. Giedt and S. Levy, editors, Stanford University Press, Stanford, California, June 1964.

2. H. W. Hoffman, "Hydrodynamic and Thermal Influence in Corrosion Studies," Proceedings of the NASA-AEC Liquid-Metals Corrosion Meeting, Vol. I, pp. 273–303, NASA Report SP-41, 1964.

General Boiling Studies

1. W. R. Gambill and R. D. Bundy, "Heat-Transfer Studies of Water Flow in Thin Rectangular Channels. Part I – Heat Transfer, Burnout, and Friction for Water in Turbulent Forced Convection. Part II – Boiling Burnout Heat Flux for Low-Pressure Water in Natural Circulation," Nucl. Sci. Eng., 18: 69–89 (January 1964).

2. W. R. Gambill, "Pool-Boiling Burnout," Nuclear Safety, 5(1): 49–51 (1963).

3. W. R. Gambill, "Forced-Convection Burnout," Nuclear Safety, 5(2): 157–165 (1964).

Vortex Fluid Mechanics

1. T. S. Chang, "Exact Criterion of Hydromagnetic Stability of Inviscid Vortex Flow with Finite Conductivity," Paper No. 64-435, First Annual Meeting and Technical Display of the American Institute of Aeronautics and Astronautics, Washington, D. C., June 28 – July 2, 1964.

Thermophysical Properties

1. J. W. Cooke, "Experimental Determination of the Thermal Conductivity of Molten Lithium from 320 to 830°C," Journal of Chemical Physics, 49(7): 1902– 1909 (April 1964); see also USAEC Report ORNL-3390, Oak Ridge National Laboratory, January 1964.

Previous Progress Reports

1. H. W. Hoffman et al., "Fundamental Studies in Heat Transfer and Fluid Mechanics, Status Report July 1, 1959 – February 29, 1960," USAEC Report ORNL CF-60-10-6, Oak Ridge National Laboratory, October 1960.

2. H. W. Hoffman, J. J. Keyes, Jr., "Studies in Heat Transfer and Fluid Mechanics, Progress Report for Period January 1 – September 30, 1963," USAEC Report ORNL-TM-915, Oak Ridge National Laboratory, October 1964.

INTERNAL DISTRIBUTION

1. L. G. Alexander
2. R. A. Armistead, Jr.
3. S. E. Beall
4. M. Bender
5. E. S. Bettis
6. D. S. Billington
7. E. P. Blizard
8. A. L. Boch
9. E. G. Bohlmann
10. C. J. Borkowski
11. G. E. Boyd
12. C. A. Brandon
13. R. B. Briggs
14. F. R. Bruce
15. R. D. Bundy
16. C. C. Burwell
17. S. J. Claiborne, Jr.
18. T. S. Chang
19. T. E. Cole
20. J. W. Cooke
21. W. B. Cottrell
22. F. L. Culler
23. R. E. Dial
24. J. A. Edwards
25. D. M. Eissenberg
26. W. K. Ergen
27. D. E. Ferguson
28. A. P. Fraas
29. J. H. Frye, Jr.
30. U. C. Fulmer, Jr.
31. W. R. Gambill
32. W. F. Gauster
33. B. L. Greenstreet
34. W. R. Grimes
35. A. G. Grindell
36. R. P. Hammond
37. W. O. Harms
38. P. N. Haubenreich
39. A. S. Householder
40. P. H. Hayes
41. J. W. Hill
42-51. H. W. Hoffman
52. W. H. Jordan
53. P. R. Kasten
54. C. P. Keim
55-59. J. J. Keyes, Jr.
60. G. J. Kidd, Jr.
61. R. B. Korsmeyer
62. A. I. Krakoviak
63. K. A. Kraus
64. C. E. Larson
65. M. E. LaVerne
66. C. G. Lawson
67. J. Lones
68. M. I. Lundin
69. R. N. Lyon
70. H. G. MacPherson
71. R. E. MacPherson
72. H. C. McCurdy
73. W. B. McDonald
74. A. J. Miller
75. R. L. Miller
76. T. C. Min
77. K. Z. Morgan
78. F. N. Peebles
79. A. M. Perry
80. M. E. Ramsey
81. M. W. Rosenthal
82. A. F. Rupp
83. G. Samuels
84. W. K. Sartory
85. H. W. Savage
86. A. W. Savolainen
87. M. J. Skinner
88. A. H. Snell
89. I. Spiewak
90. R. M. Summers
91. B. J. Sutton
92. D. G. Thomas
93. D. B. Trauger
94. D. H. Wallace
95. J. S. Watson
96. A. M. Weinberg
97. G. D. Whitman
98. R. P. Wichner
99. F. J. Witt
100. M. M. Yarosh
101-103. Central Research Library (CRL)
104-105. Y-12 Document Reference Section (DRS)
106-108. Laboratory Records Department (LRD)
109. Laboratory Records Department — Record Copy (LRD-RC)
110. Reactor Division Library, Bldg. 9204-1

EXTERNAL DISTRIBUTION

111-125. Division of Technical Information Extension (DTIE)
126. Research and Development Division, ORO
127-128. Reactor Division, ORO
129. A.E.G., AEG Hochhaus, Frankfurt, Germany (M. Schuller)
130. Aerojet-General Nucleonics (K. Johnson)
131. Allis-Chalmers Manufacturing Co. (K. F. Neusen)
132. Alsthom, Paris, France (M. P. Domenjoud)
133. ANSALDO, Direzione Generale, Genova, Italy (Dr. F. Cristofori)
134. Argonne National Laboratory (Dr. Paul Lottes)
135. Argonne National Laboratory (Dr. M. Petrick)
136. Atlantic Research Nuclear Corp. (Dr. M. Markels, Jr.)
137. Atomics International (Dr. L. Bernath)
138. Babcock & Wilcox Co. (D. F. Judd)
139. Brookhaven National Laboratory (Dr. O. E. Dwyer)
140. Centre d'Etudes Nucléaires, Grenoble, France (M. Modin)
141. Centre d'Etudes Nucléaires de Saclay, Gif sur Yvette, France (M. J. Horowitz)
142. CISE, Milano, Italy (Prof. M. Silvestri)
143. Compagnie Francaise, Gagneux, France (M. Lefranc)
144. Dartmouth College, Thayer School of Engineering (Dr. G. B. Wallis)
145. Dynatech Corporation (Dr. A. Bergles)
146-147. EURATOM, Bruxelles, Belgium (Dr. P. Kruys)
148. EURATOM, Ispra, Italy (M. R. Morin)
149. FIAT, Torino, Italy (M. G. Cesoni)
150-151. General Electric Co., Atomic Power Equipment Dept. (Dr. S. Levy)
152-153. General Electric Co., Advanced Technology Laboratory (Dr. Novak Zuber)
154. Geoscience Ltd. (Dr. H. F. Poppendiek)
155. Hanford Atomic Products Operation (Dr. John Batch)
156. MAN, Nürnberg, Germany (Dr. Mayinger)
157. Massachusetts Institute of Technology (Dr. P. Griffith)
158. Massachusetts Institute of Technology (Dr. W. M. Rohsenow)
159-161. National Aeronautics & Space Administration, Lewis Research Center (Library)
162-163. National Aeronautics & Space Administration, Lewis Research Center [R. Weltmann (SEPO)]
164. North Carolina State University, Department of Chemical Engineering (Dr. J. K. Ferrell)
165. Reactor Centrum Nederland, 's Gravenhage, Netherlands (Prof. Bogaardt)
166. SNECMA, Division Atomique, Suresnes, France (M. Fouré)
167. Technische Hogeschool, Eindhoven, Netherlands (Prof. Bogaardt)
168. University of Minnesota, Department of Chemical Engineering (Dr. H. S. Isbin)
169. U. S. Atomic Energy Commission, Assistant General Manager for Reactors (Dr. J. A. Swartout)
170-171. U. S. Atomic Energy Commission, Division of Reactor Development & Technology (R. M. Scroggins)
172. U. S. Atomic Energy Commission, Division of Reactor Development & Technology (Office of Civilian Power, Water Reactors Branch)

173. U. S. Atomic Energy Commission, Division of Reactor Development & Technology (Office of Army Reactors, Technical Evaluation Branch)
174. U. S. Atomic Energy Commission, Division of Safety Standards (R. Impara)
175. Westinghouse Electric Corporation, Atomic Power Division (Dr. L. S. Tong)